

**ENHANCEMENT OF ELECTROCHEMICAL  
PROPERTIES OF GRAPHENE OXIDE BY VIOLET LASER**



**Sarawudh Nathabumroong**

**A Thesis Submitted in Partial Fulfillment of the Requirements for the**

**Degree of Doctor of Philosophy in Physics**

**Suranaree University of Technology**

**Academic Year 2020**

การปรับปรุงสมบัติทางเคมีไฟฟ้าของกราฟีนออกไซด์ด้วยการใช้เลเซอร์  
สีม่วง



นายศราวุฒิ นาทำรุ่ง

วิทยานิพนธ์นี้เป็นส่วนหนึ่งของการศึกษาตามหลักสูตรปริญญาวิทยาศาสตรดุษฎีบัณฑิต

สาขาวิชาฟิสิกส์

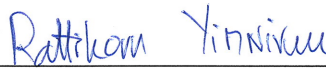
มหาวิทยาลัยเทคโนโลยีสุรนารี

ปีการศึกษา 2563

**ENHANCEMENT OF ELECTROCHEMICAL PROPERTIES OF  
GRAPHENE OXIDE BY VILOLET LASER**

Suranaree University of Technology has approved this thesis submitted in partial fulfillment of the requirements for the Degree of Doctor of Philosophy

Thesis Examining Committee

  
\_\_\_\_\_  
(Prof. Dr. Rattikorn Yimnirun)

Chairperson

  
\_\_\_\_\_  
(Assoc. Prof. Dr. Prayoon Songsirithigul)

Member (Thesis Advisor)

  
\_\_\_\_\_  
(Assoc. Prof. Dr. Saroj Rujirawat)

Member (Thesis Co-Advisor)

  
\_\_\_\_\_  
(Assoc. Prof. Dr. Thapanee Sarakonsri)

Member

  
\_\_\_\_\_  
(Assoc. Prof. Dr. Panomsak Meemon)

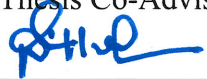
Member

  
\_\_\_\_\_  
(Dr. Adisorn Tuantranont)

Member (Thesis Co-Advisor)

  
\_\_\_\_\_  
(Dr. Narong Chanlek)

Member (Thesis Co-Advisor)

  
\_\_\_\_\_  
(Prof. Dr. Santi Maensiri)

  
\_\_\_\_\_  
(Assoc. Prof. Dr. Chatchai Jothityangkoon)

Vice Rector for Academic Affairs  
and Quality Assurance

Dean of Institute of Science

ศรารุณี นาทาบำรุง : การปรับปรุงสมบัติทางเคมีไฟฟ้าของกราฟีนออกไซด์ด้วยการใช้เลเซอร์  
สีม่วง (IMPROVEMENT OF INTRINSIC AND SURFACE PROPERTIES OF  
GRAPHENE OXIDE MATERIALS FOR SUPERCAPACITORS APPLICATIONS).

อาจารย์ที่ปรึกษา : รองศาสตราจารย์ ดร.ประยูร ส่งศิริฤทธิกุล, 158 หน้า

งานวิจัยนี้เสนอการปรับปรุงและพัฒนาวัสดุกราฟีนออกไซด์เพื่อใช้เป็นขั้วอิเล็กโทรดของตัวเก็บประจุแบบยิ่งยวด ซึ่งถูกแบ่งเป็น 2 ขั้นตอนคือ ขั้นแรกกระบวนการที่การปรับปรุงคุณสมบัติเนื้อสารของวัสดุกราฟีนออกไซด์ให้มีความนำไฟฟ้าที่ดีขึ้น รวมไปถึงเพิ่มหมู่ฟังก์ชันโดยผ่านกระบวนการไฮโดรเทอร์มอล (hydrothermal) ร่วมกับการใช้ยูเรีย ( $\text{CH}_4\text{N}_2\text{O}$ ) เพื่อเป็นวัสดุที่ให้ธาตุไนโตรเจนเจือวัสดุกราฟีนออกไซด์ (N-rGOY) ซึ่งผลการประเมินค่าประสิทธิภาพของตัวเก็บประจุแบบยิ่งยวดที่ใช้ขั้วอิเล็กโทรดที่ไม่เจือเทียบกับการเจือไนโตรเจนมีค่าความจุไฟฟ้าเชิงน้ำหนักเพิ่มจาก 25 และ 156 ฟาแรดต่อกรัม ตามลำดับ และยังคงรักษาประสิทธิภาพหลังการอัดและคายประจุ 10,000 รอบ ได้มากกว่าร้อยละ 97 มากกว่านั้นยังช่วยลดอัตราการคายประจุเองอีกด้วย ซึ่งถูกอธิบายผ่านการทำให้เกิดการเจือของไนโตรเจนในโครงสร้างของวัสดุกราฟีนออกไซด์ ที่ถูกตรวจสอบโดยเครื่องมือวิเคราะห์วัสดุนาโนโดยเทคนิคสเปกโทรสโกปีโฟโตอิเล็กตรอนด้วยรังสีเอกซ์คือ quaternary/graphitic-N ที่ช่วยเพิ่มความสามารถในการนำไฟฟ้าผ่านข้อมูลิมพีแดนซ์สเปกโทรสโกปีเชิงเคมีไฟฟ้า และ pyridinic-N กับ pyrrolic-N ที่ช่วยในการเกิด pseudocapacitance ผ่านข้อมูลจากไซคลิกโวลแทมเมตรีและกัลวานอสแตติกชาร์จ/ดิชาร์จซึ่งเป็นตัวแปรสำคัญในการพัฒนาตัวเก็บประจุแบบยิ่งยวด แต่ยังคงไว้ซึ่งลักษณะโครงสร้างของกราฟีนออกไซด์ผ่านข้อมูลโครงสร้าง  $sp^2$  และ  $I_D/I_G$  จากข้อมูลจากรามานสเปกโทรสโกปี และคุณสมบัติการชอบน้ำที่มากขึ้นจากลดลงของมุมสัมผัสของอิเล็กโทรไลต์

ในขั้นที่สองคือการปรับปรุงพื้นผิวของขั้วอิเล็กโทรดโดยการฉายด้วยแสงเลเซอร์สีม่วง (N-rGOY-VX) ซึ่งในการทดลองจะแสดงให้เห็นถึงอิทธิพลของจำนวนรอบของการฉายแสงหรือเวลาในการฉายแสงและความเข้มแสง (intensity) ต่อทั้งขั้วอิเล็กโทรดที่เจือและไม่เจือด้วยไนโตรเจน ซึ่งจากผลการทดลองผลของแสงเลเซอร์สีม่วงที่ส่งผลการพัฒนาชัดเจนผ่านจากจ่ายความต่างศักย์ประมาณ 7-10.2 โวลต์และจำนวนรอบที่เพิ่มขึ้น ซึ่งค่าสูงสุดที่ได้จากค่าความจุไฟฟ้าเชิงน้ำหนักเพิ่มคือ 214 ฟาแรดต่อกรัม และยังคงรักษาประสิทธิภาพได้มากกว่าร้อยละ 94 การใช้งานผ่านการอัดและคายประจุ 10,000 รอบ มากกว่านั้นยังช่วยลดอัตราการคายประจุเองอีกด้วย ซึ่งถูกอธิบายผ่านความสามารถในการนำไฟฟ้าที่ดีขึ้นผ่านข้อมูลิมพีแดนซ์สเปกโทรสโกปีเชิงเคมีไฟฟ้า การเกิดการลอกของแผ่นกราฟีนออกไซด์ที่เคยซ้อนทับกันผ่านข้อมูลจากกล้องจุลทรรศน์อิเล็กตรอนแบบส่องกราดและเทคนิคเอกซเรย์ดีฟแฟรคชัน และข้อมูลจากเทคนิคสเปกโทรสโกปีโฟโตอิเล็กตรอนด้วยรังสีเอกซ์และรามานสเปกโทรสโกปีแสดงให้เห็นการลดลงของหมู่ฟังก์ชันออกซิเจนจากโครงสร้างของกราฟีนออกไซด์

(reduced graphene oxide) ยิ่งไปกว่านั้นยังมีหลักฐานของการกลับไปสร้างพันธะ C=C อีกครั้ง (reestablishment) ซึ่งเป็นโครงสร้างของกราฟีน (graphene) หลังจากการหลุดออกของหมู่ฟังก์ชันออกซิเจน ผ่านการมีค่าสัดส่วนโครงสร้าง  $sp^2$  ที่เพิ่มขึ้น ค่า  $I_D/I_G$  และ  $I_{D+G}/I_G$  ที่ลดลง และการแสดงการเปลี่ยนจากสภาพโครงสร้างอสัณฐาน (amorphous) กลายเป็นสภาพโครงสร้างแบบผลึก (crystalline) มากขึ้นผ่านจากขั้วของพีค G ไปยังค่าเลขคลื่นที่น้อยลง

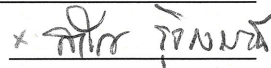
และที่สำคัญยังมีความเป็นไปได้ในการประยุกต์ในเชิงอุตสาหกรรมเพราะไม่ได้มีการเปลี่ยนระบบการผลิตของตัวเก็บประจุแบบยิ่งยวดในปัจจุบัน เพียงแต่มีการเพิ่มกระบวนการในการเตรียมขั้วอิเล็กโทรดก่อนการขึ้นรูปเซลล์



สาขาวิชาฟิสิกส์  
ปีการศึกษา 2563

ลายมือชื่อนักศึกษา 

ลายมือชื่ออาจารย์ที่ปรึกษา 

ลายมือชื่ออาจารย์ที่ปรึกษาร่วม \* 

ลายมือชื่ออาจารย์ที่ปรึกษาร่วม 

ลายมือชื่ออาจารย์ที่ปรึกษาร่วม กนกนที จันทร์แก้ว

SARAWUDH NATHABUMROONG : ENHANCEMENT OF  
ELECTROCHEMICAL PROPERTIES OF GRAPHENE OXIDE BY VIOLET  
LASER. THESIS ADVISOR : ASSOC. PROF. PRAYOON  
SONGSIRIRITTHIGUL, Ph.D. 158 PP.

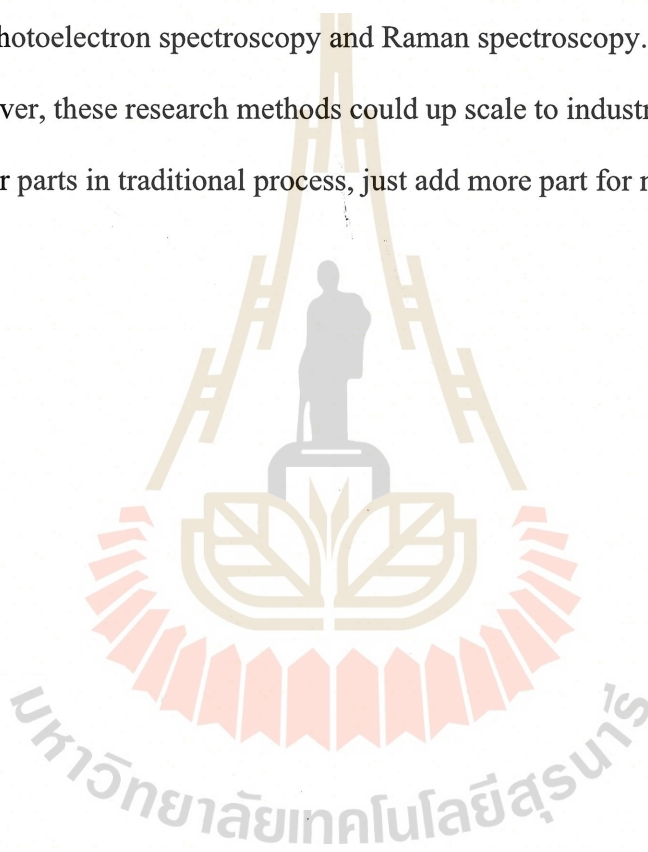
#### GRAPHENE OXIDE / VIOLET LASER

In this thesis, we have proposed two steps to enhance the electrochemical properties of graphene oxide (GO) for use as supercapacitor (SC) electrode material. Firstly, GO was reduced and doped with different concentrations of nitrogen by using a simple hydrothermal method. The highest specific capacitance of  $156 \text{ F g}^{-1}$  was reached for the prepared nitrogen doped reduced graphene oxide (N-rGO) with urea content of 40% (w/v) compared to  $25 \text{ F g}^{-1}$  for undoped. It was also found that it can maintain a capacitive retention of 97% after charge-discharge for 10,000 cycles. The prepared N-rGO samples were characterized by Raman spectroscopy, Fourier-transform infrared (FT-IR), X-ray photoelectron spectroscopy (XPS). The results indicated the successful reduction and incorporation of nitrogen, including, quaternary/graphitic-N, pyridinic-N and pyrrolic-N in the structure. This results in enhancing of the electrical conductivity, wettability, and providing additional pseudocapacitive charge storage mechanism.

Secondly, the surface of N-rGO was irradiated with violet laser at a wavelength of 405 nm. This was performed by using our in-house laser scribing machine adapted from a commercial 3D printer. After the surface irradiation, the highest specific capacitance was enhanced up to a value of  $214 \text{ F g}^{-1}$ , 48% as compared with non-treated electrode. The capacitive retention maintained at 94% after charge-discharge for 10,000 cycles

Moreover, enough intensity are controlled via applying voltage for 7-10.2 V and increasing of repeating cycle of VLT to 5 cycles prefer to useful because characterization showed surface exfoliation, higher d-spacing via scanning electron microscopy and X-ray diffraction, surface transformation from amorphous to more crystalline state via decreasing of  $I_D/I_G$  and  $I_{D'}/I_G$ , shifting of G band peak, more  $sp^2$  hybridization state or reestablishment of  $sp^2$  after reduced oxygen functional groups and decrease disorder state using X-ray photoelectron spectroscopy and Raman spectroscopy.

Moreover, these research methods could up scale to industry because there are not changing other parts in traditional process, just add more part for manufacturing.



School of Physics

Academic Year 2020

Student's Signature \_\_\_\_\_

Advisor's Signature \_\_\_\_\_

Co-Advisor's Signature \_\_\_\_\_

Co-Advisor's Signature \_\_\_\_\_

Co-Advisor's Signature \_\_\_\_\_

## ACKNOWLEDGEMENTS

My thesis could not be accomplished without help and support from many people, to whom I would like to express my sincere words of acknowledgments.

First, I would like to express my sincere gratitude to Prof. Dr. Rattikorn Yimmirun, my supervisor and chairman of thesis defense committee, for his valuable advice, very kind patience, guidance and encouragement in all steps. In addition to scientific education, he also teach me to be optimism that greatly help and motivate me throughout this work.

I am also very grateful to Assoc. Prof. Dr. Prayoon Songsiririthigul who is my kind advisor for Degree of Doctor of Philosophy in Physics at Suranaree University of Technology. He provides very good aspect, experience, suggestion, and support which are very important for my graduation.

I would like to express my grateful to Assoc. Prof. Dr. Saroj Rujirawat who is my kind co-advisor for introducing and suggesting me with many points of view in scientific. Moreover, he provides kind support to me. I am also very grateful to Dr. Adisorn Tuantranont who is my kind co-advisor for supporting and providing me the opportunity to work in his laboratory.

I would like to express my grateful Dr. Narong Chanlek who is my kind co-advisor for introducing and suggesting me with research skills. Moreover, he had been very patient to teach me.

I would like to acknowledge Assoc. Prof. Dr. Thapanee Sarakonstri who is the thesis defense committee, for giving her valuable time.

I would like to thank Asst. Prof. Dr. Prasit Thongbai, who was my kind advisor of undergraduate research project at Khon Kaen University. He was a very important person who supported and helped me for graduating in bachelor's degree.

I would like to thank Assoc. Prof. Dr. Worawat Meevasana, who was my advisor master's degree at Suranaree University of Technology. He gave me very good experience in research and helped me for graduating.

I would like to give big thank to Dr. Chatwarin Poochai, Dr. Tanachat Eknapakul, Jaturon Netthonglang, every people at Thai Organic and Printed Electronics Innovation Center (TOPIC) , every people at Beamline 5.3 and Beamline 3.2 at Synchrotron Light Research Institute (SLRI), every people in the characterization group, school of physics, SUT, my relations, all teachers, my friends, my seniors, my juniors and all staffs in school of Physics for their support. I would like to thank the Science Achievement Scholarship of Thailand (SAST) for financial support since bachelor's degree. Moreover, my girlfriend to be who I still do not know her for supporting and encouraging me to everything which I needed and every time when I faced problems. Surely, I wish to see her in near future (and I found her already while I have corrected this thesis).

Finally, I would like to express appreciation to my parents, both my older and younger brother for great support, encouragement, and good aspect as well as good advice to me over the years of my life.

Sarawudh Nathabumroong

# CONTENTS

	<b>Page</b>
ABSTRACT IN THAI.....	I
ABSTRACT IN ENGLISH .....	III
ACKNOWLEDGEMENTS .....	V
CONTENTS.....	VII
LIST OF TABLES .....	XI
LIST OF FIGURES .....	XIV
<b>CHAPTER</b>	
<b>I INTRODUCTION.....</b>	<b>1</b>
1.1 Background and significance of the study .....	1
1.2 Objectives and structure of this thesis.....	7
1.3 Scope and limitations .....	8
<b>II LITERATURE REVIEW.....</b>	<b>9</b>
2.1 Supercapacitors (SCs) .....	9
2.1.1 Electrostatic double layer capacitors (ELDCs) .....	9
2.1.2 Pseudocapacitors .....	10
2.1.3 Hybrid capacitors .....	12
2.2 Components of supercapacitors .....	13
2.2.1 Electrode.....	13
2.2.2 Electrolyte .....	14

## CONTENTS (Continued)

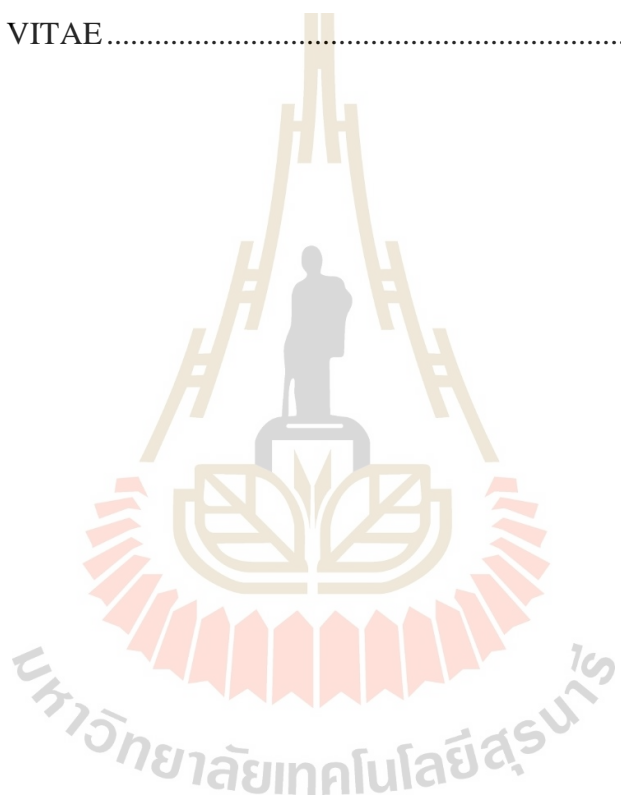
	<b>Page</b>
2.2.3 Separator.....	15
2.3 Graphene oxide (GO).....	15
2.4 Reduction of graphene oxide ad laser irradiation .....	17
<b>III EXPERIMENTAL AND TECHNIQUES</b> .....	<b>24</b>
3.1 Material preparations .....	24
3.1.1 Graphene oxide.....	25
3.1.2 Nitrogen doped reduced graphene oxide (N-rGO).....	26
3.1.3 Nitrogen and sulfur co-doped reduced graphene oxide (NandS-rGO)..	27
3.2 Electrode farications.....	27
3.3 Violet laser treatment .....	28
3.4 Supercapacitor coin cell assembly .....	31
3.5 Electrochemical evaluations .....	32
3.5.1 Galvanostatic charge/discharge (GCD) measurement .....	32
3.5.2 Cyclic voltammetry (CV) measurement.....	35
3.5.3 Electrochemical impedance spectroscopy (EIS) measurement.....	38
3.5.4 Leakage current or self-discharge measurement .....	39
3.6 Material characterization techniques.....	40
3.6.1 X-ray diffraction (XRD).....	40
3.6.2 Scanning electron microscopy (SEM).....	44
3.6.3 Raman spectroscopy.....	45

## CONTENTS (Continued)

	<b>Page</b>
3.6.4 Fourier transform infrared (FT-IR) .....	47
3.6.5 X-ray photoelectron spectroscopy (XPS).....	50
3.6.6 Contact angle and wettability measurement.....	51
<b>IV RESULTS AND DISCUSSION.....</b>	<b>52</b>
4.1 Synthesis and characterization of graphene oxide (GO).....	52
4.2 Nitrogen doped reduced graphene oxide (N-rGO).....	58
4.2.1 Electrochemical performance.....	58
4.2.2 Characterization.....	66
4.3 Comparative study of structural and electrochemical properties of reduced graphene oxide, nitrogen doped reduced graphene oxide, and nitrogen and sulfur co-doped reduced graphene oxide.....	77
4.3.1 Electrochemical performance.....	78
4.3.2 Scanning electron microscopy.....	81
4.3.3 Fourier transform infrared spectroscopy (FT-IR) .....	82
4.3.4 X-ray photoelectron spectroscopy.....	82
4.3.5 Raman spectroscopy.....	86
4.3.6 Contact angle.....	88
4.4 Violet laser treatment (VLT) on N-rGO .....	89
4.4.1 Electrochemical properties .....	91

## CONTENTS (Continued)

	<b>Page</b>
<b>V CONCLUSIONSION</b> .....	133
REFERENCES .....	135
APPENDIX.....	153
CURRICULUM VITAE.....	158



## LIST OF TABLES

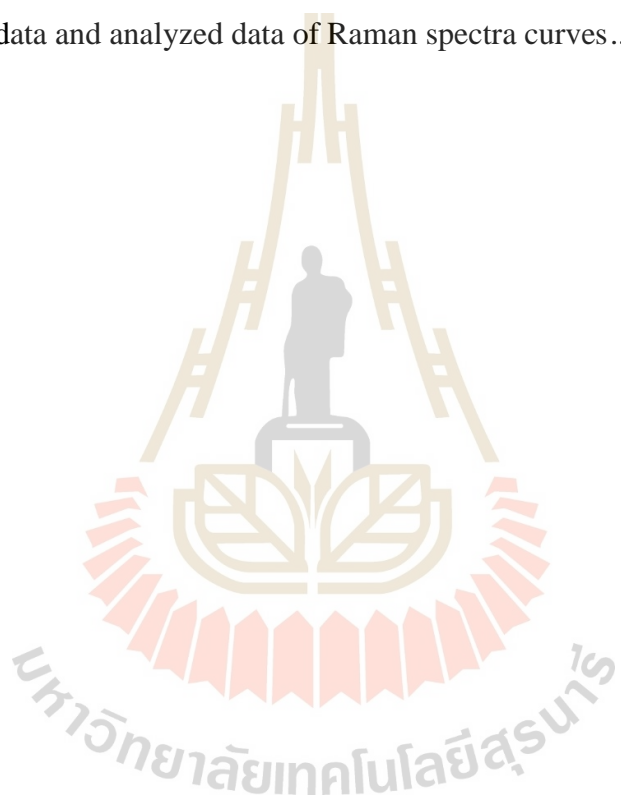
Table	Page
3.1 Possible diffraction plane and their located $2\theta$ for XRD .....	43
3.2 Possible bonding and their located wavenumber for FT-IR.....	49
4.1 The fitted data and analyzed data of Raman spectra of the prepared GO .....	58
4.2 Electrochemical performance results of rGO and all N-rGOY coin cell supercapacitors .....	63
4.3 The operating voltage, discharging time, specific capacitances, energy densities and power densities of SCs using rGO, N-rGO20, N-rGO40 and N-rGO60 in 1 M H <sub>2</sub> SO <sub>4</sub> at 0.125 A g <sup>-1</sup> .....	64
4.4 The results of XPS curve-fitting from Figure 4.16 (b)- (e) .....	74
4.5 The results of XPS curve-fitting of O1s from Figure 4.16 (f)- (i).....	74
4.6 The results of XPS curve-fitting of N1s from Figure 4.16 (j)- (l).....	74
4.7 The fitted data and analyzed data of Raman spectra curves.....	76
4.8 The results of XPS curve-fitting from C1s peak in Figure 4.25 (b)- (d).....	85
4.9 The results of XPS curve-fitting from O1s peak in Figure 4.25 (e)- (g).....	85
4.10 The results of XPS curve-fitting from N1s peak in Figure 4.25 (h), (i).....	85
4.11 The results of XPS curve-fitting from S2p peak in Figure 4.25 (j).....	86
4.12 The fitted data and analyzed data of Raman spectra curves.....	87
4.13 Electrochemical performance results of N-rGO20, N-rGO20-V1, N-rGO20-V3 and N-rGO20-V5 coin cell supercapacitors.....	94

## LIST OF TABLES (Continued)

<b>Table</b>	<b>Page</b>
4.14 Electrochemical performance results of N-rGO20, N-rGO20-V1, N-rGO20-V3 and N-rGO20-V5 coin cell supercapacitors.....	97
4.15 Electrochemical performance results of N-rGO40, N-rGO40-V1, N-rGO40-V3 and N-rGO40-V5 coin cell supercapacitors.....	101
4.16 Electrochemical performance results of N-rGO40, N-rGO40-V3 with varies intensity via applied voltage as 3, 7, and 10.2 V coin cell supercapacitors .....	105
4.17 Electrochemical performance results of N-rGO60, N-rGO60-V1, N-rGO60-V3 and N-rGO60-V5 coin cell supercapacitors.....	109
4.18 The operating voltage, charging and discharging time, specific capacitances, energy densities and power densities of SCs using rGO, rGO-VX, N-rGOY and N-rGOY-VX in 1 M H <sub>2</sub> SO <sub>4</sub> at 0.125 A g <sup>-1</sup> .....	110
4.19 The operating voltage, charging and discharging time, specific capacitances, energy densities and power densities of SCs using N-rGO40 and varies laser intensity with 3 treated cycles in 1 M H <sub>2</sub> SO <sub>4</sub> at 0.125 A g <sup>-1</sup> .....	111
4.20 The results of XPS curve-fitting of C1s from Figure 4.49 (b), (c)- Figure 4.52 (b), (c).....	122
4.21 The results of XPS curve-fitting of O1s from Figure 4.49 (d), (e)- Figure 4.52 (d), (e).....	122

**LIST OF TABLES (Continued)**

<b>Table</b>	<b>Page</b>
4.22 The results of XPS curve-fitting of N1s from Figure 4.50 (f), (g)- Figure 4.52 (f), (g).....	123
4.23 The fitted data and analyzed data of Raman spectra curves.....	128
4.24 The fitted data and analyzed data of Raman spectra curves.....	130



## LIST OF FIGURES

Figure	Page
1.1 Estimated energy and power densities of SCs compared with capacitors, commercially available batteries .....	2
1.2 Photographs of commercial, supercapacitors and their proposed application.....	3
1.3 Schematic representation of EDLC or symmetric supercapacitor.....	4
1.4 Flow chart of this thesis.....	7
2.1 Schematic of charge-storage mechanism of for EDLC .....	10
2.2 Schematic of charge-storage mechanism for different types of pseudocapacitive Electrode: underpotential deposition, redox pseudocapacitance, and intercalation Pseudocapacitance .....	12
2.3 Possible graphene oxide (GO) structure .....	16
2.4 Possible structure of nitroge doped rGO .....	19
2.5 SEM image of the surface of GO before and after laser irradiation reduced Graphene (rGO).....	22
2.6 C1s XPS peak of GO before and after irradiation with infrared laser.....	22
3.1 Preparation of graphene oxide.....	26
3.2 Preparation of the electrode for N -rGO and N andS-rGO.....	28
3.3 Photographs of the in-house laser scribig machine adapted from a 3D printing and its components.....	29
3.4 Photographs of wrting a pattern on an electrode by laser scribig machine.....	30

## LIST OF FIGURES (Continued)

<b>Figure</b>	<b>Page</b>
3.5 Laser irradiation process and control. ....	31
3.6 Assembly of supercapacitor coin cells .....	32
3.7 Example of GCD profile.....	33
3.8 Example for CV profile .....	36
3.9 Example of Nyquist plot obtained from electrochemical impedance spectroscopy (EIS) measurement .....	38
3.10 Example of leak current or self-discharge measurement.....	40
3.11 Schematic representation of Bragg's Law for XRD .....	41
3.12 Schematic diagram of (a) the basic SEM components and (b) different types of SEM signals .....	44
3.13 Schematic diagram of the identification of Raman scattering signal (a) example of deconvoluted Raman spectra (b) .....	45
3.14 Simple schematic of FT-IR spectrometer.....	48
3.15 Schematic representation of X-ray photoelectron spectroscopy (XPS) technique.....	50
3.16 Schematic of a sessile-drop contact angle with electrode surface and electrolyte system. ....	51
4.1 SEM images of graphite (a), (b) and prepared GO (c), (d) ad SEM images of graphene oxide (GO) with varies magnifications (e)- (g) .....	53
4.2 XRD result of graphene oxide (GO).....	54

## LIST OF FIGURES (Continued)

<b>Figure</b>	<b>Page</b>
4.3 FT-IR spectrum of the synthesized GO.....	55
4.4 Wide scan XPS spectrum of the synthesized GO.....	55
4.5 High resolution XPS spectra of C1s and O1s peak of GO .....	56
4.6 Raman spectroscopy result of GO .....	57
4.7 GCD (a)-(d), and CV (e)-(h) of rGO, and N-rGOY coin cells.....	60
4.8 The specific capacitance from GCD and CV measurement of rGO, and N-rGOY coin cells .....	62
4.9 Electrochemical impedance spectroscopy of rGO and N-rGOY coin cells .....	63
4.10 Percentage and the specific capacitance of capacitive retentions of rGO and N-rGO40 coin cells.....	65
4.11 Percentage and the specific capacitance of capacitive retentions of rGO, N-rGO20 and N-rGO40.....	66
4.12 SEM images of rGO (a)-(c), N-rGO20 (d)-(f), N-rGO40 (g)-(i), and N-rGO60 (j), (l) with difference magnifications .....	67
4.13 Cross-section SEM image of N-rGO40 for showing thickness of all activated film materials. ....	68
4.14 XRD pattern of rGO and N-rGO40 electrode .....	69
4.15 FT-IR spectra of rGO, N-rGO20, N-rGO40 and N-rGO60 electrode .....	70

## LIST OF FIGURES (Continued)

<b>Figure</b>	<b>Page</b>
4.16 Wide scan spectra of rGO and N-rGOY spectra (a), and (b) (c) (d) (e) C1s peak, (f) (g) (h) (i) O1s peak of rGO, N-rGO20, N-rGO40, and N-rGO60, respectively, and (j) (k) (l) N1s peak of N-rGO20, N-rGO40, and N-rGO60, respectively.....	72
4.17 Percentage of each bonding in C1s, O1s, and N1s for rGO, N-rGO20, N-rGO40 and N-rGO60.....	73
4.18 Raman spectroscopy spectra of rGO, N-rGO20, N-rGO40, and N-rGO60 .....	75
4.19 Contact angle of rGO and N-rGOY electrodes with 1 M H <sub>2</sub> SO <sub>4</sub> in DI water as electrolyte .....	77
4.20 GCD (a)-(c), CV (d)-(f) of rGO, N-rGO, and NandS-rGO coin cells in 1 M H <sub>2</sub> SO <sub>4</sub> in DI water as aqueous electrolyte .....	79
4.21 Calculated the specific capacitance from GCD and CV results of rGO, N-rGO, and NandS-rGO.....	80
4.22 EIS results of rGO, N-rGO, and NandS-rGO.....	81
4.23 SEM image of rGO, N-rGO, and NandS-rGO .....	81
4.24 FT-IR spectra of rGO, N-rGO, and NandS-rGO.....	82
4.25 XPS spectra of rGO, N-rGO, and NandS- rGO.....	84
4.26 Raman spectroscopy spectra of rGO, N-rGO, and NandS-rGO.....	87
4.27 Contact angle of rGO, N-rGO, and NandS-rGO .....	88

## LIST OF FIGURES (Continued)

<b>Figure</b>	<b>Page</b>
4.28 SEM image of cross-section view of electrode for showing interface of N-rGO40 and N-rGO40-V5 region .....	90
4.29 GCD and CV results of rGO, rGO-V1, rGO-V3 and rGO-V5 coin cells.....	92
4.30 Calculated the specific capacitance from GCD and CV results of rGO, rGO-V1, rGO-V3 and rGO-V5 coin cells .....	93
4.31 EIS results of rGO, rGO-V1, rGO-V3 and rGO-V5 coin cells. ....	94
4.32 GCD and CV results of N-rGO20, N-rGO20-V1, N-rGO20-V3 and N-rGO20-V5 coin cells. ....	95
4.33 Calculated the specific capacitance from GCD and CV results of N-rGO20, N-rGO20-V1, N-rGO20-V3 and N-rGO20-V5 coin cells .....	96
4.34 EIS results of N-rGO20, N-rGO20-V1, N-rGO20-V3 and N-rGO20-V5 coin cells .....	97
4.35 GCD and CV results of N-rGO40, N-rGO40-V1, N-rGO40-V3 and N-rGO40-V5 coin cells .....	99
4.36 Calculated the specific capacitance from GCD and CV results of N-rGO40, N-rGO40-V1, N-rGO40-V3 and N-rGO40-V5 coin cells.....	100
4.37 EIS results of N-rGO40, N-rGO40-V1, N-rGO40-V3 and N-rGO40-V5 coin cells .....	101
4.38 GCD and CV results of N-rGO40, N-rGO40-V3-3V, N-rGO40-V3-7V and N- N-rGO40-V3-10.2V coin cells .....	103

## LIST OF FIGURES (Continued)

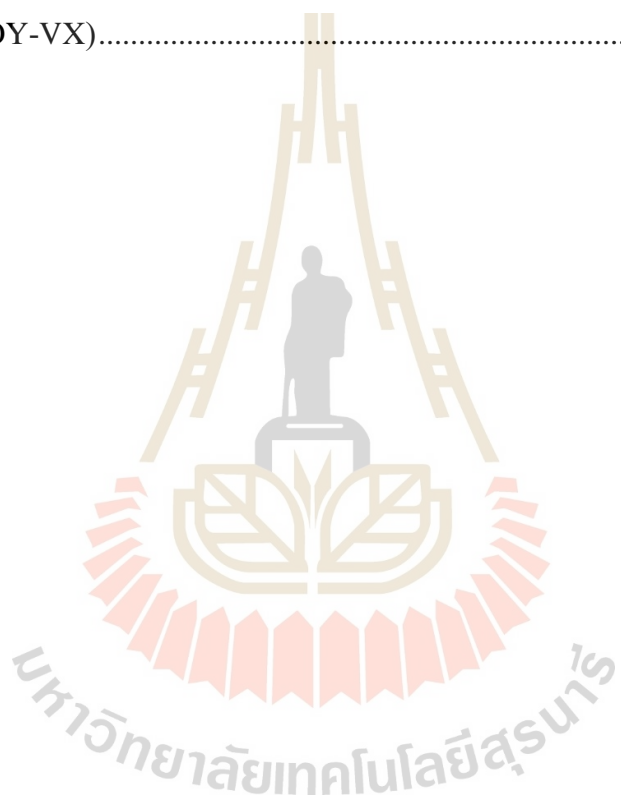
<b>Figure</b>	<b>Page</b>
4.39 Calculated the specific capacitance from GCD and CV results of N-rGO40, N-rGO40-V3-3V, N-rGO40-V3-7V and N- N-rGO40-V3-10.2V coin cells.....	104
4.40 EIS results of N-rGO40, N-rGO40-V3-3V, N-rGO40-V3-7V and N-rGO40-V3-10.2V coin cells .....	105
4.41 GCD and CV results of N-rGO60, N-rGO60-V1, N-rGO60-V3 and N-rGO60-V5 coin cells.....	107
4.42 Calculated the specific capacitance from GCD and CV results of N-rGO60, N-rGO60-V1, N-rGO60-V3 and N-rGO60-V5 coin cells.....	108
4.43 EIS results of N-rGO60, N-rGO60-V1, N-rGO60-V3 and N-rGO60-V5 coin cells .....	109
4.44 Percentage and the specific capacitance of capacitive retentions of rGO and N-rGO40 coin cells.....	112
4.45 Leakage current of some N-rGOY-VX coin cells .....	113
4.46 SEM images of N-rGO40 (a) (b), N-rGO40-V1 (c) (d), N-rGO40-V3 (e) (f) and N-rGO40-V5 (g) (h), Top view of interface between N-rGO40 and N-rGO40-V5 (i), and side view of interface between of N-rGO40 and N-rGO40-V5 region (j) .....	115
4.47 XRD results of comparative result of rGO, rGO-V5 (a), and N-rGO40, N-rGO40-V5 (b) electrode.....	116

## LIST OF FIGURES (Continued)

Figure	Page
4.48 Wide scan spectra of rGO and rGO-V5 (a), C1s of rGO (b), C1s of rGO-V5 (c), O1s of rGO (d), and O1s of rGO-V5 (e) electrode.....	118
4.49 Wide scan spectra N-rGO20 and N-rGO20-V5 (a), C1s of N-rGO20 (b), C1s of N-rGO20 -V5 (c), O1s of N-rGO20 (d), O1s of N-rGO20 -V5 (e), N1s of N-rGO20 (f), N1s of N-rGO20 -V5 (g) electrode .....	119
4.50 Wide scan spectra N-rGO40 and N-rGO40-V5 (a), C1s of N-rGO40 (b), C1s of N-rGO40 -V5 (c), O1s of N-rGO40 (d), O1s of N-rGO40 -V5 (e) N1s of N-rGO40 (f), N1s of N-rGO40 -V5 (g) electrode .....	120
4.51 Wide scan spectra N-rGO60 and N-rGO60-V5 (a), C1s of N-rGO60 (b), C1s of N-rGO60 -V5 (c), O1s of N-rGO60 (d), O1s of N-rGO60 -V5 (e), N1s of N-rGO60 (f), N1s of N-rGO60 -V5 (g) electrode .....	121
4.52 Survey scan XPS spectra of (a) of N-rGO and N-rGO-V5, high-resolution XPS spectra of C1s signal for (b) N-rGO, (c) N-rGO-V1, (d) N-rGO-V3 and (e) N-rGO-V5, (f) percentage amount of C=C sp <sup>2</sup> and C-O/N, species and (g) percentage amount of C=O/N, COOH, and C-F species concerning the repeating number of VLT treatments .....	125
4.54 Raman spectroscopy spectra of N-rGO40, N-rGO40-V1, N-rGO40-V3 and N-rGO40-V5 electrode .....	127
4.55 Comparative Raman spectroscopy spectra for rGO, rGO-V5, N-rGO20, N-rGO20-V5, N-rGO60, and N-rGO60-V5 electrode .....	129

**LIST OF FIGURES (Continued)**

<b>Figure</b>	<b>Page</b>
4.56 Picture and results of contact angle of all electrodes (rGO, rGO-VX, N-rGOY, and N-rGOY-VX).....	131
4.57 Results of contact angle of all electrodes (rGO, rGO-VX, N-rGOY, and N-rGOY-VX).....	132



# CHAPTER I

## INTRODUCTION

### 1.1 Background and significance of the study

Global warming and climate change mainly caused by the usage of fossil fuels, which is associated with CO<sub>2</sub> emission, have greatly affected our world economy and ecology. This has brought our attention to alternating energy sources which are sustainable and environmentally friendly, such as wind, solar and wave energies. However, these renewable energy sources still have the main limitation of the reliability of supply. For example, the solar energy cannot be harvested all day and all night, or wind turbine can work in windy ambient (Winter and Brodd, 2005). Efficient energy storage systems are therefore required for utilization of these energies. Supercapacitors (SCs) are electrical energy storage devices which can store and deliver energy at relatively higher rates as compared to batteries and exhibit some superior properties, such as, fast discharge/charge, high power density with acceptably high energy densities ( $> 10 \text{ Wh kg}^{-1}$ ), excellent reversibility and cyclability (more than 100 times that of batteries). The estimated energy and power density of supercapacitors in comparison with commercially available capacitors, and batteries are shown in Figure 1.1. SCs are also low-cost, stable in long-term operation and easy for applying to electronic devices (Compton and Nguyen, 2010) (Miller and Simon, 2008) (Pan, Li, and Feng, 2010) (Dyatkin et al., 2013) (L. L. Zhang and Zhao, 2009) (Brian Evans Conway, 1991)

(Du and Pan, 2006) (Guerrero, Romero, Barrero, Milanés, and Gonzalez, 2009) (Shao et al., 2018).

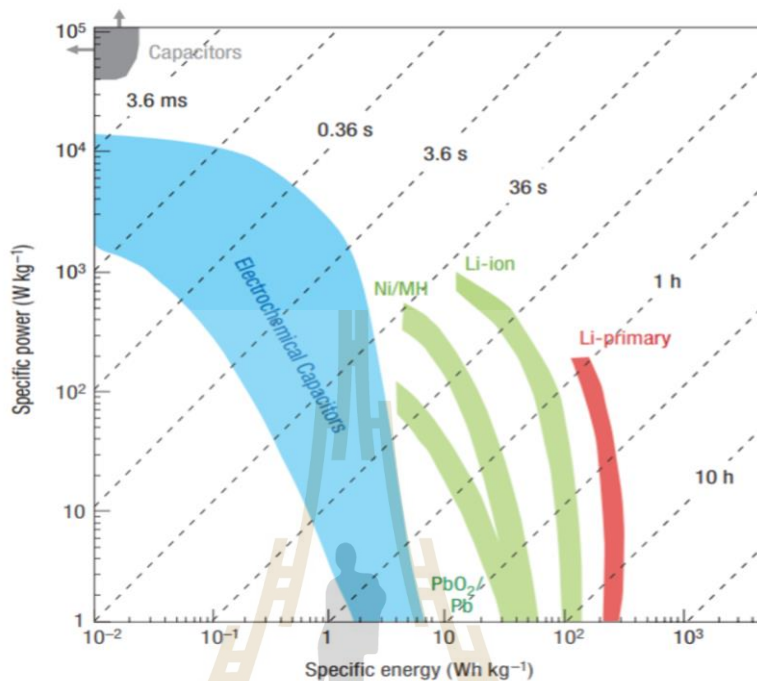


**Figure 1.1** Estimated energy and power density of SCs compared with conventional capacitors and commercially available batteries.

Owing to their superior properties, SCs are promising candidate for future electrical energy storage devices. They have been proposed and already used in many applications, such as, portable electronic devices, computer memory backup systems, low-emission hybrid electric vehicles, crane, emergency door on airplane and other applications which require high power density or fast discharge process as shown in Figure 1.2.



**Figure 1.2** Photographs of commercial supercapacitors and their proposed applications.

Generally, SCs can be categorized into 3 types depending on their charge storage mechanisms. These are electrostatic double layers capacitors (EDLCs), pseudocapacitors and hybrid capacitors. The EDLCs physically store charges via reversible ion adsorption at the electrode/electrolyte interface, while the pseudocapacitors rely on a redox reaction that appears in surface and near surface of electrode. The hybrid capacitors utilize both EDLC and pseudocapacitor charge storage mechanisms. This thesis focuses only on the EDLCs. The EDLCs typically consist of three main components which are electrolyte, separator and electrode as shown in Figure 1.3. It is sometimes called symmetric supercapacitor since both electrodes are usually made of the same material. It is mentioned here that the EDLC can also exhibit the pseudocapacitive behavior depending on the electrode materials.

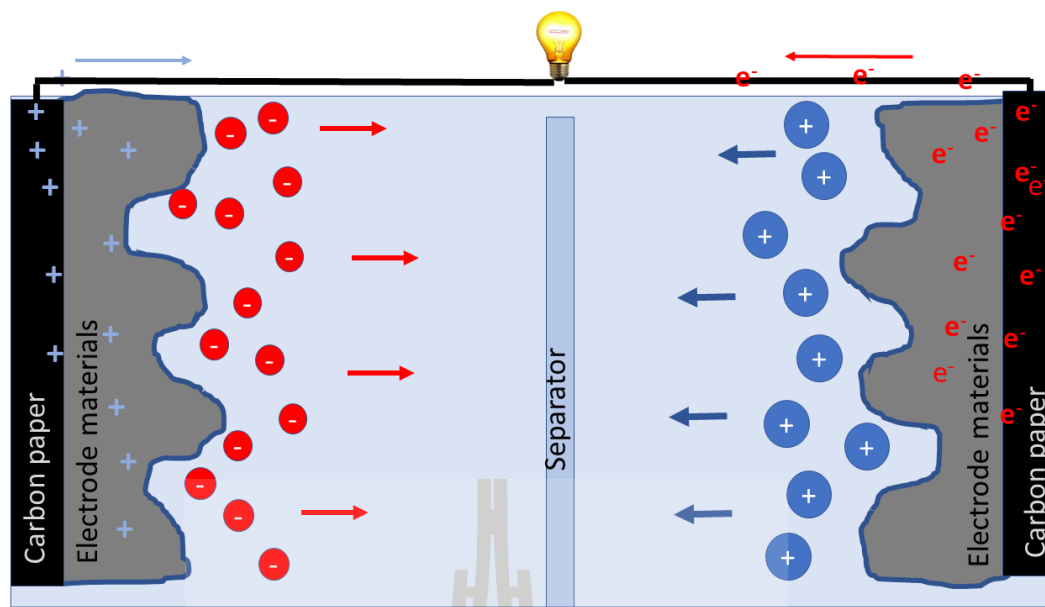


**Figure 1.3** Schematic representation of EDLC or symmetric supercapacitor.

An electrode material is the most important component of a supercapacitor. The power and energy-storage capabilities rely on the physical and chemical characteristics of the electrode material. Carbon-based materials have been typically used as electrode materials for EDLCs due to their abundance and low price, high surface area, high electrical conductivity, good wettability towards the electrolyte and electrochemically stable (Zhang and Zhao, 2009). Activated carbons (ACs) are the most widely used electrode materials today, while carbon nanotubes (CNTs) are of particular interest as they have a unique tubular porous structure and superior electrical properties, which favor fast ion and electron transportation (Chem. Soc. Rev., 2009, 38, 2520–2531). More recently, graphene, a new two-dimensional carbon nanostructure, has drawn a lot of attention as it possesses a large specific surface area and exceptionally high electronic properties.

Graphene oxide (GO), formerly call graphitic oxide, is a single layer of graphite with various oxygen containing functionalities, such as, epoxide, carbonyl, carboxyl, and hydroxyl groups. It is an intermediate material during graphene synthesis by the method of oxidation-exfoliation- reduction of graphite powder ((B. Xu et al., 2011). This material has many interesting properties, such as, highly flexible layered structure (Marco et al., 2017) very high the specific surface area (SSA) and easily tunable porous structure (Srinivas et al., 2012). It is theoretically predicted that the SSA of GO is as high as  $2600 \text{ m}^2 \text{ g}^{-1}$ , although, the experimentally measured SSA of lower than  $1000 \text{ m}^2 \text{ g}^{-1}$  have been reported (Vivekchand et al., 2008) (D. Zhou and Han, 2010) (Srinivas, Burrell, Ford, and Yildirim, 2011) (Montes-Navajas et al., 2013). Moreover, GO can be cost-effectively produced in a large scale using inexpensive graphite as a raw material. These properties have brought our attention to GO as a promising material for supercapacitor electrode. However, it is its low conductivity of lower than  $10^{-3} \text{ S cm}^{-1}$  (Gomez-Navarro et al., 2007) which limit its performance as an electrode material. This is a result of a large amount of  $\text{sp}^3$  hybridized carbon atoms bonded with the oxygen containing groups present in its structure (B. Zhao et al., 2012) (Robinson, Perkins, Snow, Wei, and Sheehan, 2008) (Strong et al., 2012).

In this thesis, I have proposed two steps to enhance the electrochemical properties of GO for use as supercapacitorelectrode material as schematically illustrated in Figure 1.4. In the first step, the intrinsic properties of GO were improved by reducing and doping with nitrogen. This was simply done by using a hydrothermal technique. Urea was used as nitrogen source. The supercapacitor coin cells using the prepared nitrogen doped reduced graphene oxide (N-rGO) as an electrode were assembled their electrochemical properties were also evaluated. The specific capacitance as high as  $145 \text{ F g}^{-1}$  was

achieved for the prepared N-rGO with urea content of 40% (w/v). Advanced surface science characterization techniques, such as, Raman spectroscopy, Fourier-transform infrared (FT-IR), X-ray photoelectron spectroscopy (XPS) indicated the successful of reduction and in cooperation of N into GO structure, therefore, enhancing the electrical conductivity and wettability. The presences of the nitrogen functionalities also provide an additional pseudocapacitance.

In the second step, the surface of the N-rGO electrode was treated with violet light laser (VLT) with a wavelength of 405 nm. This was done by our in-house laser scribing machine which is adapted from a commercial 3D printer. After the irradiation, the specific capacitance was enhanced up to  $214 \text{ F g}^{-1}$  for the prepared N-rGO with urea content of 40% (w/v), approximately 48% as compared with the untreated electrode. Moreover, it could maintain the capacitive retention of more than 94% after 10,000 cycles of charge/discharge. This is because the decrease in oxygen-containing functional groups such epoxy group and hydroxyl group, re-establishing C=C  $\text{sp}^2$  structure, and the exfoliation of surface that increases the porosity and specific surface area of the electrode.

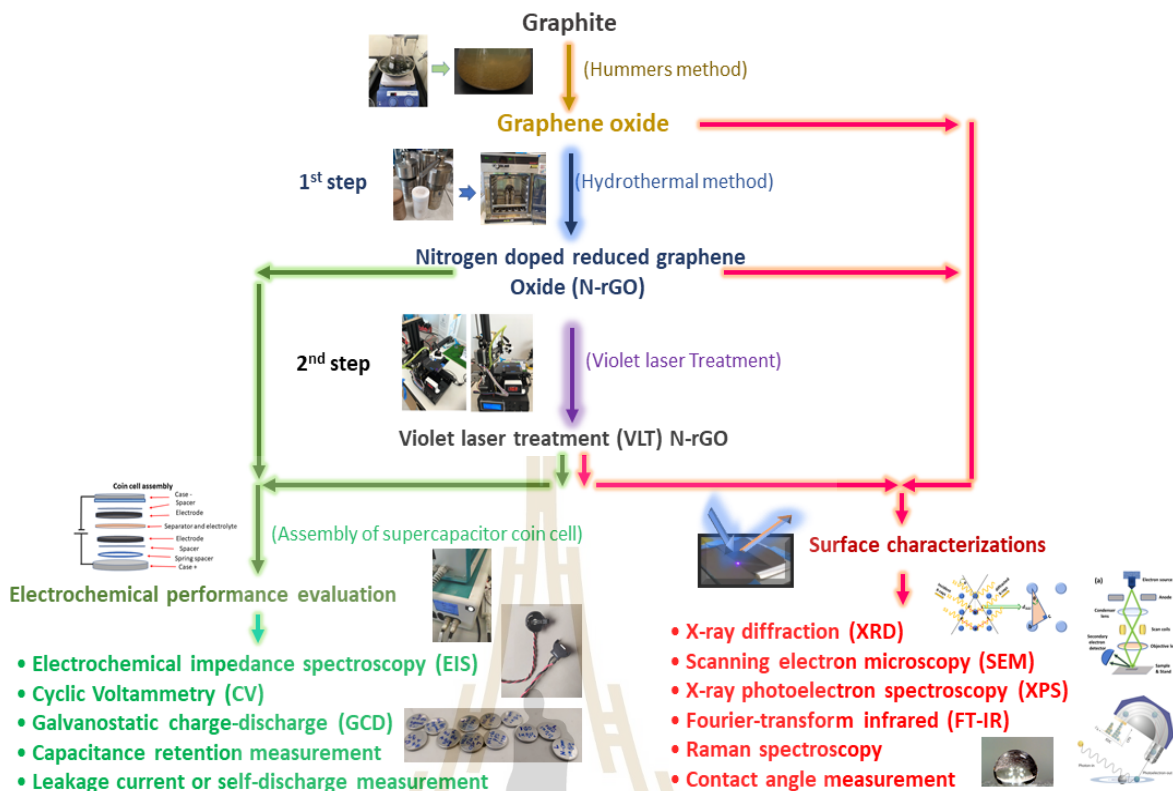


**Figure 1.4** Flow chart of the study.

## 1.2 Objectives and structure of this thesis

The objectives of this thesis are as follows:

- To enhance the electrochemical properties of GO for application as supercapacitor electrode material.
- To study the electrochemical and surface properties of N-rGO.
- To study the effect of violet laser treatment on the electrochemical and surface properties of N- rGO.

This thesis is structured as follows. The first chapter, Chapter I, provides the background and significance of the study. The objective, scope and limitation of the thesis are also given. Chapter II gives some basics of supercapacitors and reviews the

research related to this thesis. Chapter III explains the experiment and techniques used in this thesis. Chapter IV presents the experimental results and discussion focusing on the electrochemical properties and characterizations of GO, rGO, N-doped rGO and VLT N-doped rGO. In the final chapter, Chapter V, the conclusions are given. An appendix including my presentation experience in energy storage research field is also presented in the end of this thesis.

### 1.3 Scope and limitations

- GO was reduced and doped with nitrogen by using urea as nitrogen source.
- The surface of the prepared electrode materials was treated with violet laser by laser scribing technique.
- The prepared electrode materials were characterized by X-ray diffraction (XRD), scanning electron microscope (SEM), Raman spectroscopy, Fourier-transform infrared (FT-IR), X-ray photoelectron spectroscopy (XPS), and contact angle measurement techniques.
- The electrochemical properties were evaluated by using electrochemical impedance spectroscopy (EIS), cyclic voltammetry (CV) and galvanostatic charge/discharge (GCD) and self-discharge or leakage current measurement techniques.

# CHAPTER II

## LITERATURE REVIEW

### 2.1 Supercapacitors (SCs)

Supercapacitors (SCs) also known as electrochemical capacitors, ultracapacitors, or hybrid capacitors are electrical energy storage devices which have very high capacity and low internal resistance. They can be divided into three types based on their charge storage mechanisms, which are electrostatic double layer capacitance (EDLC), pseudocapacitor and hybrid capacitor.

#### 2.1.1 Electrostatic double layer capacitors (EDLCs)

The electrostatic double layer capacitors (EDLCs) physically store charges via reversible ion adsorption at the interface between a high-surface area of electrode and electrolyte as shown in Figure 2.1 (Zhang and Zhao, 2009; Winter and Brodd, 2004; Burke, 2000; Trasatti and Kurzweil, 1994). No electrochemical reaction is involved in the electrode material during the charging and discharging processes. This charge storage mechanism allows very fast energy uptake and delivery. It is also very stable during millions of charge/discharge cycles. The capacitance of EDLC is strongly dependent on the surface area of the electrode materials that is accessible to the electrolyte ions.

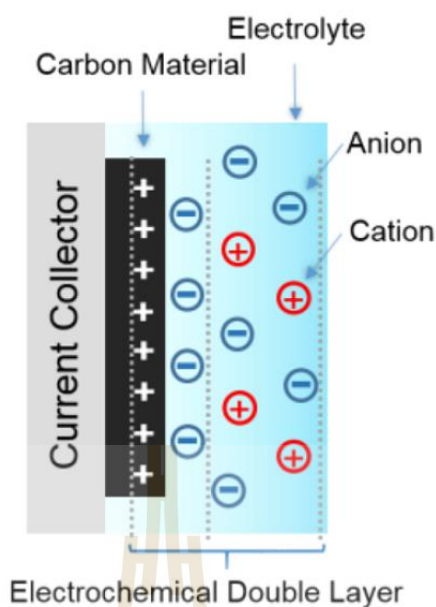


**Figure 2.1** Schematic of charge-storage mechanism for EDLC (Shao et al., 2018).

The capacitance of EDLC can be considered as that of a parallel-plate capacitor which can be explained by equation 2.1.

$$C = \frac{\epsilon_r \epsilon_0 A}{d} \quad (2.1)$$

where  $C$  is the electrostatic double layer capacitance (F or farad),  $\epsilon_r$  is the dielectric permittivity of sample materials ( $\text{F m}^{-1}$ ),  $\epsilon_0$  is the permittivity of free space equal  $8.854 \times 10^{-12}$  ( $\text{F m}^{-1}$ ),  $A$  is the surface area ( $\text{m}^2$ ) and  $d$  is the thickness of the double layer (m) which exhibited in order of  $5\text{-}10 \text{ \AA}$ , depend on electrolyte concentration (Kötz and Carlen, 2000).

### 2.1.2 Pseudocapacitors

The pseudocapacitors or redox supercapacitors employ fast and reversible surface or near surface reactions (via redox reaction at the vicinity (a few nanometers)) of the surface (Yu et al., 2015)). This charge storage mechanism provides the advantage of

fast charge-discharge (high power density) and high energy density (Augustyn et al., 2014). Three different faradaic mechanisms, which are underpotential deposition, redox pseudocapacitance and intercalation pseudocapacitance, can involve in the charge storage mechanisms as illustrated in Figure 2.2. The underpotential deposition (B. Conway, 1993) occurs when ions deposit on a 2-dimensional (2D) metal–electrolyte interface at potentials positive to their reversible redox potential for example  $H^+$  on Pt or  $Pd^{2+}$  on Au (Sudha and Sangaranarayanan, 2002) (Herrero, Buller, and Abruña, 2001). The redox pseudocapacitance exhibits at some extent of conversion of reduced species which is electrochemically absorbed onto the surface or near surface of oxidized species (or vice versa) in a Faradaic redox system i.e.,  $RuO_2$  (Bi et al., 2010) or  $MnO_2$  (Brian E Conway, Birss, and Wojtowicz, 1997). The intercalation pseudocapacitance occurs where ion intercalation into a redox-active material occurs with no crystallographic phase change and in a time scale close to that of an EDLC i.e.,  $Nb_2O_5$  (Kong et al., 2014). Typically, the pseudocapacitances can provide much higher energy density, but lower power density than the EDLCs. This is because the redox processes are normally slower than non-faradaic processes.

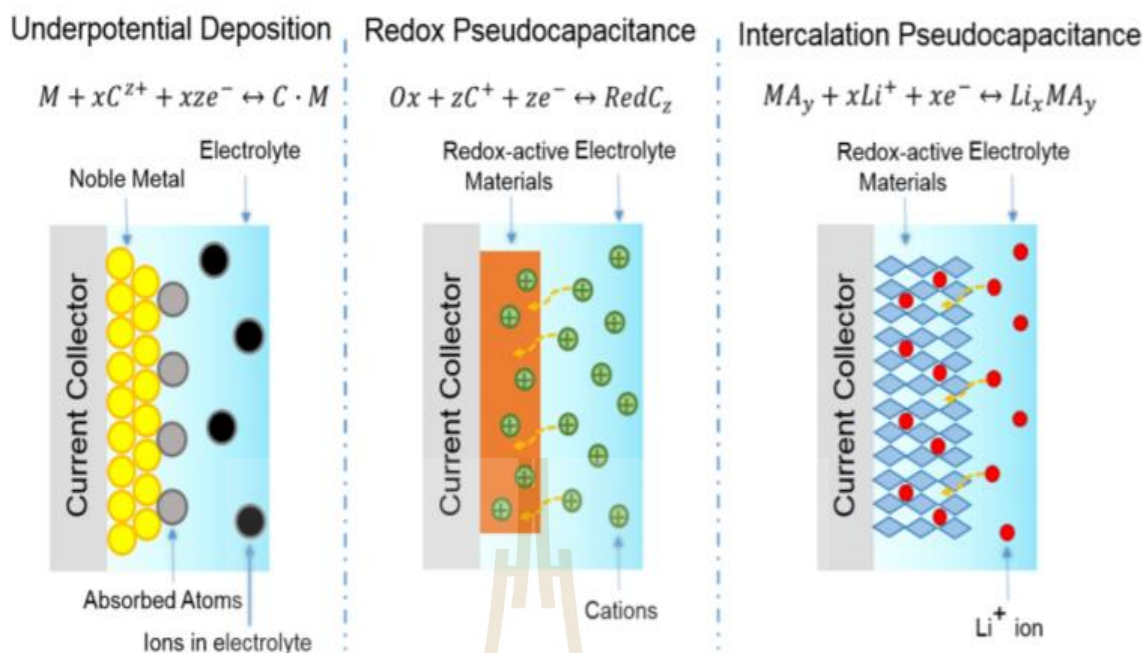


**Figure 2.2** Schematics of charge-storage mechanisms for different types of pseudocapacitive electrodes: underpotential deposition, redox pseudocapacitor, and ion intercalation pseudocapacitor (Shao et al., 2018).

### 2.1.3 Hybrid capacitors

The hybrid capacitors utilize both EDLC and pseudocapacitor charge storage mechanisms. It is generally an asymmetric supercapacitor. One electrode stores charge by the faradaic process while another electrode stores charge based on the electrostatic double layer capacitive mechanism (Shao et al., 2018). A correct combination of the electrode can increase the cell voltage and hence enhance the energy and power densities (Int. J. Electrochem. Sci., 11 (2016) 10628). However, the faradaic electrode exhibits low cyclic stability which is the main drawback of hybrid capacitors compared with EDLCs.

## 2.2 Components of supercapacitors

### 2.2.1 Electrode

Electrode is the main component of supercapacitor. The capacitance of supercapacitor strongly depends on the properties of electrode materials, especially conductivity, specific surface area, wettability, and pore size. An electrode with high surface area tends to provide high specific capacitance because charges are stored on the surface (Yu et al., 2015). However, the correlation between specific surface area and the specific capacitance of electrode materials is still unclear. The increase of specific surface area with simultaneous increase of average pore size does not result in the increase of the specific capacitance (Shi, 1996). It is recognized that the relationship between pore size of electrode and ions size of electrolyte is also crucial. Macropores can facilitate the penetration and wetting of electrolyte ions to the interior surface and hence improve the rate capability and cycle stability of the electrodes. Mesopores can provide a large accessible surface area for ion transport/charge storage, and micropores contribute to increasing the specific surface area and specific capacitance. For instance, carbon-derived-carbide sample with pore size as 0.7 nm will provide the highest normalized capacitance with the ionic liquid electrolyte which has the size of about  $7.6 \text{ \AA} \times 4.3 \text{ \AA}$  for cation and  $7.9 \text{ \AA} \times 2.9 \text{ \AA}$  for anion (Largeot et al., 2008). Optimization of pore size, pore structure, surface properties and conductivity of the electrode materials are therefore crucial for the electrochemical performances of supercapacitors. The specific capacitance and rate capability are also dependent on both electronic and ionic conductivity. High electronic and ionic conductivity will help to maintain the rectangular nature of cyclic voltammetry (CV) curve and symmetry of galvanostatic charge/discharge (GCD)

curves. They also reduce the specific capacitance losses as scan rates/current densities are increased. (Yu et al., 2015).

Various materials have been applied and used as electrode materials. Carbon materials, such as, carbon nanotube (K. An et al., 2001), nanoporous carbon (Jeon et al., 2015), carbon nanofiber (C. Kim and Yang, 2003), graphene (Liu, Yu, Neff, Zhamu, and Jang, 2010), and reduced graphene oxide (El-Kady, Strong, Dubin, and Kaner, 2012) have been intensively used for EDLCs. Metal oxides, such as, RuO<sub>2</sub>, MnO<sub>2</sub> and NiO and conducting polymer, such as, poly(3,4-ethylenedioxythiophene) (PEDOT) and polyaniline (W. Li, Chen, Zhao, Zhang, and Zhu, 2005) have been employed as electrode materials that provide pseudo capacitance (C.-C. Hu, Chang, Lin, and Wu, 2006) (Frackowiak, 2007). Although these materials exhibit a reduction-oxidation process (Sharma et al., 2010) which provides higher electrode performances, they suffer from poor stability during cycling due to redox reactions (Xiang, Yin, Wang, and Zhang, 2016) (Sun et al., 2019).

### 2.2.2 Electrolyte

Electrolyte is a material that provides pure ionic conductivity between the positive and negative electrodes of a cell (Winter and Brodd, 2004). It therefore play an important role to determine the operating voltage and power density of supercapacitor. Supercapacitor cell voltage is limited by the electrolyte decomposition at high potential (Simon and Gogotsi, 2008). There are 3 types of electrolytes which are ionic electrolyte, such as, 1-ethyl-3-methylimidazolium acetate (EMIM Ac), organic electrolyte, such as, 1.0 M of tetraethylammonium tetrafluoroborate ((C<sub>2</sub>H<sub>5</sub>)<sub>4</sub>NBF<sub>4</sub>) in acetonitrile, and aqueous electrolyte such 1.0 M H<sub>2</sub>SO<sub>4</sub> in DI water.

### 2.2.3 Separator

Separator is a physical barrier between two electrodes to prevent electrical shorting but allow positive and negative ions go through. The separator can be a gelled electrolyte, or microporous plastic film or other porous inert materials filled with electrolyte (Winter and Brodd, 2004).

## 2.3 Graphene oxide (GO)

Graphene oxide (GO) is a two-dimensional crystal structure formed by a flat monolayer of carbon atoms arranged in a hexagonal lattice (Geim and Novoselov, 2007). It contains various oxygen functionalities, such as, epoxide (C-O-C), carbonyl (C=O), phenol (Ph-OH), carboxyl (COOH) and hydroxyl (C-OH) (Gómez-Navarro et al., 2010) (Lerf, He, Forster, and Klinowski, 1998), and its layers terminate with C-OH and -COOH groups (Lerf et al., 1998) (Rao et al., 2014; Li et al., 2013; Diez-Betriu et al., 2013). Although various structural models have been proposed which are based on the observed various oxygen-containing functional groups (Lerf et al., 1998), the precise structure of GO is still uncertain because it has nearly amorphous structure. The possible structure of graphene oxide is illustrated as in Figure 2.5.

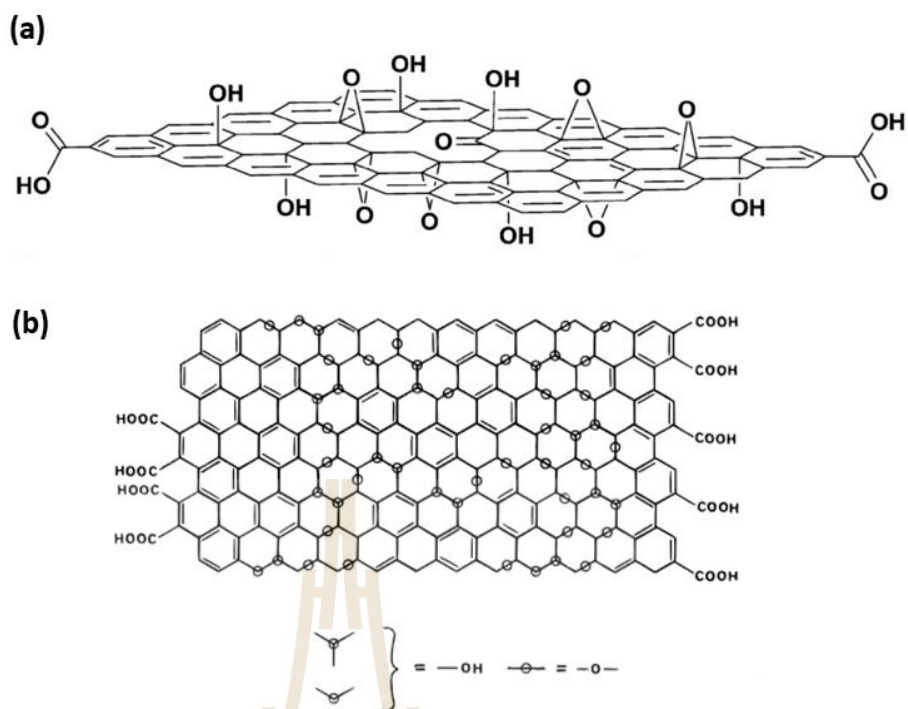


**Figure 2.3** Possible GO structure proposed by (a) Compton (Compton and Nguyen, 2010) and (b) Lerf (Lerf et al., 1998).

Today GO can be routinely synthesized from graphite. Several techniques can be employed, such as, Brodie (Brodie, 1859), Staudenmaier (Staudenmaier, 1898), Hofmann (Hofmann and Holst, 1939) and Hummers methods (Hummers Jr and Offeman, 1958). Among these techniques, the Hummers method is the most widely used due to its ease, simplicity and short time process.

GO exhibits many interesting properties which is promising for electrode material, such as, highly flexible layered structure (Marco et al., 2017), very high the specific surface area (SSA) and easily tunable porous structure (Srinivas et al., 2012). It is theoretically predicted that the SSA of GO is as high as  $2600 \text{ m}^2 \text{ g}^{-1}$ , although, the experimentally measured SSA of lower than  $1000 \text{ m}^2 \text{ g}^{-1}$  have been reported (Vivekchand et al., 2008) (D. Zhou and Han, 2010) (Srinivas et al., 2011) (Montes-

Navajas et al., 2013). Moreover, GO can be cost-effectively produced in a large scale using inexpensive graphite as a raw material (X. Huang, Qi, Boey, and Zhang, 2012).

Although GO and conducting polymers or metal oxides nanocomposites with have been widely studied, as they exhibit high capacitances and good cycling performances (H. Wang, Hao, Yang, Lu, and Wang, 2009), only few studies have been reported on the direct use of GO as electrode material. Xu et al. reported a systematic study on GO as the electrode material for supercapacitors. It was found that the highest specific capacitance of  $189 \text{ F g}^{-1}$  can be reached. It has also pointed out that the attached oxygen-containing functional groups on GO basal planes can provide an additional pseudo-capacitance [Energy Environ. Sci., 2011, 4, 2826–2830]. The main limitations of use of GO as a supercapacitor electrode are; (i) its low effective surface area of  $1000 \text{ m}^2 \text{ g}^{-1}$  in experiment, lower than the number in theory (Montes-Navajas et al., 2013) (Srinivas et al., 2011) (Vivekchand, Rout, Subrahmanyam, Govindaraj, and Rao, 2008) (D. Zhou and Han, 2010), (ii) low measured sheet resistance of  $\sim 4 \times 10^{10} \Omega$  per square (Gilje, Han, Wang, Wang, and Kaner, 2007), and (iii) many oxygen functional groups on its structure, this may cause capacitor instability, increase series resistance and increase deterioration of capacitance (Pandolfo and Hollenkamp, 2006) (Azaïs et al., 2007).

## 2.4 Reduction of graphene oxide and laser irradiation

To improve the properties of GO, many research have attempted to remove oxygen functional groups from its structure and exfoliated GO sheet to lower sheet. This product material is known as reduced graphene oxide (rGO). Various techniques can be used to tranfrom GO to rGO, such as, chemical reaction, microwave exfoliation, thermal process, and laser irradiation (TK, Nair, Abraham, Beegum, and Thachil, 2014) (Stoller, Park,

Zhu, An, and Ruoff, 2008) (Y. Wang et al., 2009) (Shin et al., 2009) (Y. Zhou, Bao, Tang, Zhong, and Loh, 2009) (Y. Zhu et al., 2010) (Vivekchand et al., 2008). The chemical and thermal methods are most frequently used. The chemical reduction method is scalable, however, it involves the use of hazardous reducing agents, such as hydrazine or sulfonate. This can leave some residues after the process and significantly affect the structures and properties of rGO (D. Yang and Bock, 2017) (Y. Huang et al., 2018). The thermal reduction process can produce rGO with high surface area which may approach the surface area of pristine graphene. However, it employs high temperatures exceeding 1000 °C which can generate various defects in the structure (D. Yang and Bock, 2017). Recently, hydrothermal method has been proposed to reduce GO. This thermal treatment technique takes place inside a closed vessel in an aqueous medium heated at subcritical temperatures (120–200 °C) under self-generated pressure (Barra et al., 2021). It is simple, fast, cost effective and environmentally friendly. It is also possible to simultaneously reduce the oxygen functional groups and dope with heteroatoms or functionalize the structure with active functional groups by the addition of reducing agents. Long et al. showed that nitrogen doped rGO sheet can be prepared by a combination of chemical and hydrothermal reduction method (Long et al., 2010). This was achieved via reduction of GO colloidal solution in the presence of ammonia and hydrazine under a hydrothermal environment.

Previous studies have shown that doping or incorporating heteroatoms, such as, nitrogen, boron, phosphorous and sulfur to the structure carbon-based electrode materials could modify the chemical reactivity, electrical conductivity, surface activity and mechanical properties which are essentially for supercapacitor electrode material (Hulicova-Jurcakova, Seredych, Lu, and Bandosz, 2009) (Lota, Grzyb, Machnikowska,

Machnikowski, and Frackowiak, 2005) (D.-W. Wang, Li, Chen, Lu, and Cheng, 2008). Among these dopants, nitrogen has been widely studied in the last few years. Lee et al. reported the synthesis N doped rGO by microwave-assisted hydrothermal method (Y.-H. Lee, Chang, and Hu, 2013). Pyridinic-N, pyrrolic-N, pyridine-N-oxides were observed in the structure of rGO, as shown in Figure 2.8, which provided pseudocapacitive behavior and the total specific capacitance of  $218 \text{ F g}^{-1}$  was achieved. Fan et al. synthesized nitrogen-rich graphene-incorporated nitrogen-containing hydrothermal carbons from GO by using a hydrothermal method and glucosamine as nitrogen source (Fan, Yu, Yang, Ling, and Qiu, 2014). The synthesized composite exhibited the highest specific capacitance of  $218 \text{ F g}^{-1}$  at  $0.1 \text{ A g}^{-1}$  in  $6 \text{ M KOH}$  aqueous solution.

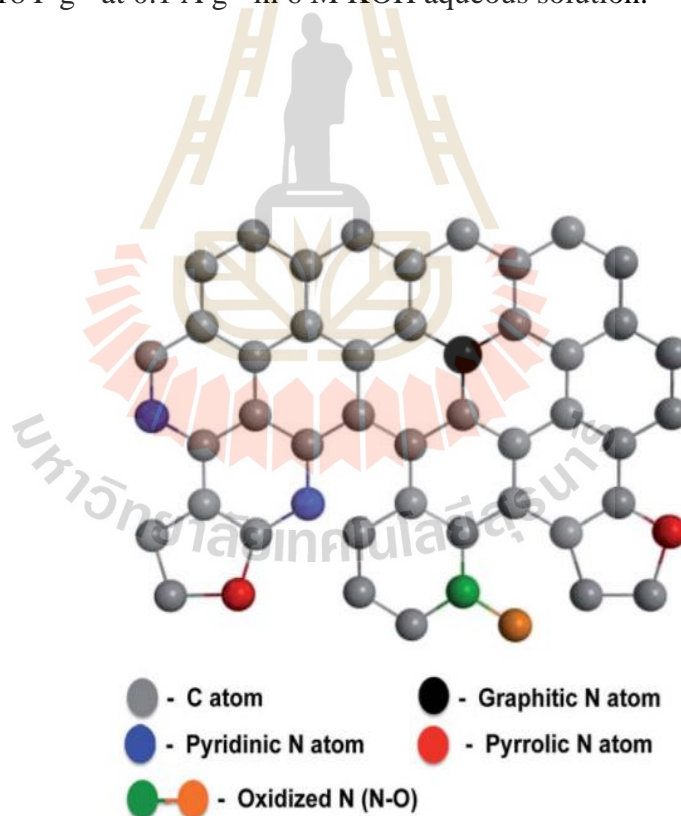


**Figure 2.4** Possible structure of nitrogen doped rGO (Faisal et al., 2017).

In addition to nitrogen doping, sulfur doping and nitrogen and sulfur co-doping have become attractive. Wang et al. reported the synthesis of thiophene–sulfur doped rGO via the ethanol-thermal reaction (Z. Wang et al., 2014). Benzyl disulfide and ethanol were used as S doping source and reducing agent, respectively. It was demonstrated that the sulfur doping can enhance the conductivity of rGO better than nitrogen doping due to its stronger electron donor ability. Chen et al. reported the synthesis of sulfur-doped three-dimensional (3D) porous rGO hollow nanospheres framework which exhibited a high specific capacitance of  $343 \text{ F g}^{-1}$ , good rate capability and excellent cycling stability in aqueous electrolytes (X. Chen et al., 2014). This excellent performance was believed to be due to the synergistic effect of sulfur-doping enhancing the electrochemical activity and 3D porous hollow nanospheres framework structure facilitating ion diffusion and electronic transfer. Rochman et al. prepared the N and S doped rGO via hydrothermal method (Rochman, Wahyuningsih, Ramelan, and Hanif, 2019). Wang et al. investigated the nitrogen and sulfur co-doped graphene prepared via a one-pot hydrothermal route using GO and L-cysteine as starting material. A good electrochemical performance with a specific capacitance of  $566\text{-}343 \text{ F g}^{-1}$  was observed (T. Wang, Wang, Wu, Xia, and Jia, 2015).

Recently, there have been reports on the reduction of GO by using photo-irradiation, such as, UV induced catalytic reduction, photo-thermal reduction using a pulsed Xenon flash, and laser reduction (D. Yang and Bock, 2017). This technique does not rely on the use of chemicals or high temperatures and shorten the reaction time from several hours to a few minutes (Yang, D., and Bock, C. (2017)). The reduction process can be also performed on dry GO films or GO flakes as starting materials. The first use of laser irradiation was reported by Strong et al. (Strong et al., 2012). Infrared laser with a

wavelength of 788 nm was irradiated on the GO electrode by using Light Scribe patterning technology. After irradiation, the decrease in disorder state (epoxide, hydroxyl, and carbonyl) and the re-establishment of C=C bonds in the carbon network was observed in the XPS spectra as shown in Figure 2.11. In 2012, Eigler et al. employed a green light laser to reduce graphene oxide prepared using diluted dispersion of GO on a ZnSe window. This reduced GO film showed the decrease of  $I_D/I_G$  which implied that this technique impact to local defects on GO structure (Eigler, Dotzer, and Hirsch, 2012)

In 2012, El-Kady et al. applied infrared laser scribing technique from a computerized lightscribe DVD on GO supercapacitor electrode and observed that it could enhance the specific capacitance up to  $276 \text{ F g}^{-1}$  (El-Kady et al., 2012). Dongfang Yang and Christina Bock reported the use of KrF excimer laser with a wavelength of 248 nm to reduce GO in aqueous solution. Then, the product material was dropcasted on Si substrates and used as electrode for supercapacitor. It exhibited the specific capacitance of  $130 \text{ F g}^{-1}$  (D. Yang and Bock, 2017). In 2020, Yar et al. proposed the optical reduction of freeze-dried GO by using laser engraver (Yar et al., 2020). The specific capacitance as high as  $161 \text{ F g}^{-1}$  was achieved.

From the previous studies, two effects of laser irradiation were attributed to the enhancement of electrode performance; i) laser light can create surface exfoliation as shown in Figure 2.10.

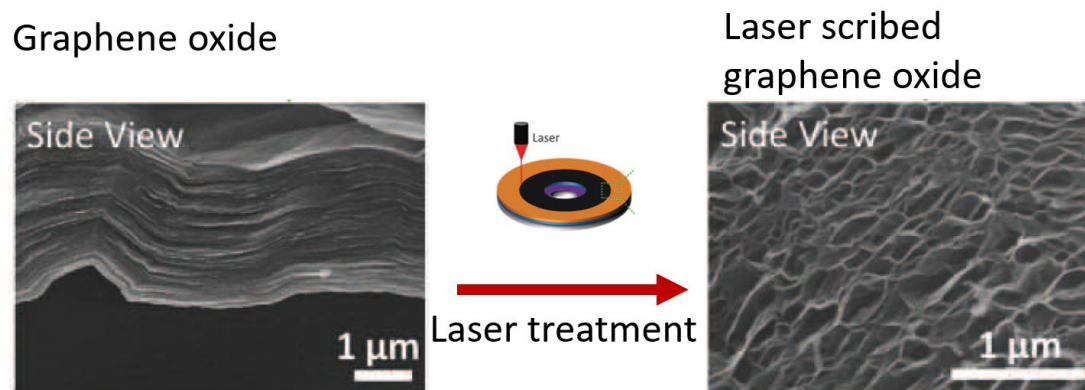


**Figure 2.5** SEM images of the surface of GO before and after laser irradiation graphene (rGO) (El-Kady et al., 2012).

Laser can reduce oxygen functional groups. Figure 2.11 shows the XPS spectra of GO before and after irradiation with infrared laser. The measured C1s peak showed the reduction of disorder or oxygen functional groups with increasing of  $sp^2$  hybridization state (Strong et al., 2012)

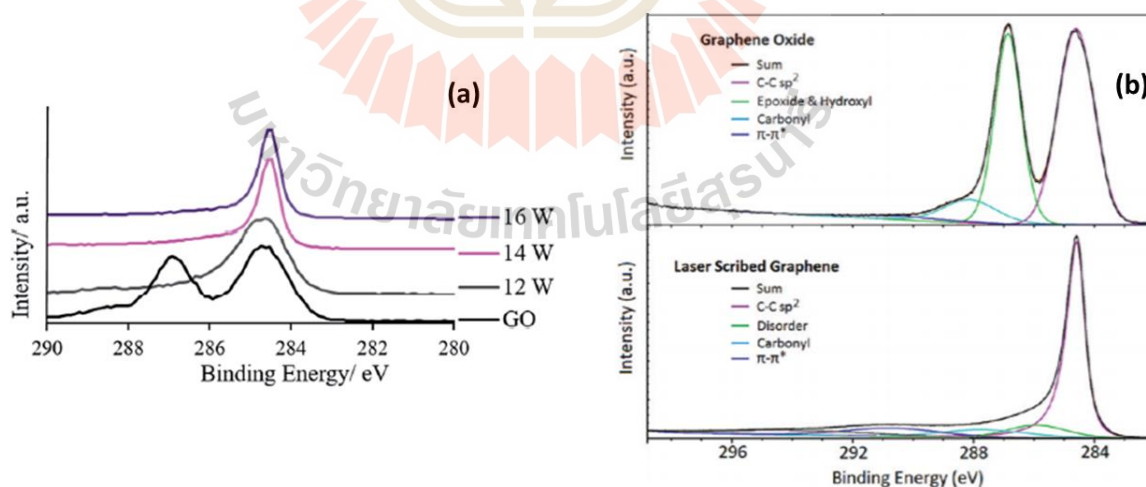
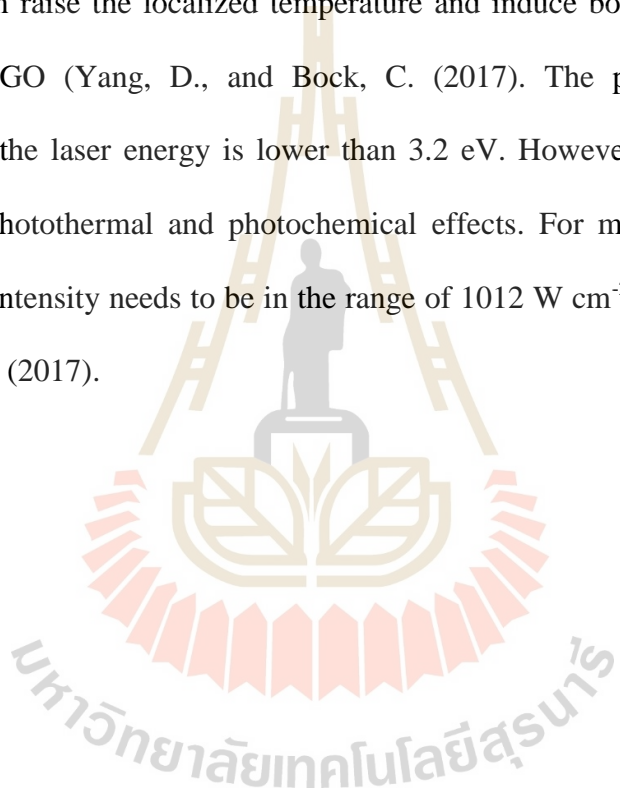


**Figure 2.6** C1s XPS peak of GO before and after irradiation with infrared laser (Strong et al., 2012).

In the photo reduction process, two main mechanisms are dominate which are photochemical and photothermal process (Yang, D., and Bock, C. (2017). The photochemical involves the absorption of photon and breaking the covalent bond. It has been reported that the photon energies of larger than 3.2 eV ( $\lambda < 390$  nm) is required for photo-reduction of GO (Smirnov, Arbuzov, and Shulga, 2011). In photothermal process, the electrons can absorb energy from photons, and the excited electrons can heat up the lattice which can raise the localized temperature and induce bond breaking resulting in deoxidation of GO (Yang, D., and Bock, C. (2017). The photothermal process is dominant when the laser energy is lower than 3.2 eV. However, most laser reductions may use both photothermal and photochemical effects. For multiphoton ionization to occur, the laser intensity needs to be in the range of  $10^{12}$  W cm<sup>-2</sup> to  $10^{16}$  W cm<sup>-2</sup> (Yang, D., and Bock, C. (2017).



## **CHAPTER III**

### **EXPERIMENTS AND TECHNIQUES**

In this work, graphene oxide (GO) was synthesized from graphite powder and then its properties were improved in two steps. In the first step, GO was reduced and doped with nitrogen. This was simply done by a conventional hydrothermal method and urea was used as a nitrogen source. In the second step, the surface of the prepared nitrogen doped reduced graphene oxide (N-rGO) was treated with violet laser. This was performed by the in-house violet laser scribing machine. The prepared samples were consequently prepared as electrodes and their electrochemical properties were evaluated by using galvanostatic charge/discharge (GCD), cyclic voltammetric (CV), electrochemical impedance spectroscopy (EIS), and leakage current measurement techniques. The prepared electrodes materials were also characterized by using X-ray diffraction (XRD), fourier transform infrared spectroscopy (FT-IR), scanning electron microscopy (SEM), Raman spectroscopy (Raman), X-ray photoelectron spectroscopy (XPS), and water contact angle measurement. All experiments and techniques used in this thesis are described in this chapter.

#### **3.1 Material preparations**

All chemicals used in this work were of analytical reagent grade. Water used is ultrapure (Milli Q water, resistivity of  $18.2 \text{ M}\Omega \text{ cm}^{-1}$ ). Graphite powder and acetylene black (AB) were purchased from Thai Carbon and Graphite Co. Ltd. and Carbot

(VXC72R LOT-4207037), respectively. Poly-(vinylidene fluoride) (PVDF), N-methyl-2-pyrrolidone (NMP), Sulfuric acid ( $\text{H}_2\text{SO}_4$ ) and Urea ( $\text{NH}_2\text{CONH}_2$ ) were purchased from Sigma Aldrich, USA.

### 3.1.1 Graphene oxide

GO was synthesized from graphite powder according to the modified Hummers method (Hummers Jr and Offeman, 1958). All processes were done in hood for safety. The preparation process is schematically shown in Figure 3.1 and briefly explained as follows:

- 10 g of graphite powder and 5 g of sodium nitrate ( $\text{NaNO}_3$ ) were dispersed in 200 ml of 98% sulfuric acid ( $\text{H}_2\text{SO}_4$ ), and it was stirred for 2 hours.
- 30 g of potassium permanganate ( $\text{KMnO}_4$ ) was carefully added and, then it was continuously stirred for 12 hours.
- 280 ml of DI water was slowly added.
- 30 ml of 30% hydrogen peroxide ( $\text{H}_2\text{O}_2$ ) was carefully dropped into the solution, and it was continuously stirred for 30 minutes.
- 720 ml of DI water was poured into the obtained brown solution, and it was continuously stirred for 30 minutes. The pH of the solution was adjusted to 6-7 using DI water.
- The brown solution of GO was filtered and washed with several DI water.



**Figure 3.1** Preparation of graphene oxide.

### 3.1.2 Nitrogen doped reduced graphene oxide (N-rGO)

N-rGO with different nitrogen doping contents were synthesized from the prepared GO. This was done by using conventional hydrothermal method. Urea (NH<sub>2</sub>CONH<sub>2</sub>) was used as nitrogen source. The synthesis process is briefly explained as follows:

- 5 g of GO was dispersed in 25 ml of the urea in DI water solutions with urea contents of 20%, 40%, and 60% (w/v). The subsequently prepared samples were labeled as N-rGO20, N-rGO40, N-rGO60, respectively.
- The mixtures were transferred into a 100 ml Teflon-lined stainless-steel hydrothermal chamber. They were heated to 180 °C with a heating rate of

10 °C min<sup>-1</sup> and maintained at this temperature for 12 hours before naturally cooling down.

- The obtained products were filtered and washed with DI water until reaching the pH of 6-7.
- The products were finally washed with ethanol and were dried at 80 °C for 6 hours.

### 3.1.3 Nitrogen and sulfur co-doped reduced graphene oxide (NandS-rGO)

In this work, nitrogen and sulfur co-doped reduced graphene oxide (NandS-rGO) was also synthesized. This was done by using conventional hydrothermal method, like the synthesis process of N-rGO. Thiourea (CH<sub>4</sub>N<sub>2</sub>S) was used as nitrogen and sulfur source.

## 3.2 Electrode fabrications

The prepared materials including GO, rGO, N-rGO and NandS-rGO were prepared as electrode as follows.

- 3.75 g of the prepared electrode material (GO, N-rGO and NandS-rGO) was firstly mixed with 0.75 g of polyvinylidene fluoride (PVDF) and 0.50 g of carbon black in 40 ml N-methyl-2-pyrrolidone (NMP).
- The mixture was ball-milled at 1000 rpm for 3 hours until a homogenous paste was obtained.
- The electrodes were fabricated by dropping 10 ml of the prepared paste on a carbon fiber paper (5×10 cm<sup>2</sup>) by a doctor-blade technique and were dried under ambient condition for 24 h as shown in Figure 3.2.

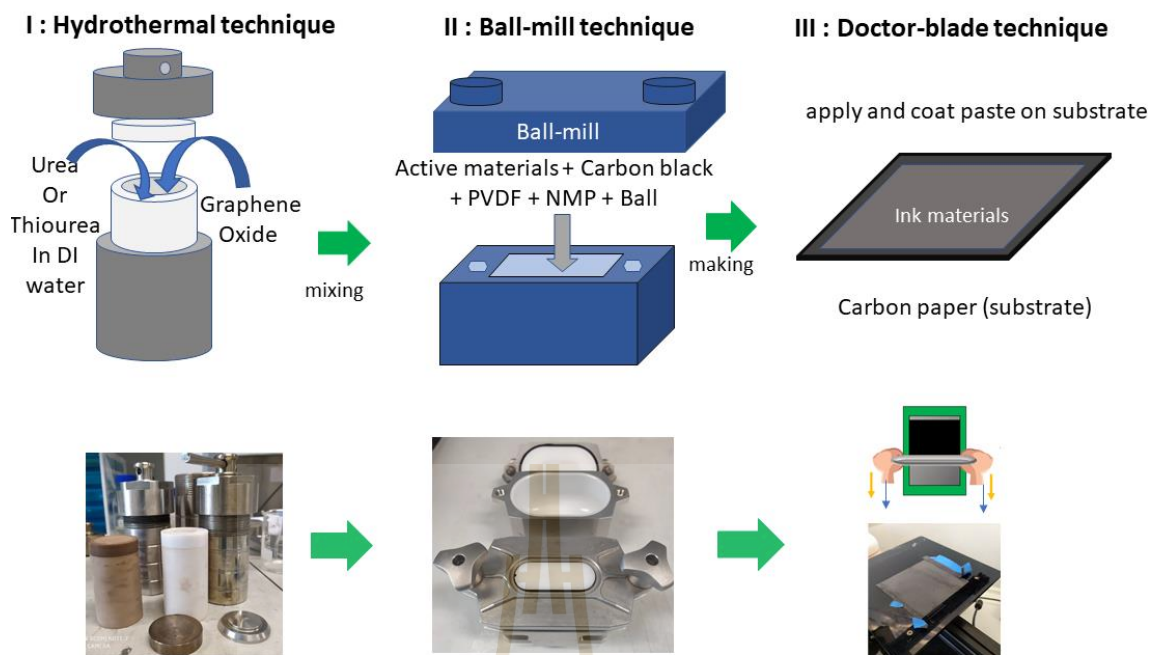


**Figure 3.2** Preparation of the electrodes for N-rGO and Nands-rGO.

### 3.3 Violet laser treatment

The violet laser treatment was performed by our in-house laser scribing machine. The machine is adapted from a commercial 3D printer structure (Tronxy, XY-2 pro I3). The photographs of the laser treatment machine used in this work and its components are shown in Figure 3.3.

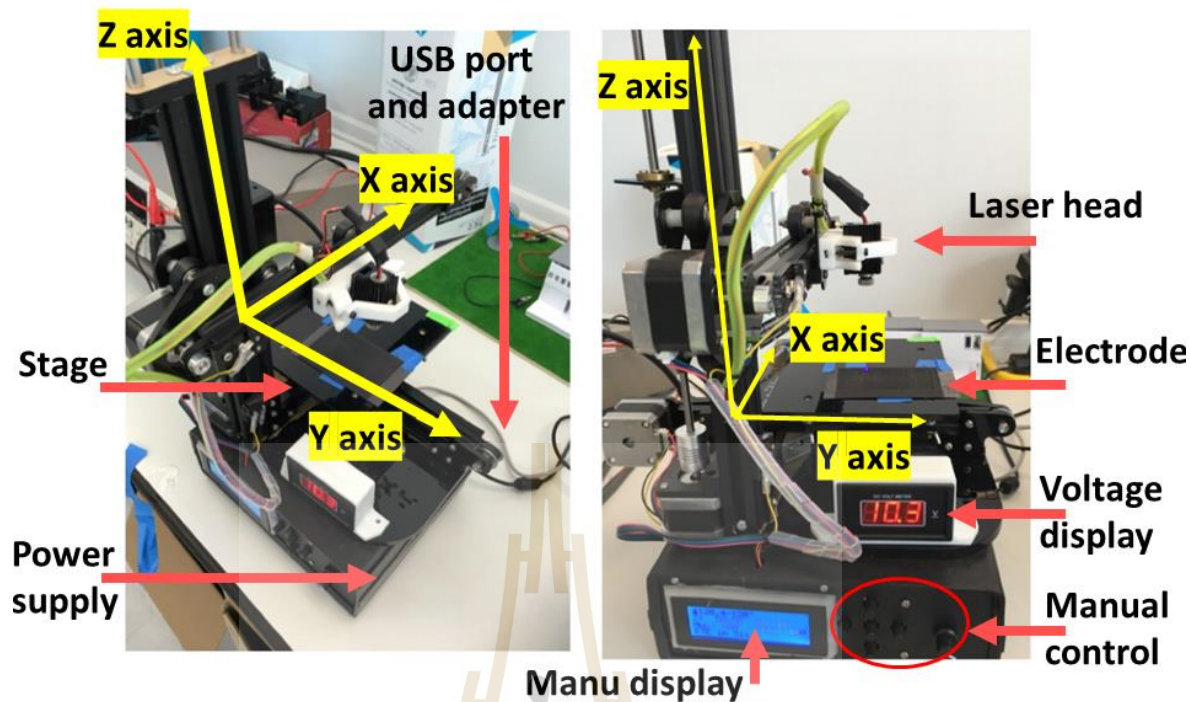


**Figure 3.3** Photographs of the in-house laser scribing machine adapted from a commercial 3D printer and its components.

The extruder of the 3D machine has been installed with a violet laser. The violet laser engraver with a wavelength of 405 nm was purchased from LaserGRBL. The maximum power of this laser was approximately 5 W. In this work, the laser power and intensity cannot be precisely controlled due to the limitation of our instrumentations. Its intensity was controlled by the voltage applied separately from the extruder. There is a monitor for voltage display as seen in Figure 3.3. The laser head is driven by using a step motor (model SL42STH34-1504A) which can move with a step angle of  $1.8^\circ$  (5% accuracy).

The machine also has the ability to write a pattern on an electrode as shown in Figure 3.4. This can be performed by creating a shap file (.gcode or .STL file) by the Inkscape program.

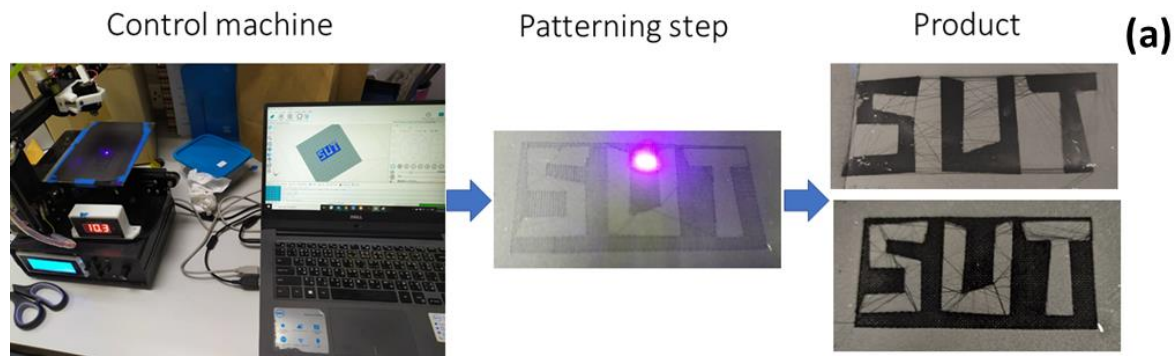


**Figure 3.4** Photographs of writing a pattern on an electrode by the laser scribing machine.

In this work, the prepared electrodes were scribed in a square shape with a size of 2 x 4 cm or larger depend on number of electrodes that we need to use as shown in Figure 3.5. The laser was irradiated perpendicular to an electrode. The distance between laser head and electrode was fixed at 8 cm. The beam size of laser treatment was approximately 0.1 mm. The laser was irradiated for different applied voltages (3, 7, and 10.2 V) and repeating cycles (3, and 5 cycles) to study the effect of laser intensity and exposure time, respectively. During the irradiation, the scribing speed was fixed at a high speed of  $10 \text{ cm s}^{-1}$  to avoid heating process that could damages the structure of electrode material (D. Yang and Bock, 2017).

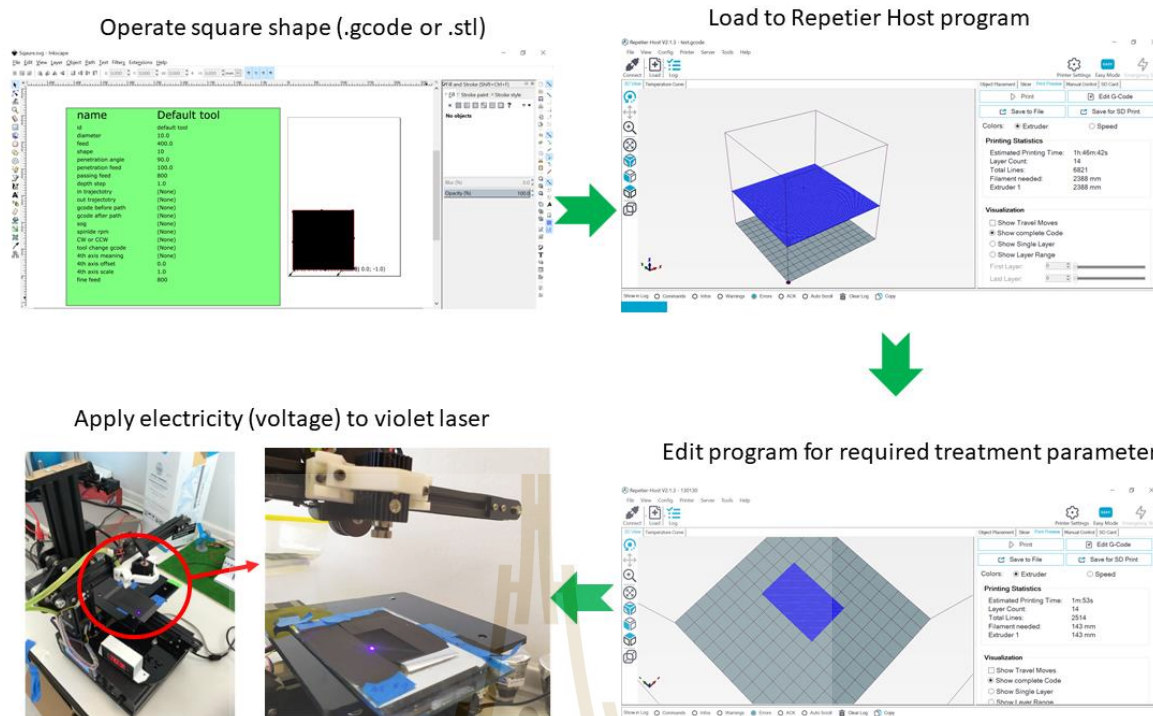
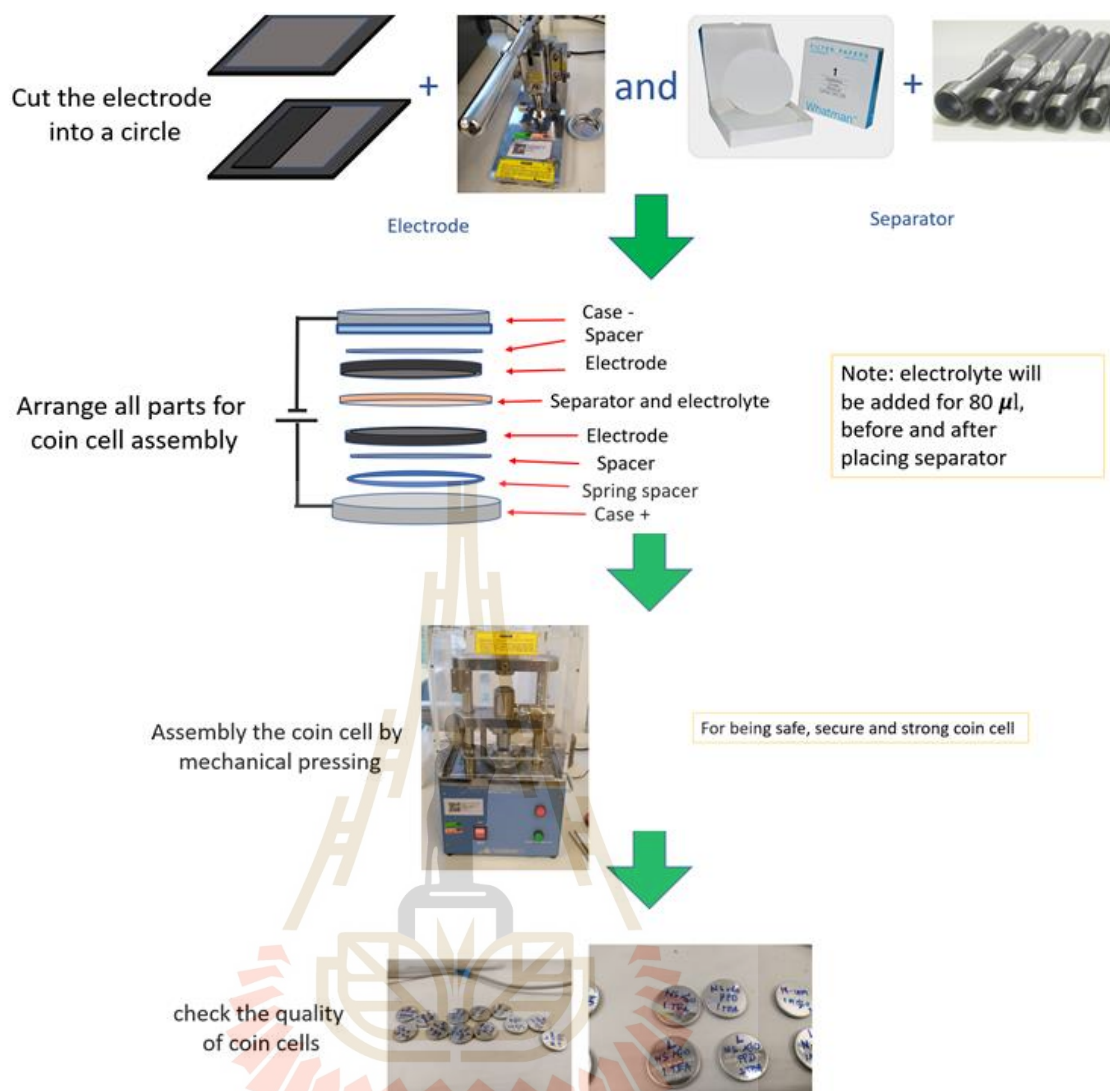


Figure 3.5 Laser irradiation process and control.

### 3.4 Supercapacitor coin cell assembly

The symmetric supercapacitor coin cells were assembled as follows.

- The prepared electrodes were cut into a circular shape with a diameter of 1.5 cm.
- A circular filter paper with a diameter of 1.8 cm was used as separator.
- 1 M  $\text{H}_2\text{SO}_4$  in DI water for 160  $\mu\text{l}$  was added as electrolyte.
- Assemble all parts as coin cell (CR2302) as shown in Figure 3.6
- The assembled cell was mechanically pressed and quality checked.



**Figure 3.6** Assembly of supercapacitor coin cells.

## 3.5 Electrochemical evaluations

### 3.5.1 Galvanostatic charge/discharge (GCD) measurement

The galvanostatic charge discharge (GCD) is a reliable method to evaluate the electrochemical capacitance of materials. This technique applies constant positive and negative currents to charge and discharge a material or device under fixed potential window. This process is often repeated for multiple cycles. GCD profiles, plot between cell potential and time, can be used to evaluate the quality of capacitive response, the

specific capacitance and capacitive retention of electrical energy storage. An example of a typical GCD profile is shown in Figure 3.8.

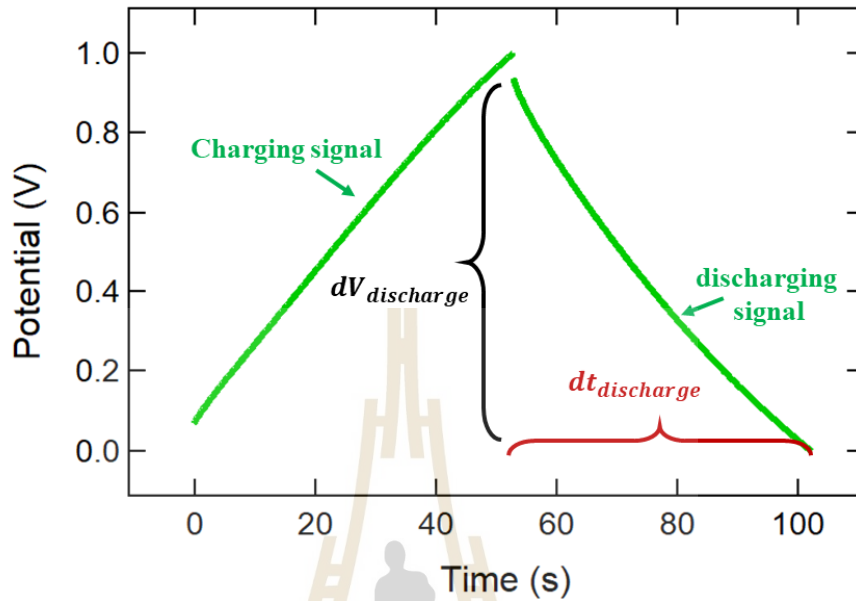


**Figure 3.7** Example of GCD profile.

The single-cell (symmetric) supercapacitor can be considered as two parallel-plate capacitors in series. The total capacitance ( $C_T$ ) of the cell can be calculated as:

$$\frac{1}{C_T} = \frac{1}{C_a} + \frac{1}{C_c} \quad (3.1)$$

where  $C_a$  is the capacitance of anode and  $C_c$  is the capacitance of cathode. For a symmetric supercapacitor, both electrodes are made of the same active material. The specific capacitance of the active materials ( $C_{sp, materials}$ ) is usually used to determine ability of each material. The capacitance of cell ( $C_{cell}$ ) can be written as:

$$\frac{1}{C_{cell}} = \frac{1}{m_a C_{sp, materials}} + \frac{1}{m_c C_{sp, materials}} \quad (3.2)$$

Therefore,

$$C_{cell} = \frac{1}{2} m C_{sp,materials} \quad (3.3)$$

The specific capacitance of cell ( $C_{sp, cell}$ ) can be expressed as:

$$C_{sp,cell} = \frac{C_{cell}}{2m} = \frac{\frac{1}{2} m C_{sp,materials}}{2m} = \frac{C_{sp,materials}}{4} \quad (3.4)$$

where  $m_a$  and  $m_c$  are the mass of active materials in anode and cathode electrodes (g), respectively.

The specific capacitance for materials of a single electrode ( $C_{sp, materials}$ ) is four time of the specific capacitance of supercapacitor cell which can be estimated from GCD and CV measurements. Energy density and power density are usually used to evaluate the electrochemical performances of supercapacitor. The energy and power density of a supercapacitor coin cell can be calculated as:

$$Energy\ density = \frac{1}{8} \left( \frac{1000}{3600} \right) (C_{sp,materials} V^2) \quad (3.5)$$

$$Power\ density = \frac{E(3600)}{\Delta t_{discharge}} \quad (3.6)$$

where  $V$  is the operating voltage in volt (V), and  $\Delta t_{discharge}$  is the discharge time in second (s). In the GCD technique, the capacitance of a supercapacitor can be estimated as follows:

$$C = \frac{I dt_{discharge}}{dV_{discharge}} \quad (3.7)$$

Since  $I$  is constant current which is measured on 2 electrodes of coin cell,  $C_{sp,materials}$  ( $F\ g^{-1}$ ) is therefore calculated by using the following equation:

$$C_{sp,materials} = 4 \frac{I}{\frac{dV_{discharge}}{dt_{discharge}}} \quad (3.8)$$

Cyclic stability, sometimes called capacitance retention, is also an important consideration when evaluating the performance of supercapacitors (EDLCs or redox capacitors). Galvanostatic charge/discharge cycling is the most common method used for determining the cycling stability. This can be done by repeating GCD test over large number of cycles (normally, 1000-10,000 cycles).

In this research, the potentiostat model Metrohm, Eco Chemie Autolab PGSTAT30, operated with NOVA 1.11 software, was used for GCD measurement. The measurements were performed with applied constant currents of 0.125, 0.25, 0.5, 1, 2, 5, 10 A g<sup>-1</sup>. For the cyclic stability evaluation, the measurement was done at a constant current of 1 A g<sup>-1</sup>.

### 3.5.2 Cyclic voltammetry (CV) measurement

Cyclic voltammetry (CV) is a powerful tool in the field of electrochemistry. It has been extensively used to determine the performance of electrical energy storing devices, such as, supercapacitors. In this technique, electric potential is imposed at the electrodes which varies periodically and linearly with time. The resulting electric current is recorded as CV loop as shown in Figure 3.9. Normally, CV loop shows rectangular shape that implies EDLC behavior. The CV loop may also exhibit a quasi-rectangular shape with a pair of small board oxidation or pseudocapacitance peak as shown in Figure 3.9, which suggests both EDLC and pseudocapacitive behavior. The total charge accumulated at the surface of electrode can be calculated by integrating the electric current with respect to time. The capacitance can be then estimated as the total charge

divided by the potential window. Capacitance is generally measured at different scan rates.

The specific capacitance ( $\text{F g}^{-1}$ ) of a supercapacitor coin cell can be calculated as shown in following:

$$C = \frac{Q}{V} = C = \frac{Q}{V} \quad C = \frac{Q}{V} \text{Idt/dv} = I/v \quad (3.12)$$

where  $v = dV/dt$  is the potential scan rate ( $\text{V s}^{-1}$ ).

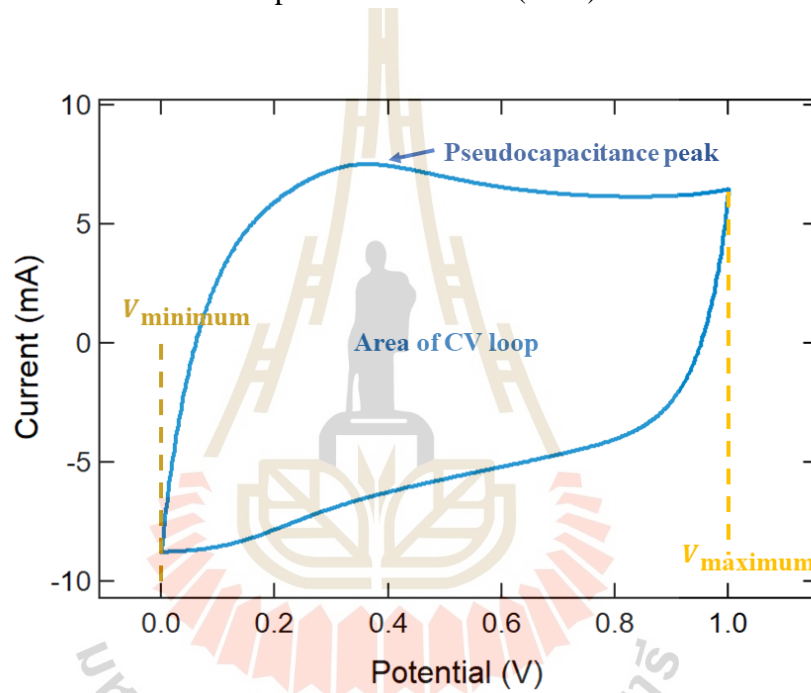


**Figure 3.8** Example for CV measurement.

$I$  is the the current (A) which is a function of voltage,  $I(V)$ , as:

$$I = I(V) = \frac{\int_{V_{\text{minimum}}}^{V_{\text{maximum}}} I(v) dv}{\text{Potential window of CV}} = \frac{\text{Area of CV loop}}{V_{\text{maximum}} - V_{\text{minimum}}} \quad (3.14)$$

Therefore,

$$C = \frac{I}{v} = \frac{\int_{V_{\text{minimum}}}^{V_{\text{maximum}}} I(V) dv}{\frac{V_{\text{maximum}} - V_{\text{minimum}}}{v}} \quad (3.15)$$

Since the CV loop contains both charge and discharge steps, the specific capacitance of only discharge state therefore can be calculated as:

$$C_{\text{cell}} = \frac{\int_{V_{\text{minimum}}}^{V_{\text{maximum}}} I(v) dv}{2v (V_{\text{maximum}} - V_{\text{minimum}})} \quad (3.17)$$

Then,  $C_{\text{sp,cell}}$  is calculated as:

$$C_{\text{sp,cell}} = \frac{\int_{V_{\text{minimum}}}^{V_{\text{maximum}}} I(V) dv}{2v (V_{\text{maximum}} - V_{\text{minimum}})} \left(\frac{1}{m}\right) \quad (3.18)$$

where  $m$  is mass of active materials for two electrodes of a coin cell, Then,  $C_{\text{sp,materials}}$  ( $\text{F g}^{-1}$ ) is evaluated as:

$$C_{\text{sp,cell}} = 4 \frac{\int_{V_{\text{minimum}}}^{V_{\text{maximum}}} I(V) dv}{2v (V_{\text{maximum}} - V_{\text{minimum}})} \left(\frac{1}{m}\right) = 2 \frac{\int_{V_{\text{minimum}}}^{V_{\text{maximum}}} I(V) dv}{vm (V_{\text{maximum}} - V_{\text{minimum}})} \quad (3.19)$$

where  $V$  is potential in volt (V),  $V_{\text{max}}-V_{\text{min}}$  is potential window in volt (V), and  $m$  is mass of active materials in gram (g), and the integration of the resulting cyclic voltammograms (Stoller et al., 2008) (J. H. Park, Park, Shin, Jin, and Kim, 2002) (Qu et al., 2009) (Stoller and Ruoff, 2010) (W. Chen, Fan, Gu, Bao, and Wang, 2010).

In this thesis, the potentiostat model Metrohm, Eco Chemie Autolab PGSTAT30, operated with NOVA 1.11 software was used for the CV measurements. The specific capacitance was evaluated with potential scan rates of 5, 10, 25, 50, 100, 200, 500  $\text{mV s}^{-1}$ .

### 3.5.3 Electrochemical impedance spectroscopy (EIS)

Electrochemical impedance spectroscopy is an electrochemical technique that is used to investigate the electrochemical behavior at the electrode/electrolyte interface. An example of Nyquist plot, which is the plot of the real and negative of imaginary part of the impedance obtained from the EIS measurement is shown in Figure 3.9. Based on Bing-Ang Mei's work (Mei, Munteshari, Lau, Dunn, and Pilon, 2018), we use the interpretations from this research to be guidelines as shown in following.

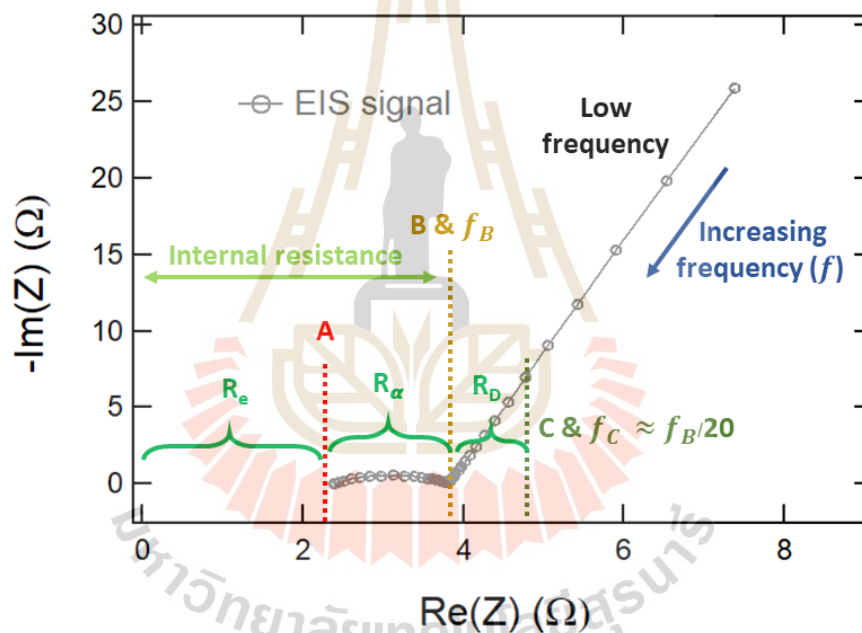


**Figure 3.9** Example of Nyquist plot obtained from electrochemical impedance spectroscopy (EIS) measurement.

The plot can be divided into 3 parts for physical interpretation of for EDLCs. Electrode resistance ( $R_e$ ), resistance at point A, is related with electrical conductivity of electrode and contact resistance between collector and electrode. Electrolyte resistance ( $R_e$ ), diameter of the semicircle,  $R_\alpha$ , is related with electrolyte concentration and bulk

electrolyte resistance. Therefore,  $R_e + R_{\Omega}$  can be interpreted as the electrode-electrolyte resistance. Diffuse layer resistance ( $R_D$ ) is the resistance of diffusion layer near one electrode. The slope of plot in this region is associated with limitation of electrolyte ions diffusion (Taberna, Portet, and Simon, 2006) (Sing, 1985) and conductivity at the interface between electrode–electrolyte (D. Zhu et al., 2017).

The electrochemical impedance spectroscopy is a sensitive technique. Great care must be taken. It is not always well understood because of the incomplete mathematical developments of equations connecting the impedance data with the physico-chemical parameters.

In this research, the potentiostat model Metrohm, Eco Chemie Autolab PGSTAT30, operated with NOVA 1.11 software was used for the EIS measurement. The EIS was operated in the frequencies range between  $10^{-1}$  Hz and  $10^4$  Hz at a bias potential of 500 mV.

#### **3.5.4 Leakage current or self-discharge measurement**

The leakage current or self-discharge is an important parameter which implies the ability to maintain the state of charges when supercapacitors are not connected to an electrical network. It is always the main weak point for supercapacitor.

There are many methods that can be used for measuring the leakage current, for example, applying DC voltage to a supercapacitor and measuring the required current for maintaining voltage, and charging a supercapacitor to fixed voltage, then opening the circuit and measuring the voltage change during self-discharge process which is used in this thesis. Figure 3.10 shows an example of a leak current measurement which is a plot between remained voltage and passing time.

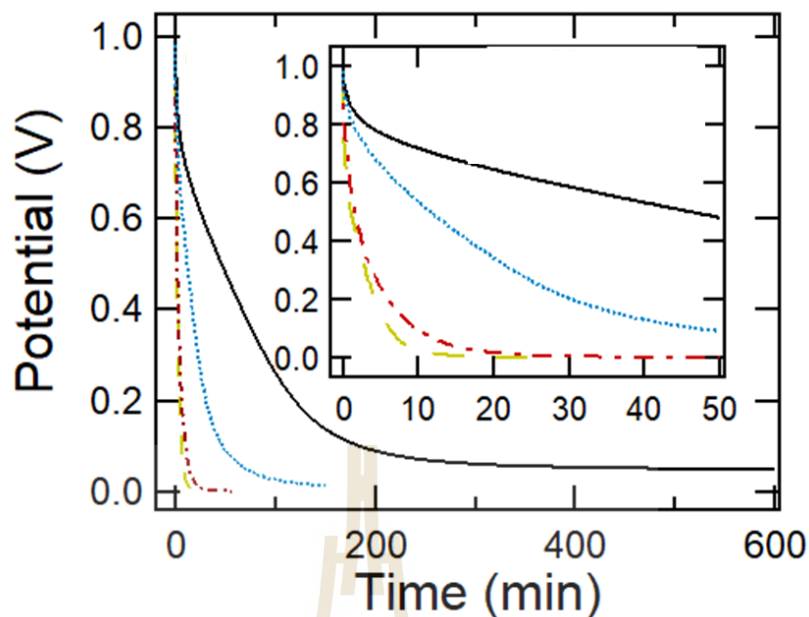


**Figure 3.10** Example of leak current or self-discharge measurement.

### 3.6 Material characterization techniques

#### 3.6.1 X-ray diffraction (XRD)

X-ray diffraction is a common material characterization technique that provides detailed information about the crystallographic structure, chemical composition, and physical properties of materials. It also allows for identification of crystal orientations and interatomic spacing ( $d_{(hkl)}$ ). Subsequently, XRD results were showed relationship between intensity of diffraction plane peak and  $2\theta$  which come from incident X-ray direction. In plane X-ray waves, are used for this technique because wavelength is on the same length scale as interatomic spacing and lattice parameter values. X-ray diffraction data is analyzed by using Bragg's equation 3.17 as shown in following.

For explanation of XRD equations, there are incidents' X-ray wave in the same plane that incident to atomic structure plane ( $s_1, s_2$  etc.). Then, based on natural of EM

wave, interval between  $ab+bc = n\lambda$  including  $de+ef = m\lambda$  where  $n$  and  $m$  are counting number. Figure 3.11 showed this relationship for plan and adjacent plan. Moreover, useful trigonometry theory, we can show  $\sin\theta = ab/d_{(hkl)}$ , and  $\sin\theta = bc/d_{(hkl)}$ . For above, we will get this equation as shown in Equation 3.17.

$$n\lambda = 2d_{(hkl)}\sin\theta \quad (3.17)$$

and the angle of reflection for a particular set of lattice planes  $(hkl)$  is given as

$$2\theta = 2\sin^{-1}\left(\frac{n\lambda}{2d_{(hkl)}}\right) \quad (3.18)$$

where  $n$  is the order of reflection,  $\lambda$  is the wavelength of x-rays,  $d_{(hkl)}$  is the characteristic spacing between the crystal planes of a given specimen, and  $\theta$  is the angle between the incident beam and the normal to the reflecting lattice plane.

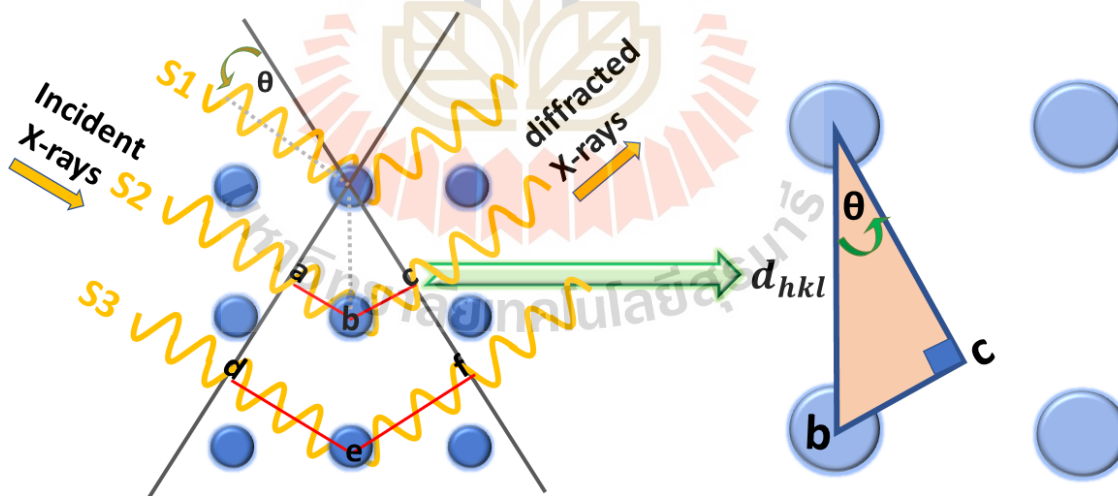
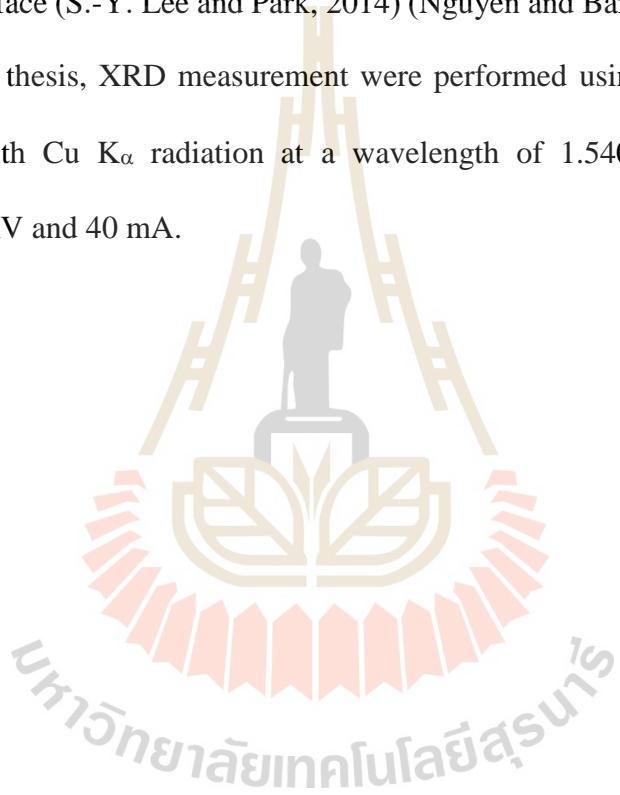


**Figure 3.11** Schematic representation of Bragg's Law for XRD.

To interpret XRD data, according to materials that were used in this thesis, based on graphene oxide, PVDF, and carbon black. Subsequently, possible diffraction plane and their  $2\theta$  were showed in Table 3.1. Furthermore, this thesis concentrates useful XRD results to attribute and support graphene oxide exfoliation. Due to  $2\theta$  and  $d_{(hkl)}$  are reciprocal in equation 3.2. Therefore, in case of, XRD peaks show shifting of  $2\theta$  to lower value that can be attributed interatomic spacing for each atomic plane  $d_{(hkl)}$  will increase or exfoliated surface (S.-Y. Lee and Park, 2014) (Nguyen and Baird, 2007).

In the thesis, XRD measurement were performed using XRD; BRUKER, D8 ADVANCE) with Cu  $K\alpha$  radiation at a wavelength of 1.5406 Å from a generator operating at 40 kV and 40 mA.



**Tabel 3.1** Possible diffraction plane and their located  $2\theta$  for XRD.

Determine of diffraction plane	$2\theta$ (°)	Ref.
Signature of GO with interlayer d-spacing $\sim 6.91$ - $8.22$ Å	10.76-12.80	(Slabaugh and Seiler, 1962) (Nakajima, Mabuchi, and Hagiwara, 1988) (Strong et al., 2012) (Shayeh, Ehsani, Ganjali, Norouzi, and Jaleh, 2015)
$\alpha(100)$ from PVDF	17	(W.-b. Zhang et al., 2015)
$\alpha(020)$ from PVDF and GO and rGO	18.4	(W.-b. Zhang et al., 2015) (Xu, Liu, Neoh, Kang, and Fu, 2011)
$\alpha(110)$ from PVDF	20	(W.-b. Zhang et al., 2015)
$\alpha(021)$ from PVDF and rGO	26.7	(W.-b. Zhang et al., 2015) (L. Q. Xu et al., 2011)
(002) from rGO	27-28	(Saleem, Haneef, and Abbasi, 2018) (Strankowski, Włodarczyk, Piszczyk, and Strankowska, 2016) (L. Q. Xu et al., 2011)
Signal from rGO	38.5	(L. Q. Xu et al., 2011)
(10), (100)	43.5	(Stobinski et al., 2014)
Signal from rGO	44.4	(L. Q. Xu et al., 2011)
(004) or (103) from graphite	50.5	(Stobinski et al., 2014) (Pang et al., 2010)
(004) from graphite	55	(Ban, Majid, Huang, and Lim, 2012)
(110) from graphite	60	(Ban et al., 2012)
Signal from graphene oxide and (220) from graphite	74.5	(Singh et al., 2009) (Pang et al., 2010)
(110) from carbon black	78	(Ungar, Gubicza, Ribarik, Pantea, and Zerda, 2002)

### 3.6.2 Scanning electron microscopy (SEM)

Scanning electron microscopy (SEM) produces images of surface sample by scanning the surface with a focused beam of electrons as shown in Figure 3.13. The principle of SEM is based on the interaction between an incident electron and the solid specimen. This interaction can produce signals that contain information about the surface topography and elemental composition of the sample. SEM images are produced by collecting two types of electrons which are backscattered electrons (BSE) and secondary electrons (SE). The secondary electrons are originated from atoms on sample surface that interact as inelastic collision with the electron beam. On the other hand, the backscattered electrons are the primary electrons which are reflected after elastic interactions between the electron beam and atoms. They are originated from deeper regions of sample surface. The BSE and SE carry different types of information. BSE image is highly sensitive to differences in atomic number such that the higher the atomic number and the brighter the material appears in the image, while SE image can provide more detailed surface information.

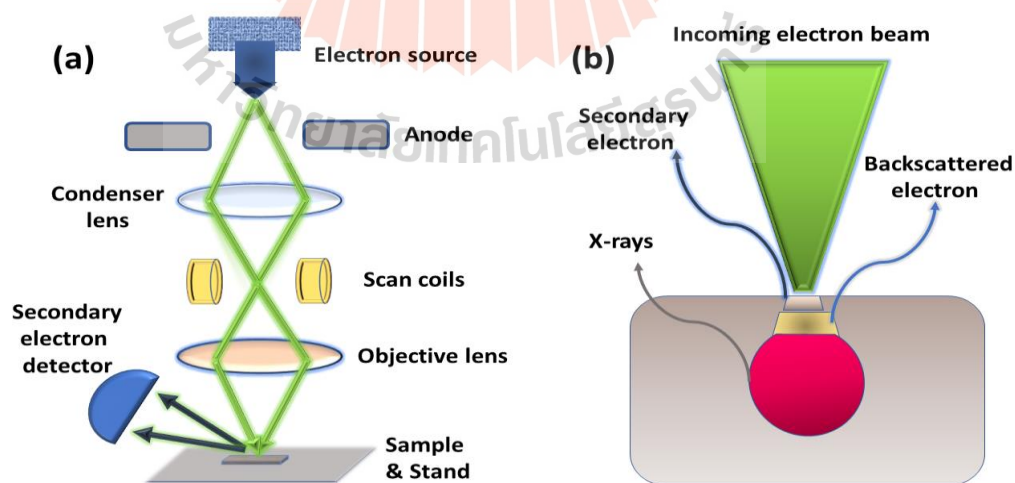


**Figure 3.12** Schematic diagram of (a) basic SEM components and (b) different types of SEM signals.

In this thesis, SEM image were provided using SEM machine from Hitachi, SU8230.

### 3.6.3 Raman spectroscopy

Raman spectroscopy is a spectroscopic and non-destructive chemical analysis technique that can be used to determine vibrational, rotation, structural information, and other low-frequency modes of molecules. This technique relies upon inelastic scattering of photons, known as Raman scattering, including both Stokes Raman scattering and anti-Stokes Raman scattering, as shown in Figure 3.13(a).

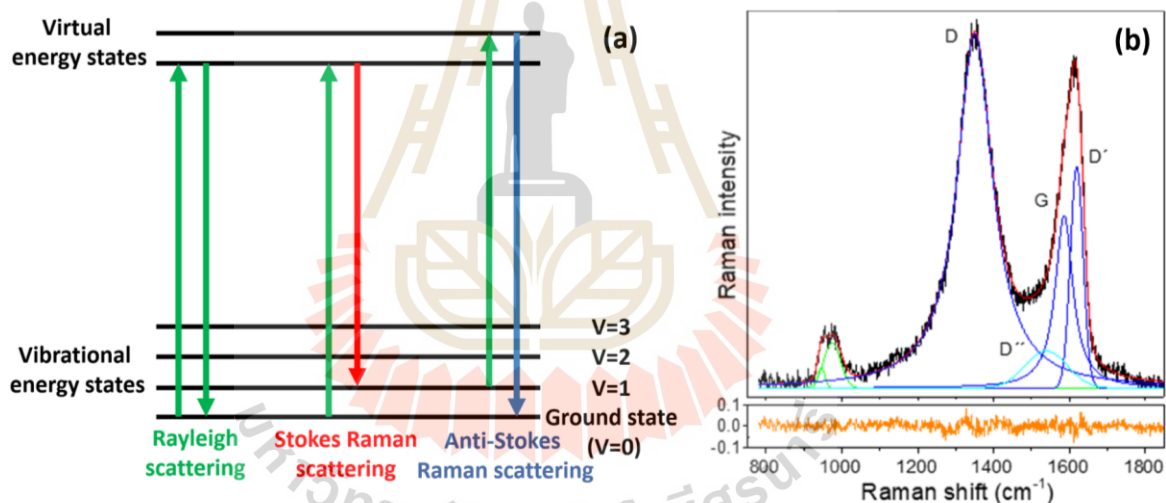


**Figure 3.13** Schematic diagram of the identification of Raman scattering signal (a), example of deconvoluted Raman spectra (b) (Berrellez-Reyes and Alvarez-Garcia, 2019).

In this technique, a monochromatic light, usually laser in the visible region, such as, green laser which has a wavelength of 532 nm, is focused on sample surface, and interacts with its vibrations or excitations at a molecular level. This generates shifted

laser photons which are immediately recorded as Raman scattering spectrum and then reported as a relationship between wavenumber and intensity.

Raman spectroscopy is a useful and famous technique to investigate graphene, GO and rGO properties. A typical Raman spectrum excited with green laser usually shows 2 obvious band peaks located at the wavenumbers of  $\sim 1345$  and  $\sim 1590$   $\text{cm}^{-1}$  corresponding to defect graphite structure (D-band), graphitic carbon phase with C=C double bond with  $\text{sp}^2$ -hybridization (G-band), respectively. These main peaks can be deconvoluted into more additional band peaks at the wavenumbers of  $1520$  and  $1618$   $\text{cm}^{-1}$  which are attributed to interstitial defects or amorphous  $\text{sp}^2$ -bonded carbons ( $\text{D}''$ -band) and disorder-induced phonon mode due to crystal defects ( $\text{D}'$ -band), respectively as shown in Figure 13(b) (Tuinstra and Koenig, 1970) (X. Zhao and Ando, 1998) (Ferrari and Robertson, 2000).

In this thesis, the Raman spectroscopy was carried out on a Raman; Horiba, KH8700 with green laser which has a wavelength of  $532$  nm. The Raman spectra were deconvoluted based on Lorentzian functions for D- and G- bands and Gaussian function for  $\text{D}'$ - and  $\text{D}''$ - bands (Berrellez-Reyes and Alvarez-Garcia, 2019). The area of these band peaks and the  $I_{\text{D}}/I_{\text{G}}$  were calculated. This value can indicate the C=C double bond with  $\text{sp}^2$  hybridization content and amount of oxygen/nitrogen-containing functional groups on electrode surface. The decrease of  $I_{\text{D}}/I_{\text{G}}$  suggests the decrease of disorder state and increase of crystalline graphene (Childres, Jauregui, Park, Cao, and Chen, 2013). This is (Claramunt et al., 2015). Moreover, the red-shifting of G-band peak can also be used to suggest the transition from an amorphous to a more crystalline carbon state of graphene (Strong et al., 2012). This is attributed to the strain on graphene structure (Ni et al., 2008).

### 3.6.4 Fourier transform infrared (FT-IR) spectroscopy

Fourier Transform Infrared (FT-IR) spectrometry is a technique which is used to obtain infrared spectrum of absorption, emission, and photoconductivity of solid, liquid, and gas. It is used to detect different functional groups in used materials.

To explain about operated detail for FT-IR technique, interferometer is a simple optical device that can produce many infrared frequencies from a light source by employing beam splitter as shown in Figure 3.14. This Figure showed one beam reflects off a mirror that is fixed in place. another beam reflects off a mirror which can move with short distance (few millimeters). Subsequently, these two beams (incident beam and reflected beam) are recombined again before exposure on sample. Therefore, the recombined wave exhibited many wavenumbers, depend on, moving step of moving mirror.

The resulted spectrum of this technique represents the molecular transmission and absorption of sample with many frequencies wave from interferometer. Then, these results exhibit a molecular fingerprint of each bonding on sample which is no two unique molecular structure, can produce the same resulted spectrum.

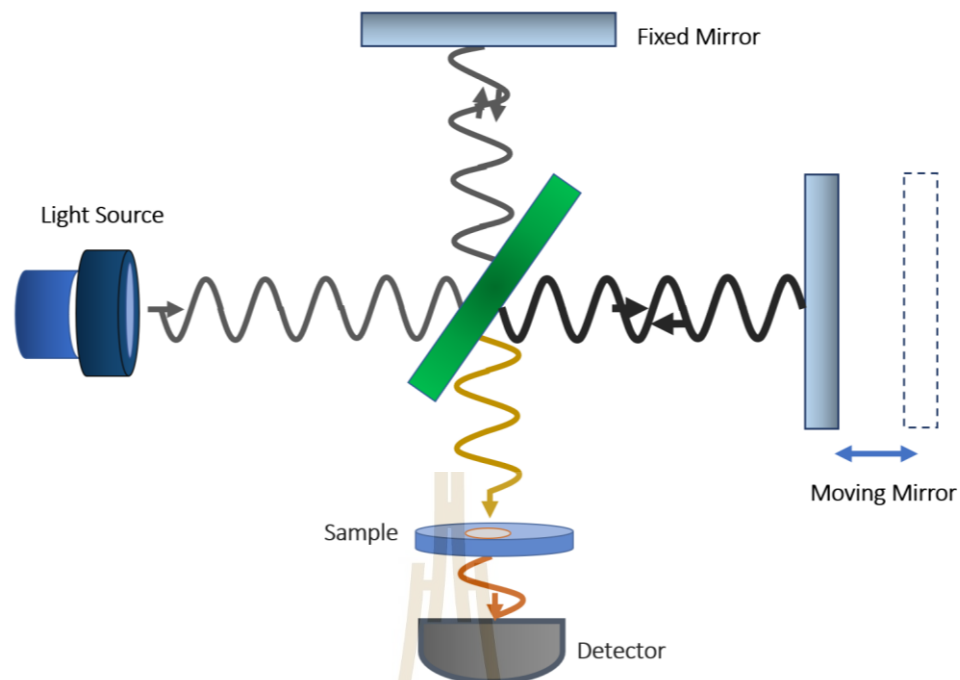


**Figure 3.14** Simple schematic of FT-IR spectrometer.

According to this spectroscopy shows relationship of intensity of infrared after responding with all bonding of electrode sample then transmit to detector and wavenumber of infrared wave. To interpreting data, each bonding in materials can absorb or match with individual frequency of infrared, called fingerprint of each bonding which are used to identify their bonding types. According to there are many materials were used in this research. Then, all possible absorption peak which may appear, and wavenumber was shown in following Table 3.2.

**Table 3.2** Possible bonding and their located wavenumber for FT-IR.

Possible absorption peak	Wavenumber (cm <sup>-1</sup> )	Reference
the stretching vibration peaks of water molecule	3,423	(Stankovich, Piner, Nguyen, and Ruoff, 2006)
the O–H stretching vibration	3,410	(J. Park and Kim, 2014)
symmetric and anti-symmetric stretching vibrations of –CH <sub>2</sub>	2,954	(J. Park and Kim, 2014)
	2,831	(J. Park and Kim, 2014)
C=O (carbonyl)	1,733	(Stankovich et al., 2006)
	1,713	(Ma et al., 2012)
	1,703	(Y. Hu et al., 2010)
Thiocarboxylic acid ester R-CO-SR	1,698	(Stankovich et al., 2006)
C=C (Aromatic skeleton carbon ring)	1,631	(W. S. V. Lee, Leng, Li, Huang, and Xue, 2015)
The bending vibration of N-H	1,585	(Ma et al., 2012)
	1,585	(Y. Hu et al., 2010)
CHN	1,543	(Ai et al., 2012)
-C-F- group	1,400	(Ryu and Shanmugaraj, 2014) (Han et al., 2013)
O-C=O (Carboxyl)	1,396	(Stankovich et al., 2006)
the stretching vibration of >C–H, which could be assigned to H-adsorbed on graphene surface.	831	(Acharya, Gopinath, Alegaonkar, and Datar, 2018)
The stretching vibration of N-H	820	(Ma et al., 2012)
The asymmetric stretching of metal-O	600-400	(Y. Hu et al., 2010)
		(J. Park and Kim, 2014)

Here, FTIR spectrum is recorded between 4000 and 500 cm<sup>-1</sup> with FT-IR: Perkin Elmer model Spectrum GX with powder sample.

### 3.6.5 X-ray photoelectron spectroscopy (XPS)

X-ray photoelectron spectroscopy (XPS) is a surface-sensitively spectroscopic technique based on the photoelectric effect. XPS spectra are obtained by irradiating a material with a monoenergetic X-ray beam while simultaneously measuring the kinetic energy and number of emitted electrons that escape from surface as shown in Figure 3.16. The kinetic energy of the emitted electrons ( $E_k$ ) is related to the energy of the incident X-ray ( $h\nu$ ) as in the following equation:

$$E_k = h\nu - W - E_b \quad (3.19)$$

where,  $W$  is the surface work function (eV),  $h$  is the Plank's constant,  $\nu$  is the frequency of incident X-ray and  $E_b$  is the binding energy.

The binding energies of electrons for element have their own fingerprint. Only certain values of energy can excite each electron in different quantized energy. This technique therefore can provide the information of elemental composition as well as electronic structure of material via the relationship plotted between binding energy or kinetic energy of incident electron with intensity of emitted electrode.

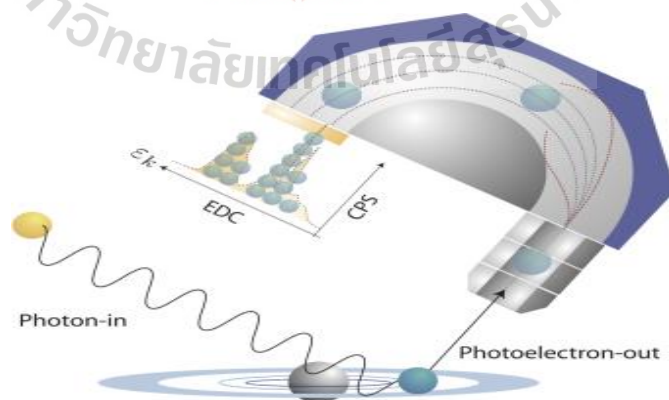


**Figure 3.15** Schematic representation of X-ray photoelectron spectroscopy (XPS) technique (picture from <https://www.slri.or.th/th/beamline/bl32a-pes.html>).

In this research, the XPS experiments were performed by using XPS machine stand alone; ULVAC-PHI PHI5000 Versa Probe II at beamline 5.3 (SLRI) and XPS at beamline 3.2a (SLRI).

### 3.6.6 Contact angle and wettability measurement

Contact angle ( $\theta$ ) is a parameter which relates with electrochemical performance of supercapacitors applications. Contact angle is indicated by using wetting behavior of the degree of wetting when electrode surface and electrolyte interacts as shown in Figure 3.17.

In this thesis, the contact angle was measured by dropping an electrolyte on electrode surface and taking pictures. The contact angle was then derived from the picture using ImageJ program. Large contact angles higher than  $90^\circ$  correspond to low wettability, while small contact angles lower than  $90^\circ$  correspond to high wettability (Y. Yuan and Lee, 2013). There are 2 main parameters, effect on contact angle of electrode materials which are heteroatom doping, cause polarity surface (Y. Li et al., 2015) (Dai et al., 2019) and more surface roughness, can increase wettability (Nakae, Inui, Hirata, and Saito, 1998).

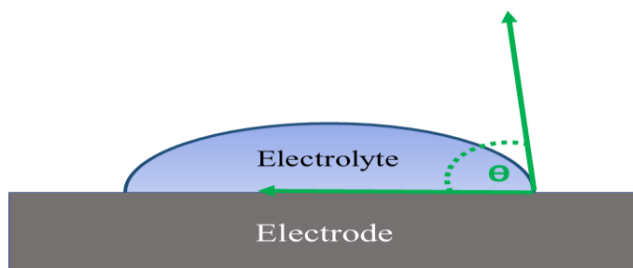


**Figure 3.16** Schematic of a sessile-drop contact angle with electrode surface and electrolyte system.

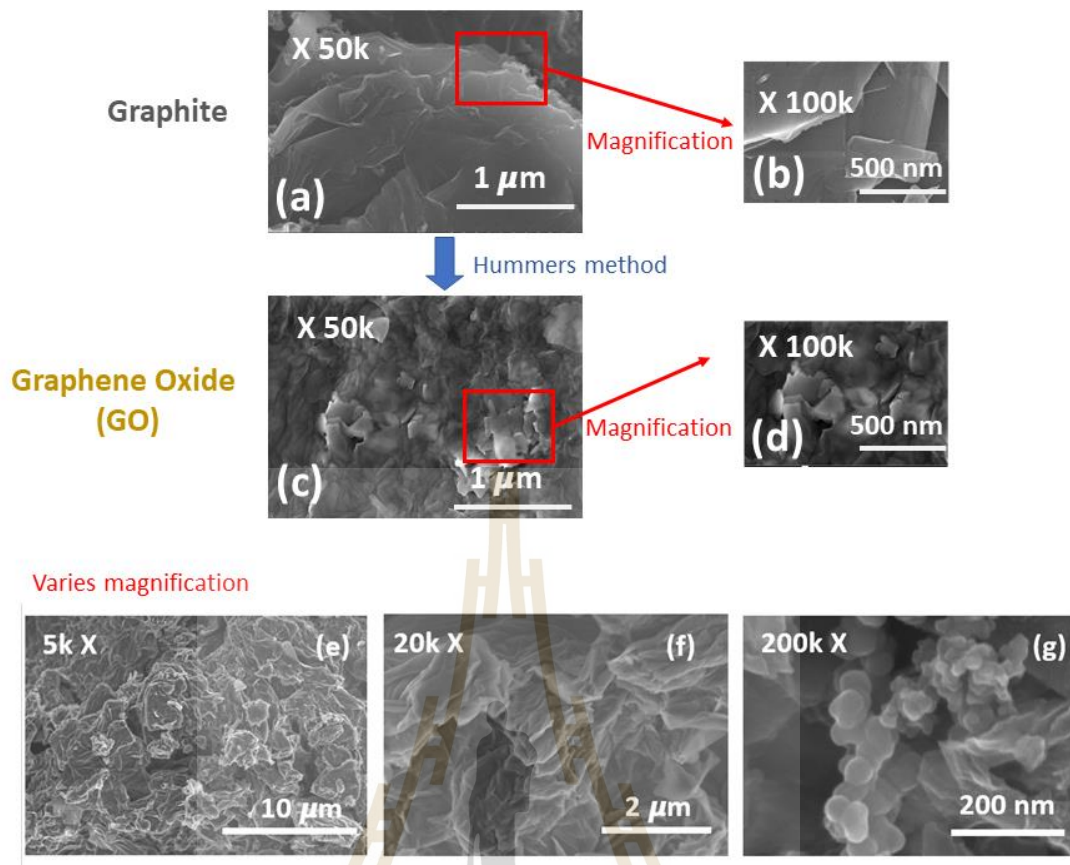
## CHAPTER IV

### RESULTS AND DISCUSSION

#### 4.1 Synthesis and characterization of Graphene oxide (GO)

In this work, graphene oxide (GO) was used as a based materials for fabrication of supercapacitor electrode. It was synthesized from graphite via the modified Hummer's method. The properties of the synthesized GO were investigated by many characterization techniques including scanning electron microscopy ( SEM) , X-ray diffraction ( XRD) , Fourier Transform Infrared ( FT-IR) and X-ray photoelectron spectroscopy (XPS).

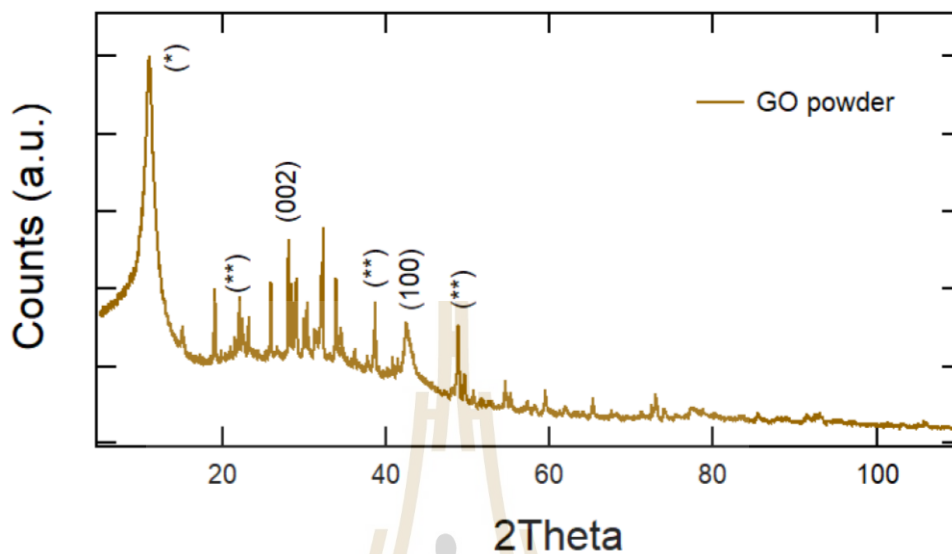
SEM images of graphite and the prepared GO are shown shown in Figure 4.1. The SEM image reveal the layered structure of graphite which consists of square shape and smoot surface flake sheets. This is similar to the previous observation by Markervich et.al. (Markervich, Salitra, Levi, and Aurbach, 2005).After the transformation to GO, the smooth graphit sheets became wrinsurface mophology of GO transform towrinkled and randomly aggregated sheets which is the characteristics of GO (Śliwak, Grzyb, Díez, and Gryglewicz, 2017) (Soltani and Lee, 2017) (Lin, Waller, Liu, Liu, and Wong, 2013).



**Figure 4.1** SEM images of graphite (a), (b) and the prepared GO (c), (d) and SEM images of graphene oxide (GO) with varies magnifications (e)- (g).

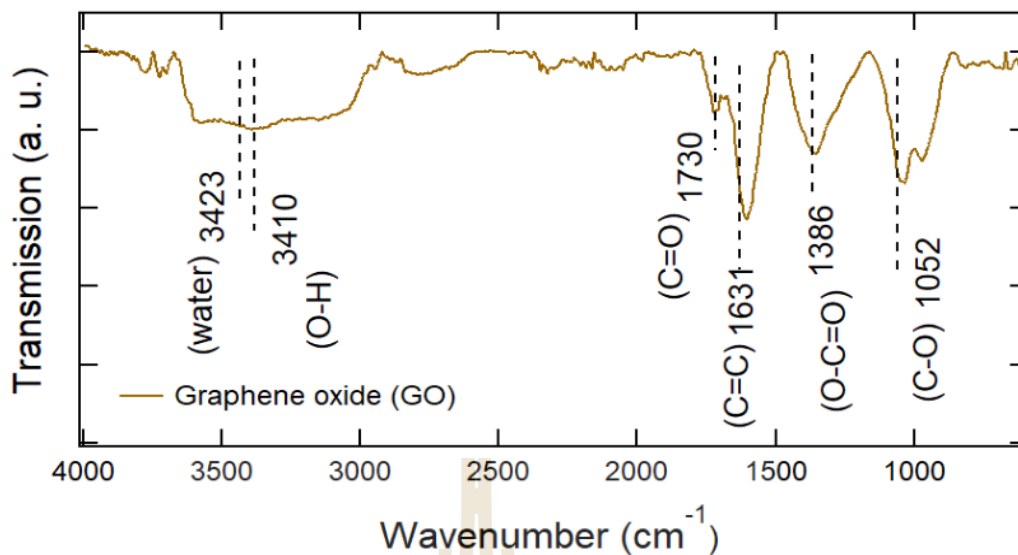
X-ray diffraction (XRD) pattern of the prepared GO is shown in Figure 4.2. There are an obvious single peak at  $2\theta = 10.76 - 12.80^\circ$  corresponds to oxidation with permanganate reveals an interlayer d-spacing in range of 6.91 - 8.22 Å (GO membrane nanolayer) which was marked peak with \* (Slabaugh and Seiler, 1962) (Nakajima et al., 1988) (Strong et al., 2012), peaks around 26-28°, indicated (002) plane peak showed similar with other research (W.-b. Zhang et al., 2015) (Strankowski et al., 2016), peak at 44°, indicated (100) or (10) plane peak showed similar with Xu Li research work (L. Q. Xu et al., 2011) and another mark peaks which showed matching of GO from other

research (W.-b. Zhang et al., 2015) (L. Q. Xu et al., 2011). Unfortunately, there are other peaks appear in XRD results which came from impurity on our GO powder.



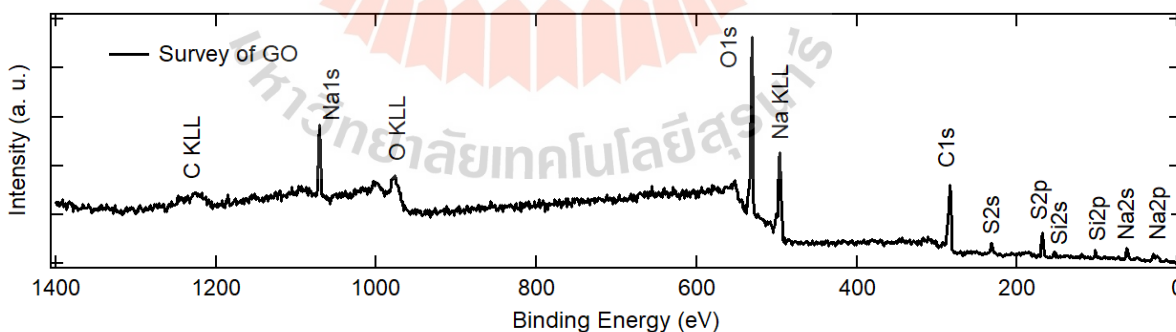
**Figure 4.2** XRD pattern of the prepared GO.

Figure 4.3 shows the FT-IR spectrum of the prepared GO. The peaks located at wavenumber of 1052, 1386, 1631, 1730, 3410, and 3423  $\text{cm}^{-1}$  are attributed to C-O, O-C=O, C=C, C=O, O-H and water, respectively. The observation of many oxygen functional groups reflects the nature of GO structure. This observation is in good agreement with the previous studies (Biniak, Szymański, Siedlewski, and Świątkowski, 1997) (K. H. An et al., 2002) (Lorenc-Grabowska, Gryglewicz, and Diez, 2013).



**Figure 4.3** FT-IR spectrum of the synthesized GO.

The chemical composition of the prepared GO was also investigated by XPS. Figure 4.4 shows a wide scan XPS spectra of the prepared GO in the range of 0-1,400 eV. The spectrum reveals the presences of C O which are the main elements of GO. The presence of sodium and silicon may be due to the residue from the synthetic process.



**Figure 4.4** Wide scan XPS spectrum of the synthesized GO.

The high resolution XPS spectra in the C1s and O1s region of the prepared GO are shown in Figure 4.5. The C1s was deconvoluted into 5 components at the binding energies of  $\sim 284.5$ ,  $\sim 258.3$ ,  $\sim 286.5$ ,  $\sim 287.5$ ,  $\sim 289.0$  eV, corresponding to C=C ( $sp^2$ ),

C-C ( $sp^3$ ), C-O, C=O and COOH, respectively (Biniak et al., 1997) (K. H. An et al., 2002) (Kelemen and Kwiatek, 1995) (Zhuo, Zhang, Du, and Yan, 2015). The high resolution signal of O1s was deconvoluted into 4 peaks at the binding energies of  $\sim 531.0$ ,  $\sim 532.5$ ,  $\sim 534.4$  and  $\sim 536.0$  eV, corresponding to C=O, C-OH, C-O-C and water, respectively (Lorenc-Grabowska et al., 2013) (Zielke, Hüttinger, and Hoffman, 1996). The relative atomic percentage of each bonding in C1s and O1s are also shown in Figure 4.5. It was observed that C=C ( $sp^2$ ) bonding is the main component of the prepared GO, which is consistent with the most popular model proposed by Lerf's research (Lerf et al., 1998). The estimated atomic ratio between C and O was found to be approximate 1.1, which is similar to that reported in the other studies (Compton and Nguyen, 2010).

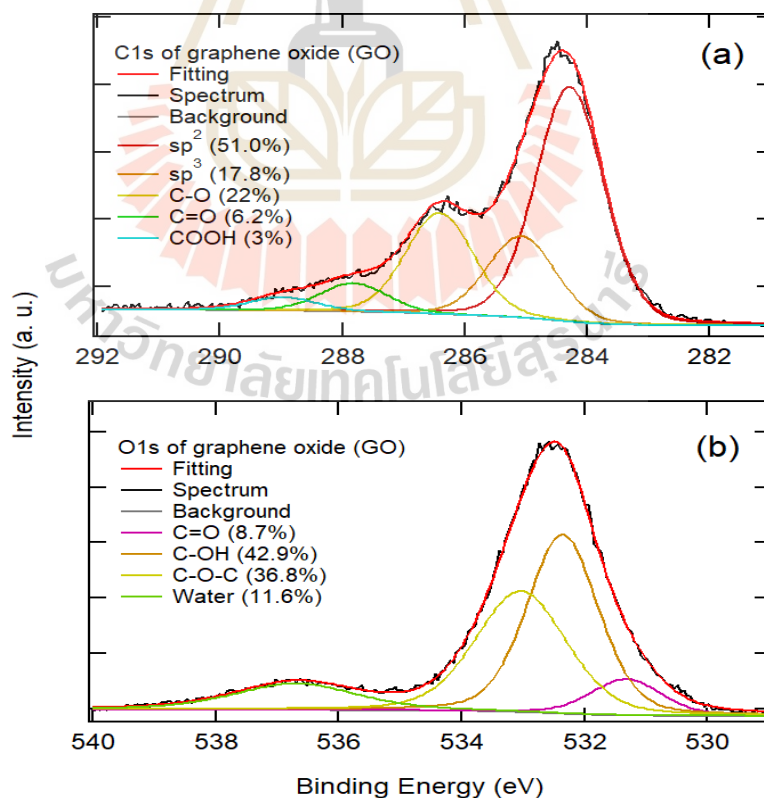


**Figure 4.5** High resolution XPS spectra of C1s and O1s peak of GO.

The structure of the prepared GO was also investigated by Raman spectroscopy. Figure 4.6 shows the Raman spectrum of the prepared GO recorded with green light laser with a wavelength of 532 nm. The spectrum was deconvoluted into 4 peaks at the wavenumbers of 1348.6, 1519.7, 1586.1 and 1620  $\text{cm}^{-1}$  corresponding to defect graphite structure (D-band), interstitial defects or amorphous  $\text{sp}^2$ -bonded carbons ( $\text{D}''$ -band), graphitic carbon phase with C=C double bond with  $\text{sp}^2$ -hybridization (G-band) and disorder-induced phonon mode due to crystal defects ( $\text{D}'$ -band), respectively (Tuinstra and Koenig, 1970) (X. Zhao and Ando, 1998) (Ferrari and Robertson, 2000). The estimated  $I_{\text{D}}/I_{\text{G}}$  and  $I_{\text{D}''}/I_{\text{G}}$  ratios are  $\sim 2.1$  and  $\sim 0.5$ , respectively, as listed in Table 4.1. This result suggests that the prepared GO consists of graphitic carbon phase mixing with disorder state such interstitial defects, and amorphous  $\text{sp}^2$ -bonded carbons.

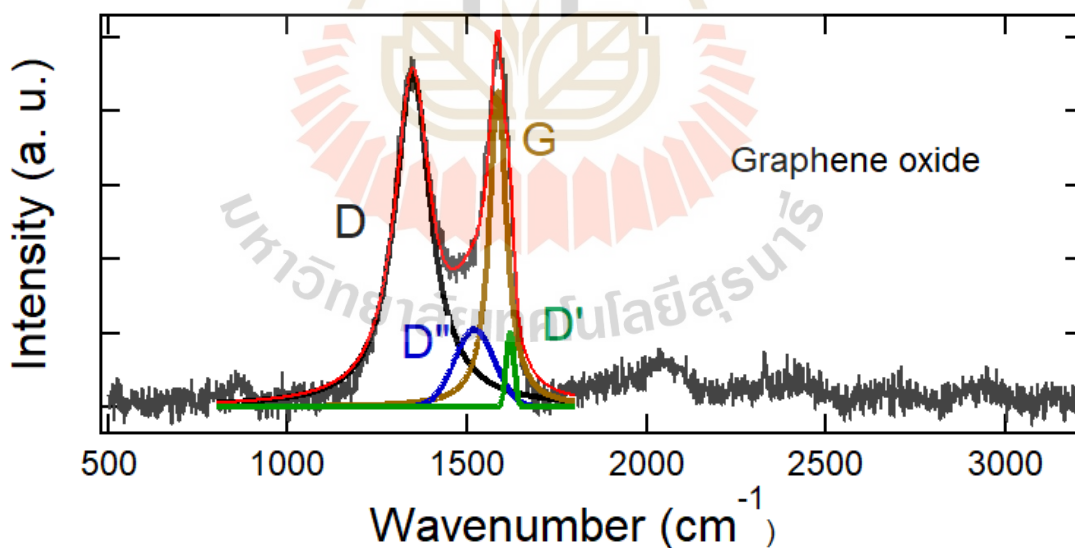


**Figure 4.6** Raman spectroscopy result of graphene oxide (GO).

**Table 4.1** The fitted and analyzed data of Raman spectrum of the prepared GO.

	$I_D/I_G$	$I_{D'}/I_G$	Peak position (cm <sup>-1</sup> )			
			D band	D' band	G band	D' band
GO	2.24	0.38	1348.6	1519.7	1586.1	1620.0

The above results show that the prepared GO in this work consists of nanosheet, wrinkled sheet and porous structure. It exhibits main components which are C=C (sp<sup>2</sup>), C-C (sp<sup>3</sup>), C-O, C=O and COOH in agreement with other research.

## 4.2 Nitrogen doped reduced graphene oxide (N-rGO)

Nitrogen doped reduced graphene oxide (N-rGO) electrode was synthesized from the prepared GO by using a conventional hydrothermal method. Urea was used as a nitrogen source. Three N-rGO electrodes with different urea contents of 20%, 40%, and 60% (w/v) were prepared which were labeled as N-rGO20, N-rGO40, N-rGO60 electrodes, respectively. The electrodes were assembled as supercapacitor coin cells as explained in Chapter III. 1 M of H<sub>2</sub>SO<sub>4</sub> in DI water was used as electrolyte. Their electrochemical performances were evaluated via cyclic voltammetry (CV), galvanostatic charge-discharge (GCD) and electrochemical impedance spectroscopy (EIS) measurement. In addition, electrodes were characterized by using scanning electron microscopy (SEM), X-ray diffraction (XRD), Fourier transform spectroscopy (FT-IR), X-ray photoelectron spectroscopy (XPS), Raman spectroscopy, and contact angle measurement to understand the material properties.

### 4.2.1 Electrochemical performances

Firstly, the specific capacitance of all coin cell supercapacitors were assessed using Galvanostatic charge-discharge (GCD) and Cyclic voltammetry (CV) with expand operating voltage from 1 V to 1.0 V. Then, CV measurements were evaluated with varies

potential scan rate as 5, 10, 25, 50, 100, 200, 500  $\text{mV s}^{-1}$ . GCD were measured with different constant currents of 0.125, 0.25 0.50, 1, 2, 5 and 10  $\text{A g}^{-1}$ . Finally, individual electrodes were further characterized using electrochemical impedance spectroscopy (EIS).

#### 4.2.1.1 The specific capacitance

All rGO, N-rGO20, N-rGO40, and N-rGO60 SCs coin cells were evaluated electrode performance via the specific capacitance ( $C_{\text{sp}}$ ). Galvanostatic charge/discharge curves showed longer discharge time for urea doped coin cells which are 44.8, 129, 294, and 161 s for rGO, N-rGO20, N-rGO40, and N-rGO60, respectively at 0.125  $\text{A g}^{-1}$  shown in Figure 4.7 (e)- (h). Discharge feature of N-rGO40 showed a little bit curve at potential 0.3-0.4 V which showed signal from pseudocapacitive behavior. Cyclic voltammetry loops showed bigger loop with a little bit signal of pseudocapacitance at after urea doping. For the best urea concentration, CV loops of N-rGO40 SCs coin cell showed obvious quasi-rectangular shapes with a board oxidation and reduction signals which are approximately 0.3 – 0.5 V for all potential scan rate similar with GCD measurement, confirming mainly EDLCs behavior with pseudocapacitive ability as shown in Figure 4.7 (c), (g). These clear signals may be caused the highest the specific capacitance for N-rGO40 coin cell.

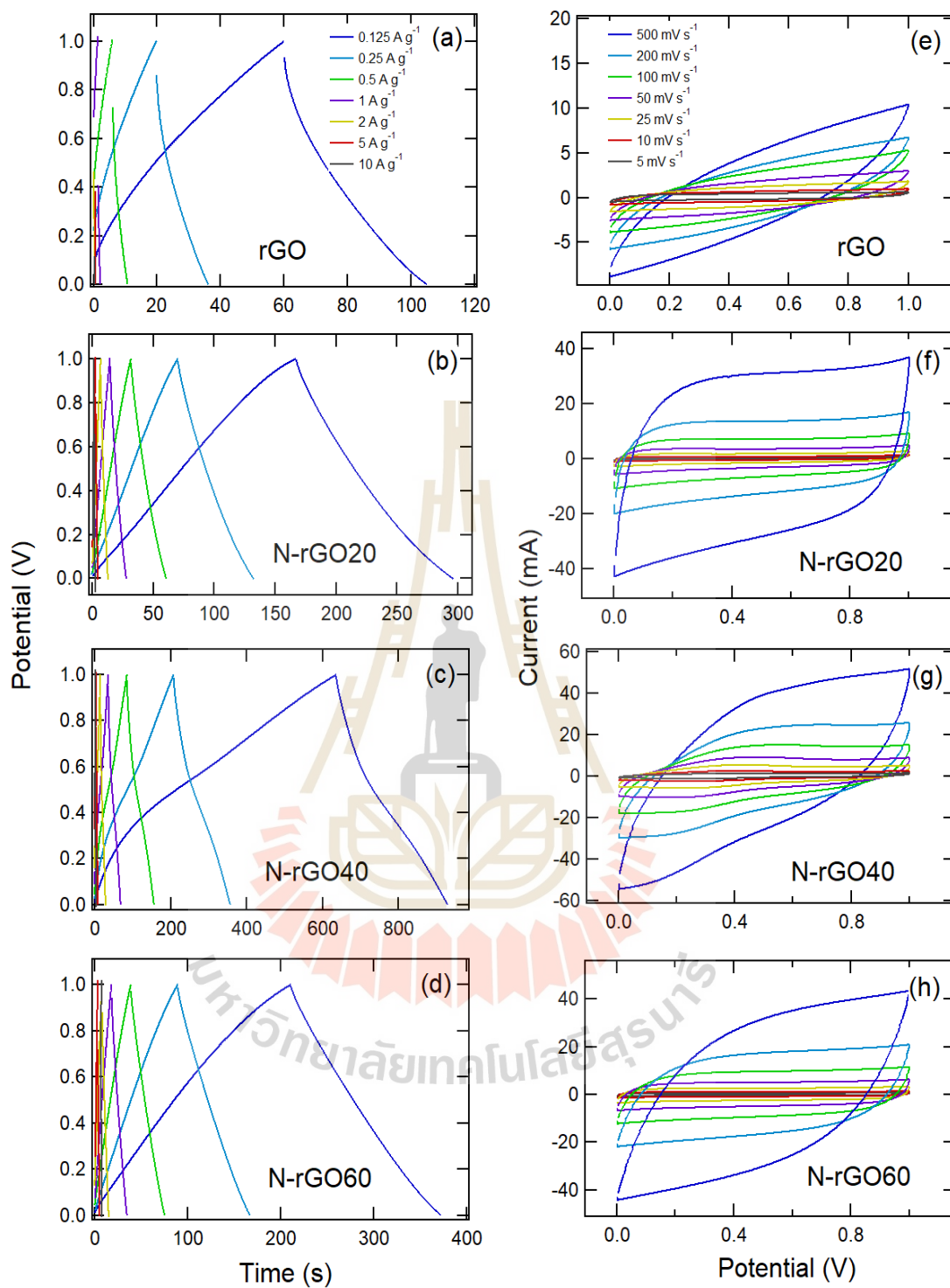


**Figure 4.7** GCD (a)-(d), CV (e)-(h) of rGO, and N-rGOY SCs coin cells.

To show the conclude performance results, for nitrogen doped reduced graphene oxide (N-rGOY), the specific capacitance of all measurements showed higher supercapacitor coin cells performance with all N-rGOY electrode, compared to rGO electrode. These enhancements can be attributed via improving of electron transfer from nitrogen-lone-pair electron to  $\pi$ -orbital of carbon in graphene structures, resulting in an improvement of wettability, electronic conductivity, and electrochemical performance as well as providing pseudocapacitance (Śliwak et al., 2017) (Liao et al., 2016).

Moreover, according to the best electrode is N-rGO40 which showed higher Csp than N-rGO20, maybe exhibit a best electrode material because of the optimal number of nitrogen-containing functional groups in graphene then Figure 4.8 (a) and (b) showed highest of pseudocapacitance influence with rapid decreasing of the specific capacitance with increasing of constant current and potential scan rate (Borenstein et al., 2018). Furthermore, Csp of N-rGO60 < N-rGO40 electrode which may be attributed the decreasing of performance which might be explained an excess amount of insulating urea blocking active sites of graphene (Soo, Loh, Mohamad, Daud, and Wong, 2016).

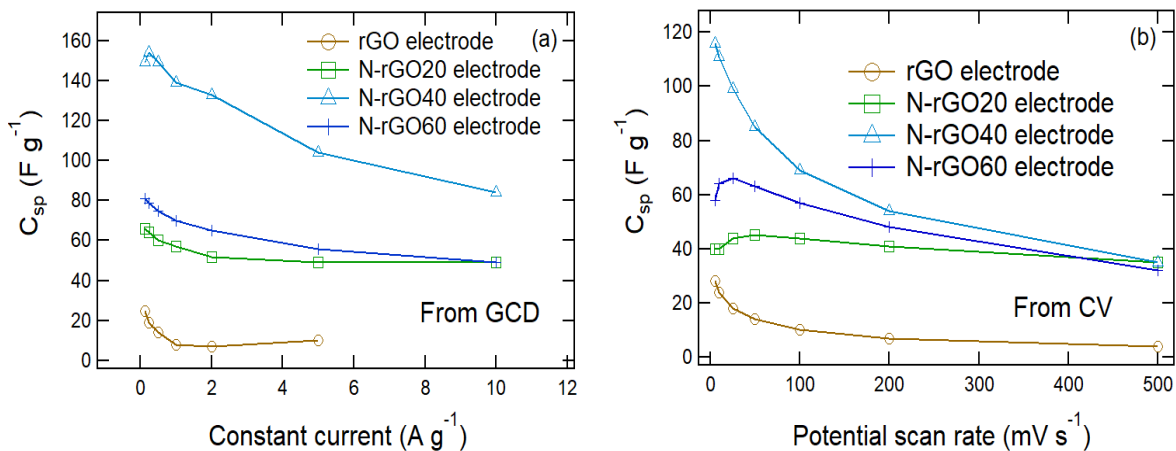


**Figure 4.8** The specific capacitance from GCD and CV measurement of rGO, and N-rGOY SCs coin cells.

#### 4.2.1.2 Electrochemical impedance spectroscopy (EIS) of rGO and N-rGOY SCs coin cells

To evaluate charge electrode transfer resistance, we can interpret EIS measurement as the following, Figure 4.9 showed all nitrogen condition which were doped, and reduced graphene oxide can help to increase electrical conductivity of electrode as shown in following. Electrode resistance can be obtained from the  $x$ -axis intercept as  $N\text{-rGO}20 > N\text{-rGO}40 > N\text{-rGO}60 > rGO$  SCs coin cells. Electrode electrolyte resistance are decreased as  $N\text{-rGO}20 < N\text{-rGO}40 < N\text{-rGO}60 < rGO$  SCs coin cells which were observed from  $R_{\infty}$  at semicircle. Furthermore, higher slope at low frequency and diffusion layer resistance ( $R_D$ ) region can be showed in all nitrogen doped reduced graphene oxide that showed more electrical conductivity at the interface between electrode-electrolyte and electrolyte ions diffusion (Taberna et al., 2006) (Sing, 1985) (D. Zhu et al., 2017) as shown in Table 4.2.

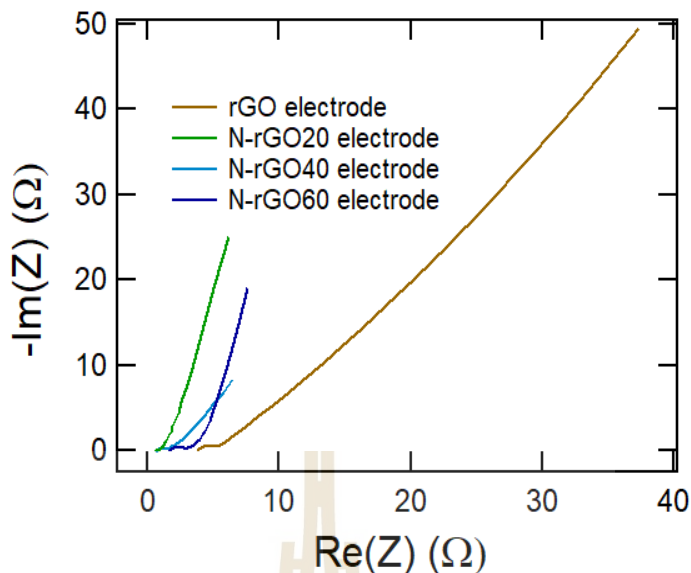


**Figure 4.9** Electrochemical impedance spectroscopy result from rGO and N-rGOY coin cells.

In this thesis, N-rGO40 SCs coin cells is the best performance condition when the specific capacitance is evaluated as Farad per gram ( $F g^{-1}$ ) then concluded results as shown in Table 4.2.

**Table 4.2** Electrochemical performance results of rGO and all N-rGOY SCs coin cell.

Electrode	GCD		CV		EIS		
	Best $C_{sp}$ ( $F g^{-1}$ )	Position of pseudo-peak (V)	Best $C_{sp}$ ( $F g^{-1}$ )	Position of pseudo-peak (V)	$R_e$	$R_e + R_{\infty}$	Slope at $R_D$ region and slope at low f
rGO	25	-	28	-	3.85	5.50	N-rGO20 $\approx$ N-rGO60 > N-rGO40 > rGO
N-rGO20	66	-	45	-	0.66	0.88	
N-rGO40	158	0.3-0.4	158	0.3-0.5	0.73	1.35	
N-rGO60	81	-	66	-	1.69	2.89	

Furthermore, N-rGO20, N-rGO40, and N-rGO60 SCs coin cells also showed improvement of a weak point for supercapacitor which is better energy density than undoped or rGO and still exhibit a bit higher of power density, compare with rGO as shown in Table 4.3.

**Table 4.3** The operating voltage, discharging time, specific capacitances, energy densities and power densities of SCs using rGO, N-rGO20, N-rGO40 and N-rGO60 electrodes in 1 M H<sub>2</sub>SO<sub>4</sub> at 0.125 A g<sup>-1</sup>.

Electrode	$\Delta V$ (V)	$\Delta t_{\text{discharge}}$ (s)	$C_{\text{sp}}$ (F g <sup>-1</sup> )	E (W h kg <sup>-1</sup> )	P (W kg <sup>-1</sup> )
rGO	0.93	45	24.2	0.73	58.1
N-rGO20	0.99	129	65.2	2.2	61.8
N-rGO40	0.99	294	149	5.1	61.9
N-rGO60	0.99	161	81.3	2.8	61.9

#### 4.2.1.3 Capacitive retention of of rGO and N-rGOY SCs coin cells

To show long term stabilities of a coin cell supercapacitors, only rGO and N-rGO40 SCs coin cells were tested capacitive retention with GCD at 1 A g<sup>-1</sup> for 10,000 cycles (there is limitation with other conditions because not enough time for measurement). Subsequently, the specific capacitance and percentage of capacitive retention of N-rGO40 SCs coin cell was a bit greater than that of rGO SCs coin cell, as 97% and 95% after 10,000 charge-discharge cycles as shown in Figure 4.10. That can imply nitrogen doped, could be used for extending life cycle for supercapacitor electrode. Unfortunately, we have available cells for testing only rGO, and N-rGO40 SCs coin cells.

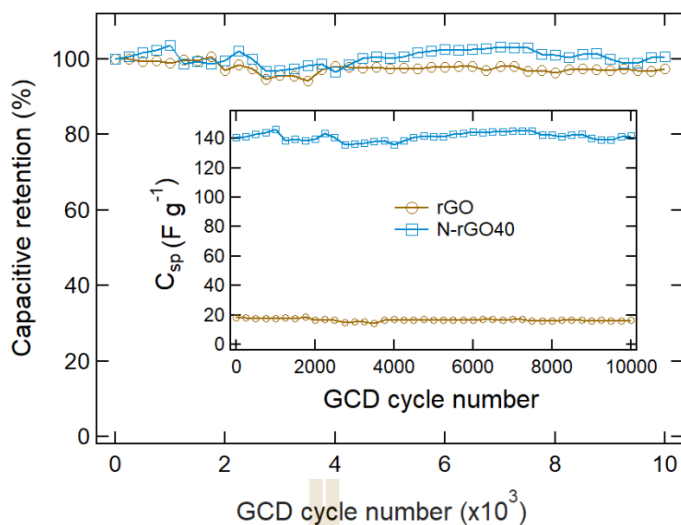


**Figure 4.10** Percentage and the specific capacitance of capacitive retentions of rGO and N-rGO40 coin cells.

#### 4.2.1.4 Leakage current of rGO and N-rGOY coin cells

Moreover, Nitrogen doped reduced graphene oxide electrode can obviously help the decreasing of leakage current and self-discharge, compare with non-doped (rGO) as shown in Figure 4.11. The improvement may be attributed the reduced oxygen functional (S. Yuan et al., 2020) after nitrogen doping. Unfortunately, we have available cells for testing only rGO, N-rGO20 and N-rGO40 SCs coin cells because another coin cell was broked before measurement.

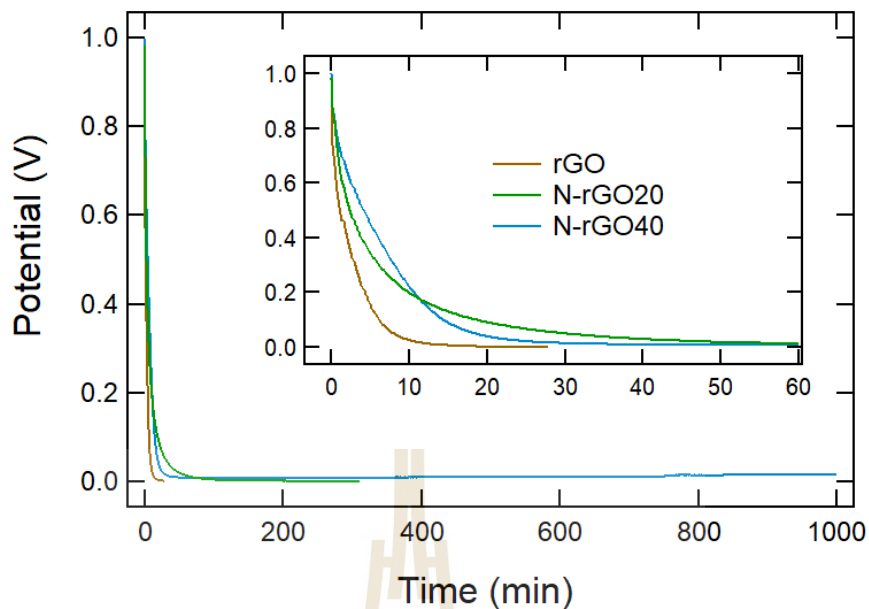


**Figure 4.11** Percentage and the specific capacitance of capacitive retentions of rGO, N-rGO20 and N-rGO40 SCs coin cells.

## 4.2.2 Characterization

### 4.2.2.1 Scanning electron microscopy

SEM images of rGO, N-rGO20, N-rGO40, and N-rGO60 electrodes are shown in Figure 4.12. These images showed quite similar morphology which nanosheet of GO, wrinkle surface. For 10k X of magnification, all nitrogen doped electrodes exhibited mixing with the distribution of nano particles insert along graphene oxide structure when compare with rGO electrode as also shown in Figure 4.12.

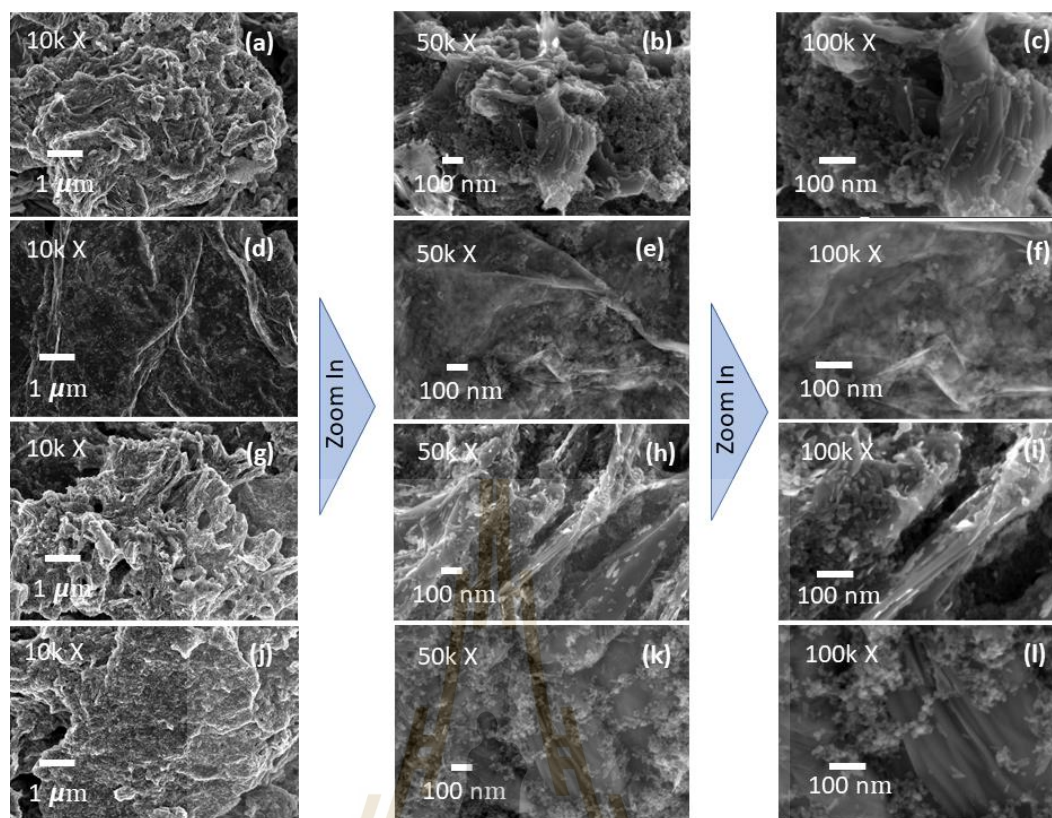


**Figure 4.12** SEM images of rGO (a)-(c), N-rGO20 (d)-(f), N-rGO40 (g)-(i), and N-rGO60 electrode (j), (l) with difference magnifications.

Moreover, cross-section SEM image showed thickness of N-rGO40 electrode film which used to represent all of electrode thickness are around 80  $\mu\text{m}$  as shown in Figure 4.13.

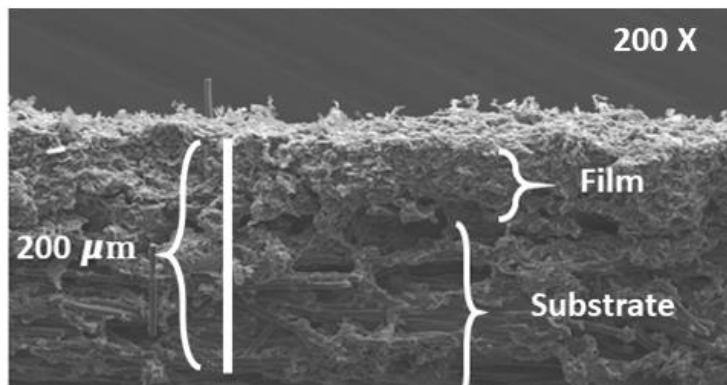


**Figure 4.13** Cross-section SEM image of N-rGO40 electrode for showing thickness of all activated film materials.

#### 4.2.2.2 X-ray diffraction

XRD showed crystalline plan of rGO and N-rGO electrode. Here, we chose only rGO electrode as undoped graphene oxide condition and N-rGO40 electrode as the best condition for nitrogen doped reduced graphene oxide condition for comparison as shown in Figure 4.14. XRD results of both conditions showed same peaks as the following, located peak at  $2\theta \sim 36.3^\circ$ ,  $45^\circ$ ,  $65^\circ$ , and  $78^\circ$  could be identified as plan peaks (002), (111), (103) and (220) which came from graphitic plan, PVDF, and carbon black (Pang et al., 2010) (Roy, Deb, Bhattacharjee, and Pal, 2002) (Ungar et al., 2002).

Furthermore, XRD of only N-rGO40 electrode maybe further attribute crystalline plan of nitrogen which showed more diffraction peaks at  $2\theta \sim 43^\circ$ ,  $51^\circ$ , and  $76^\circ$ , corresponding to (10) or (100), (102), and (110) which indicate a short-range order in stacked graphene layers, more graphite plan state (Pang et al., 2010) (Stobinski et al., 2014).

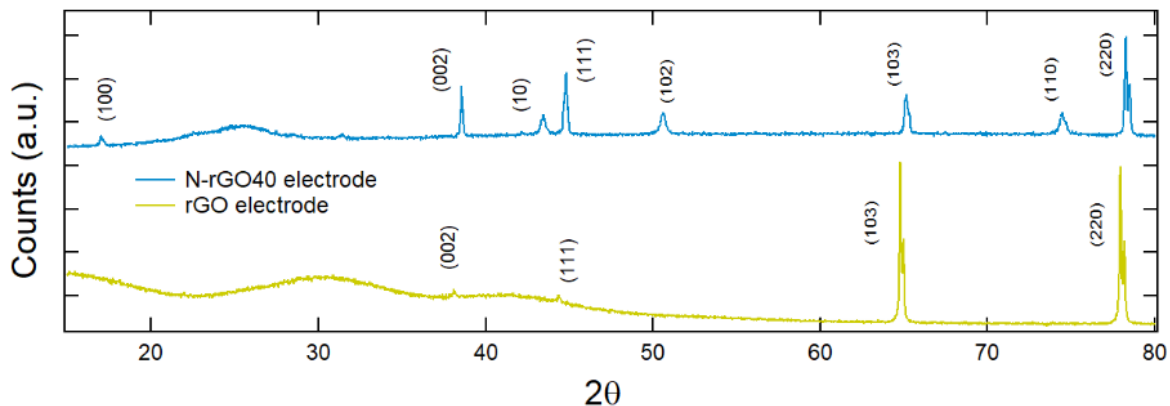


**Figure 4.14** XRD pattern of rGO and N-rGO40 electrodes.

#### 4.2.2.3 Fourier transform infrared (FT-IR)

To investigate chemical bonding, FT-IR results of all electrodes were showed transmission peak as  $\sim 728, 875, 1068, 1175, 1390, 1540, 1650 \text{ cm}^{-1}$ , corresponding to  $\beta$ -phase in PVDF, C-O, C-N, O-C-O, O-C=O, CHN, and C=C as shown in Table 3.2. Furthermore, spectrum for rGO electrode showed highest transmission peak for C=C and these spectra for all N-rGOY showed lower transmission peak for O-C-O that can be implied nitrogen doped reduced GO may destroy some of graphene structure and nitrogen can completely be doped and reduced graphene oxide, respectively.

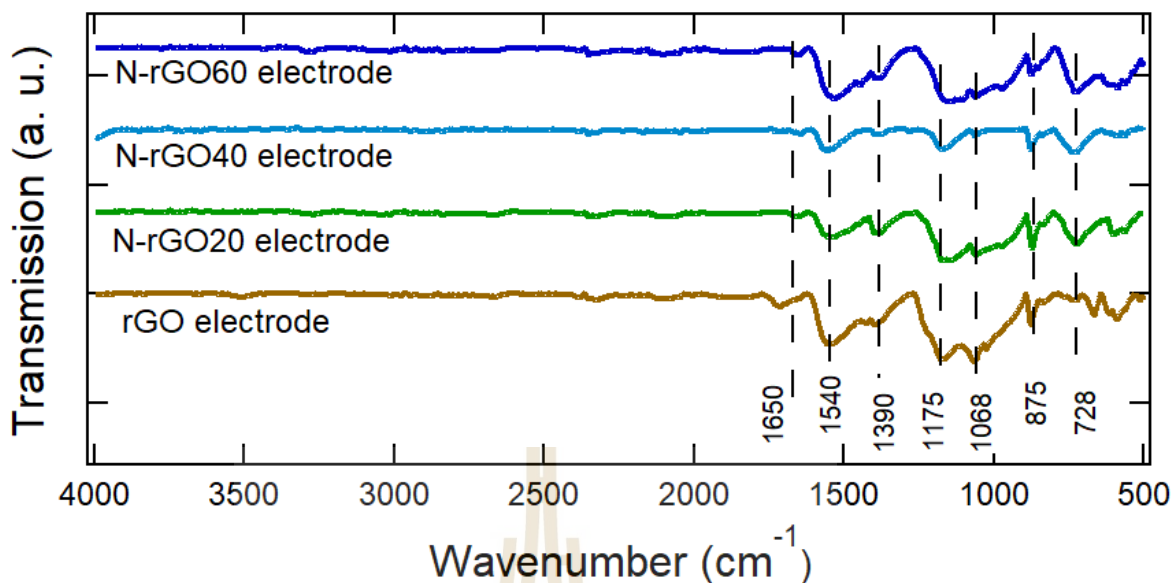


**Figure 4.15** FT-IR results of rGO, N-rGO20, N-rGO40 and N-rGO60 electrode.

#### 4.2.2.4 X-ray photoelectron spectroscopy

X-ray photoelectron spectroscopy (XPS) were performed to investigate chemical compositions on all N-rGOY electrodes. Wide scans of rGO, N-rGO20, N-rGO40 and N-rGO60 electrodes were recorded in the binding energies range from 0 to 550 eV which included carbon, oxygen on all electrodes and a little nitrogen peak on N-rGO20, N-rGO40 and N-rGO60 electrodes as shown in Figure 4.16 (a). To analysis surface chemical compositions, the high resolution XPS spectra of C1s signal of rGO, N-rGO20, N-rGO40 and N-rGO60 electrodes are displayed in Figure 4.19 (b) – (e). The XPS spectrum of C1s comprised C=C ( $sp^2$ ), C-O/C-N, C=O/C=N, COOH, CHF, and C-F at binding energies of 284.5, 285.3, 286.8, 288.4, 289.2 and 292.0 eV, respectively (Zhuo et al., 2015) (K. H. An et al., 2002) (Biniak et al., 1997) (Kelemen and Kwiatek, 1995). Figure 4.16 (c)- (e) showed influence of nitrogen doped reduced graphene oxide that

affect to decrease of C=C peak but increase C-O/C-N, C=O/C=N. That can be implied nitrogen can be doped in graphene oxide structure.

To check reduced oxygen on rGO, N-rGO electrode, the signal of O1s are shown oxygen-containing functional groups such as C=O, C-OH/C-O-C, and COOH/water at binding energies of 531.5, 533.0, 534.5 eV, respectively (Zielke et al., 1996) (Lorenc-Grabowska et al., 2013). Figure 4.16 (f)- (i) showed influence of nitrogen doped reduced graphene oxide that affect to decrease C=O peak but increase COOH and water peaks.

Moreover, N-rGO20, N-rGO40 and N-rGO60 electrodes revealed nitrogen-containing functional groups such pyridinic-N, pyrrolic-N, and quaternary-N at binding energies of 398.3, 400.5 and 404.5 eV, respectively (Lorenc-Grabowska et al., 2013) (Śliwak et al., 2017) (Kapteijn, Moulijn, Matzner, and Boehm, 1999). Notice point for N-rGO40 electrode is highest exhibition of pyridinic-N than both N-rGO20 and N-rGO60 as shown in Figure 4.16 (j)- (l).

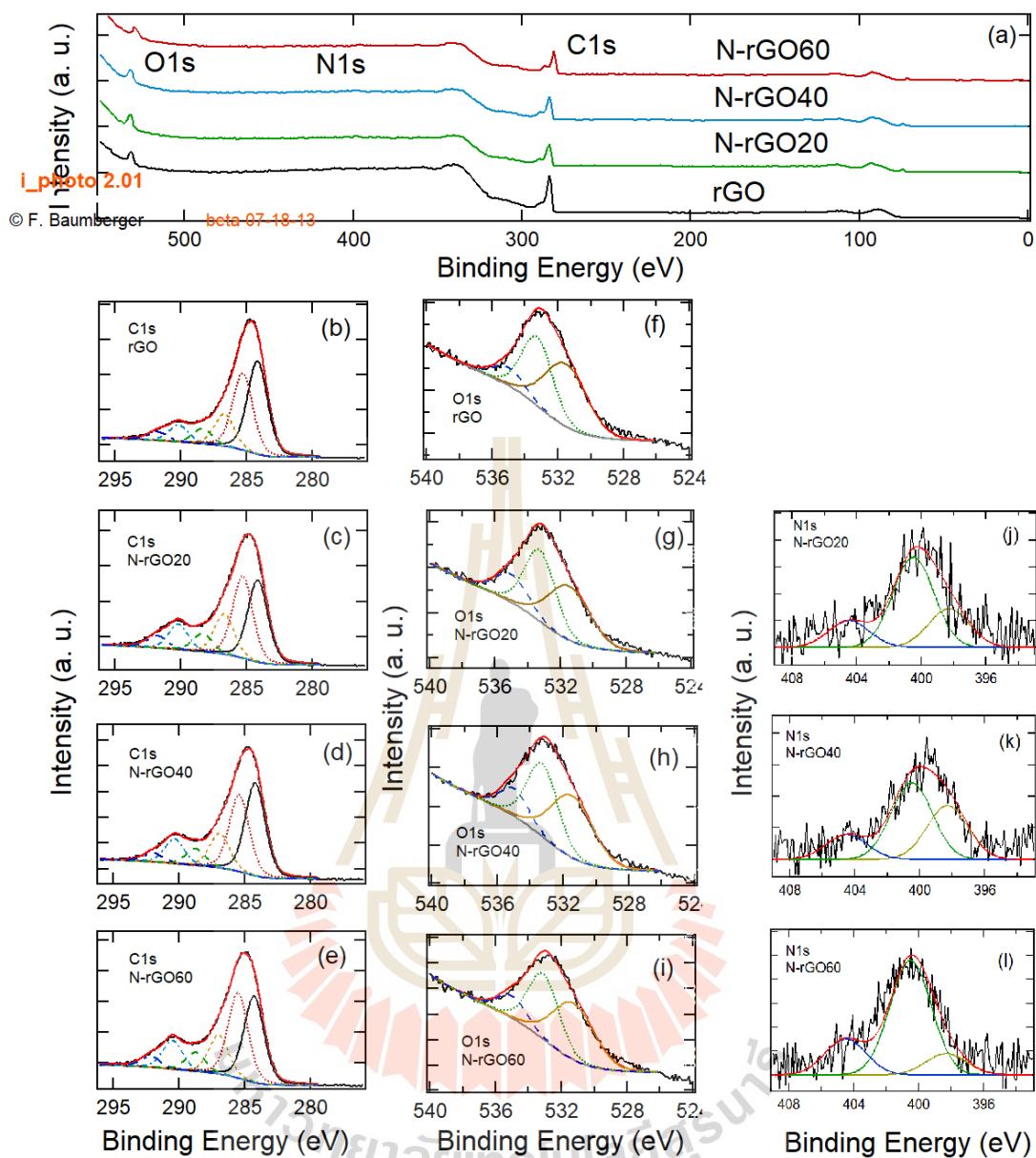


**Figure 4.16** Wide scan of spectra from rGO and N-rGOY electrodes (a), Fine scan C1s peak spectra from rGO and N-rGOY electrodes (b) (c) (d) (e), Fine scan O1s peak spectra from rGO and N-rGOY electrodes (f) (g) (h) (i), Fine scan N1s peak spectra from N-rGOY electrodes.

There are some more noticed points which can be attribute the relationship between quantitative bonding and electrode performance. The different quantity of remained  $sp^2$  and appeared pyridinic- N of N-rGO40 electrode showed highest volume after hydrothermal treatment with urea and preparing electrode process. Therefore, these two factors might be caused high electrical conductivity and highest pseudocapacitance of N-rGO40 condition as shown in Figure 4.17.

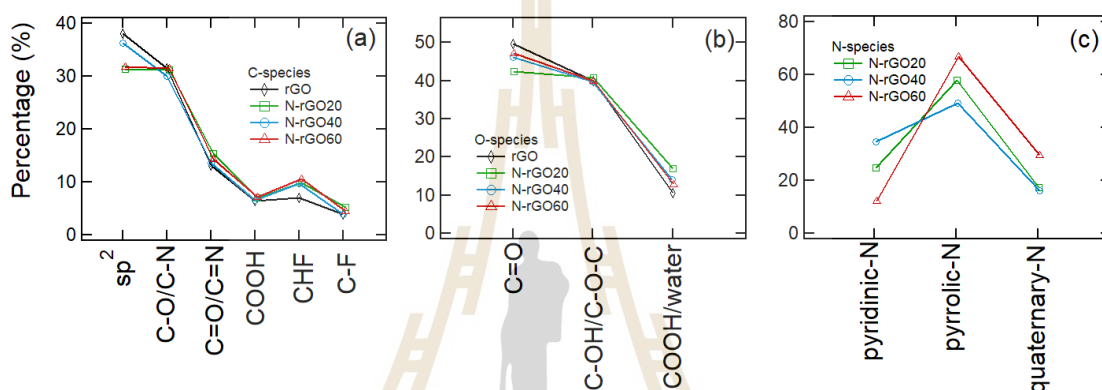


**Figure 4.17** Percentage of each bonding in C1s, O1s, and N1s for rGO, N-rGO20, N-rGO40 and N-rGO60 electrodes.

To more analyzation, relative  $C=C$  ( $sp^2$ ) is the calculation of area of  $sp^2$  per other peaks area which can be implied remained  $C=C$  ( $sp^2$ ) structure after hydrothermal with varies urea concentrations. The results from Table 4.4 showed using 40% urea concentration, could maintain graphene structure lower than 20, and 60% (w/v) that might be implied nitrogen could be successful for introducing into graphene state. Table 4.5 and 4.6 showed peak position and area under each peak for O1s and N1s peak, respectively. To support N-rGO40 electrode as the best condition, the highest of relative

pyridinic-N might be attributed the possible providing of pseudocapacitive behavior because the lowest bonding energy, compare with pyrrolic-N and quaternary- N.

**Table 4.4** The results of XPS curve-fitting from Figure 4.19 (b)- (e).

Electrode	Position of each bonding at C1s						Relative C=C (sp <sup>2</sup> )
	sp <sup>2</sup>	C-O/C-N	C=O/C=N	COOH	CHF	C-F	
rGO	284.2	285.4	286.7	288.4	290.1	291.8	0.62
N-rGO20	284.2	285.5	286.8	288.4	290.2	291.9	0.46
N-rGO40	284.2	285.5	286.9	288.7	290.3	292.0	0.57
N-rGO60	284.3	285.5	286.9	288.6	290.4	292.0	0.47

**Table 4.5** The results of XPS curve-fitting of O1s from Figure (f)- (i).

electrode	Position of each bonding at O1s			Area of each bonding at O1s		
	C=O	C-OH/C-O-C	COOH/water	C=O	C-OH/C-O-C	COOH/water
rGO	531.5	533.3	535.0	49.66	39.85	10.48
N-rGO20	531.5	533.3	535.0	42.41	40.64	16.95
N-rGO40	531.5	533.3	535.0	46.21	39.70	14.09
N-rGO60	531.3	533.1	535.0	47.23	39.93	12.83

**Table 4.6** The results of XPS curve-fitting of N1s from Figure (j)- (l).

electrode	Position of each bonding at N1s			Area of each bonding at N1s		
	pyridinic-N	pyrrolic-N	quaternary-N	pyridinic-N	pyrrolic-N	quaternary-N
N-rGO20	398.3	400.5	404.5	24.7	58.0	17.3
N-rGO40	398.3	400.5	404.5	34.6	49.4	16.0
N-rGO60	398.3	400.5	404.5	12.2	67.0	20.8

#### 4.2.2.5 Raman spectroscopy

Raman spectroscopy showed higher disorder (D band peak) after nitrogen doped reduced graphene oxide that related with SEM image that showed more complex morphology or more amorphous. Raman spectra of rGO, N-rGO20, N-rGO40, and N-rGO60 electrodes exhibited a pair of strong peak at  $\sim 1586$  and  $\sim 1328$   $\text{cm}^{-1}$ , corresponding to graphitic carbon phase with  $\text{sp}^2$ -hybridization (G-band) and defect graphite structure (D-band), respectively (Tuinstra and Koenig, 1970) as shown in Figure 4.18. All electrodes showed structure based on graphene with disorder state. D' band of N-rGO20, N-rGO60 electrodes showed lower that has been attributed to the disorder-induced phonon mode due to crystal defects, lower than rGO and N-rGO40 electrode as shown in Table 4.7.

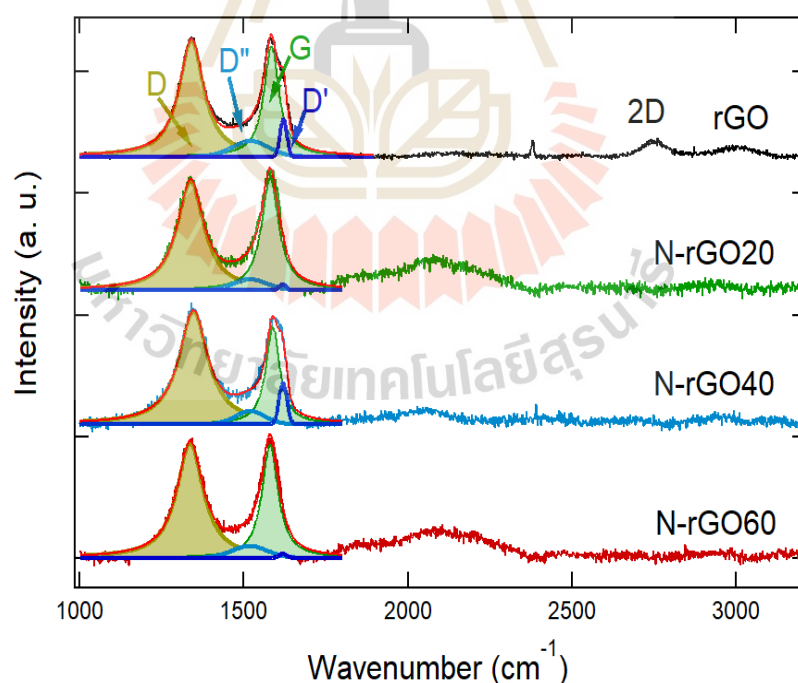


**Figure 4.18** Raman spectroscopy result of rGO, N-rGO20, N-rGO40, and N-rGO60 electrodes.

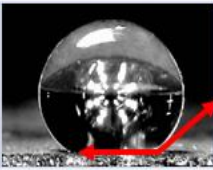
According to the highest  $I_D/I_G$  of N-rGO40 electrode might be attributed the highest introduction of nitrogen functional groups into GO structure or creation of disorder state.

**Table 4.7** The fitted data and analyzed data of Raman spectra curves.

electrode	$I_D/I_G$	$I_{D'}/I_G$	Position			
			D	D''	G	D'
rGO	1.71	0.23	1340.9	1520.5	1584.6	1620.9
N-rGO20	1.51	0.13	1338.4	1520.6	1580.8	1618.7
N-rGO40	2.42	0.19	1346.8	1520.3	1588.7	1619.7
N-rGO60	1.66	0.16	1336.7	1518.5	1580.2	1619.6

#### 4.2.2.6 Contact angle

Wettability of graphene oxide was enhance using heteroatom or nitrogen doping (Szciodrowski, Pr elot, Lantenois, Douillard, and Zajac, 2009) with all urea concentration which can be explained via contact angle of  $rGO > N-rGO60 > N-rGO20 > N-rGO40$  electrode as shown in Figure 4.19. N-rGO40 electrode exhibit lowest contact angle as  $142.8^\circ$  that implied higher possible possess of surface energy expectation on nanomaterials of N-rGO40 electrode surface (B ockman,  ostvold, Voyiatzis, and Papatheodorou, 2000) (Mane et al., 2009). Then the reason is a more reason to cause highest the specific capacitance on the electrode condition.

Electrode	Picture	Contact angle
rGO		149.8°
N-rGO20		143.8°
N-rGO40		142.8°
N-rGO60		146.0°

**Figure 4.19** Contact angle of rGO and N-rGOY electrodes with 1 M H<sub>2</sub>SO<sub>4</sub> in DI water as electrolyte.

### 4.3 Comparative study of structural and electrochemical properties of reduced graphene oxide, nitrogen doped reduced graphene oxide, and nitrogen and sulfur co-doped reduced graphene oxide.

According to proposal examination, we introduced N-rGO and another possible strategies to improve intrinsic and surface of graphene oxide that is nitrogen and sulfur co-doping on graphene oxide, called NandS-rGO. Subsequently, we noticed some comparative study for between N-rGO electrode (main point in this thesis) and NandS-rGO electrode and rGO electrode. The study showed the difference effect of monomer-doping (N from urea: CH<sub>4</sub>N<sub>2</sub>O as nitrogen source) and co-doping (N and S from thiourea:

CH<sub>4</sub>N<sub>2</sub>S as nitrogen and sulfur source). After that, SCs coin cells of all electrodes were evaluated electrochemical performance via CV, GCD, and EIS. Finally, electrodes would be used for characterization for relating with their performance.

#### 4.3.1 Electrochemical performance

In electrochemical performance, all rGO, N-rGO, and NandS-rGO SCs coin cells provided CV loop, GCD curve, and EIS as shown in following.

##### 4.3.1.1 The specific capacitance of rGO, N-rGO, and NandS-rGO SCs coin cells

According to we reported discharge feature of N-rGO40 SCs coin cell showed a little bit curve at potential 0.3-0.4 V which showed signal from pseudocapacitive behavior. Cyclic voltammetry loops showed bigger loop with a little bit signal of pseudocapacitance at after urea doping which showed obvious quasi-rectangular shapes with a board oxidation and reduction signals which are approximately 0.3 – 0.5 V, confirming mainly EDLCs behavior with pseudocapacitive ability as shown in Figure 4.20 (b), (e). But there isn't these signals in rGO and NandS-rGO SCs coin cell then we might use this reason to explain the highest performance for N-rGO SCs coin cell.

For the thiourea, CV loops showed bigger than rGO or non doped SCs coin cells. GCD curve showed discharge time of N-rGO SCs coin cells longer than NandS-rGO and rGO SCs coin cells as shown if Figure 4.20.

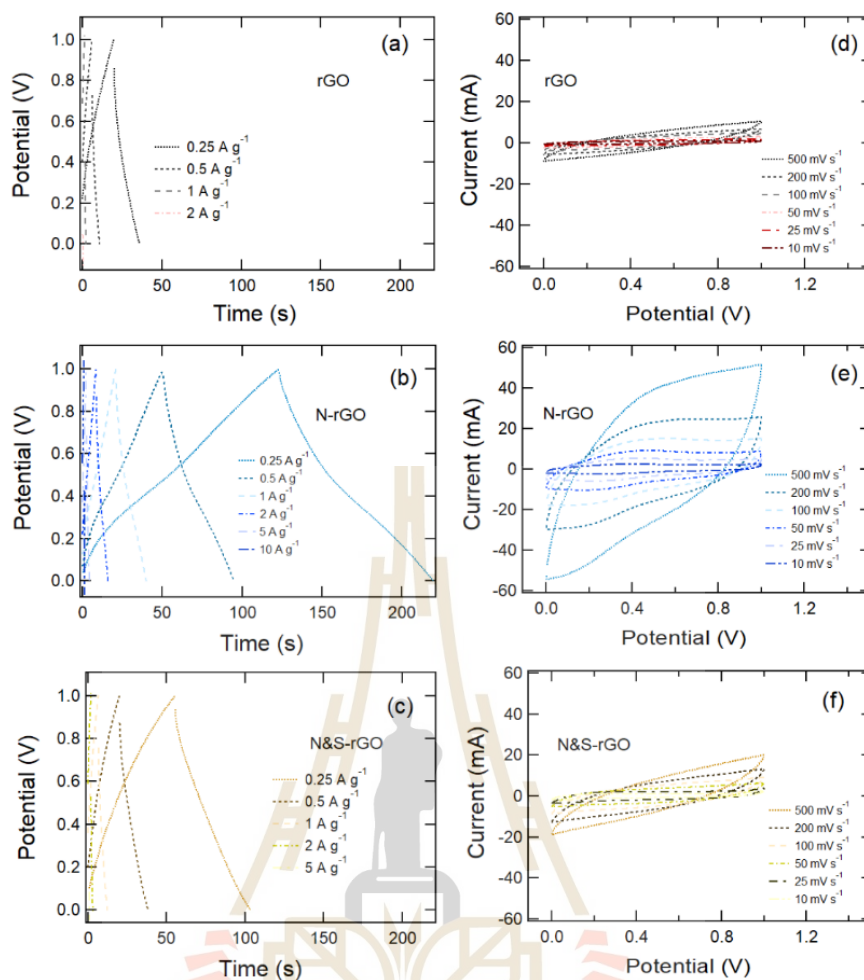


**Figure 4.20** GCD (a)- (c), CV (d)-(f) of rGO, N-rGO, and NandS-rGO SCs coin cells in 1 M H<sub>2</sub>SO<sub>4</sub> in DI water as aqueous electrolyte.

Furthermore, the specific capacitance ( $C_{sp}$ ) of coin cells with electrode as N-rGO > NandS-rGO > rGO for 1 M H<sub>2</sub>SO<sub>4</sub> electrolyte as shown in Figure 4.21. The results showed trend of the specific capacitance with constant current in GCD and potential scan rate for CV. The trend results showed the using nitrogen doping electrode can clearly improve of performance of supercapacitor via increase EDLCs mechanism and pseudocapacitance or redox reaction more than NandS-rGO SCs coin cells. Moreover, NandS-rGO SCs coin cells clearly showed higher performance from rGO SCs

coin cells that maybe attributed by pseudocapacitance from sulfur functional groups cooperation with EDLCs.

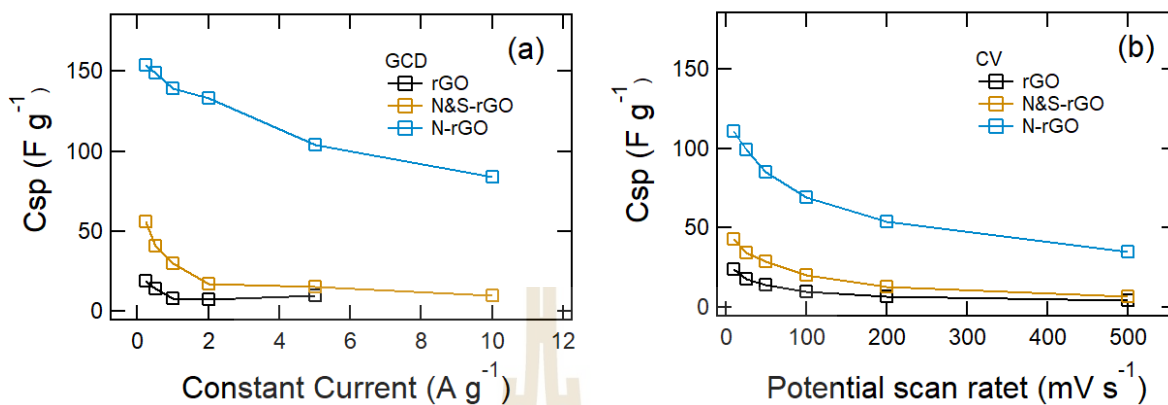


**Figure 4.21** Calculated the specific capacitance from GCD and CV results of rGO, N-rGO, and NandS-rGO coin cells.

#### 4.3.1.2 EIS of rGO, N-rGO, and NandS-rGO SCs coin cells

The electrochemical behavior at the electrode/electrolyte interface was reported by EIS, showed both N-rGO and NandS-rGO SCs coin cells can achieve the decreasing of electrode ( $R_e$ ) and electrode/electrolyte resistance ( $R_e + R_{\alpha}$ ). Furthermore, slope at low frequency of N-rGO SCs coin cells result clearly showed increasing of charge diffusion rate more than NandS-rGO and rGO SCs coin cells as shown in Figure 4.22.

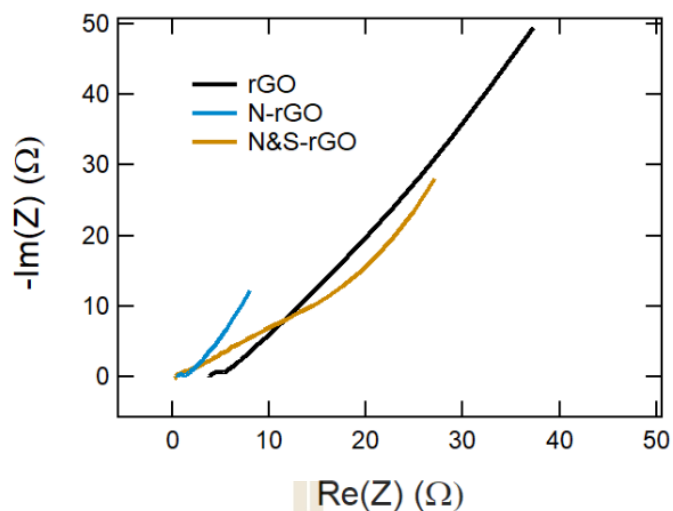


**Figure 4.22** EIS results of rGO, N-rGO, and NandS-rGO SCs coin cells.

#### 4.3.2 Scanning electron microscopy

SEM images showed graphene oxide sheet and wrinkly surface for rGO electrode. Then, after hydrothermal treatment with both urea and thiourea, both N-rGO and NandS-rGO electrode surface represented showed more nanoparticle which distribute for whole surface which might come from creation of more disorder state after hydrothermal treatment with nitrogen, and nitrogen and sulfur source as shown in Figure 4.23.

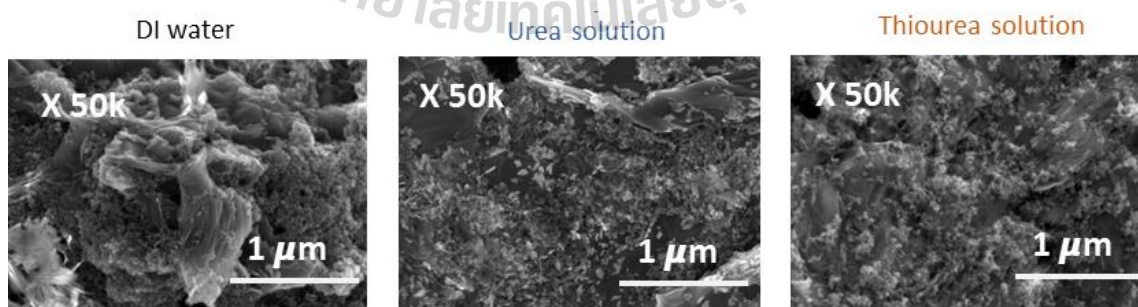


**Figure 4.23** SEM image of rGO, N-rGO, and NandS-rGO electrode.

### 4.3.3 Fourier transform infrared spectroscopy (FT-IR)

FT-IR clearly showed absorption peak at  $1713\text{ cm}^{-1}$ , and  $1168\text{ cm}^{-1}$  correspond to C=O (carbonyl), and O-C-O (epoxy), respectively for rGO electrode. After that, N and NandS doping electrode showed decreasing of C=O (carbonyl), and O-C-O (epoxy) which might attribute by oxygen functional groups were replaced nitrogen and sulfur functional groups. Moreover, there are nitrogen functional groups obviously occur peak that are absorption peaks around  $1056\text{ cm}^{-1}$ , and around  $820\text{ cm}^{-1}$ , correspond to the bending vibration of C-N, N-H, respectively as shown in Figure 4.24.

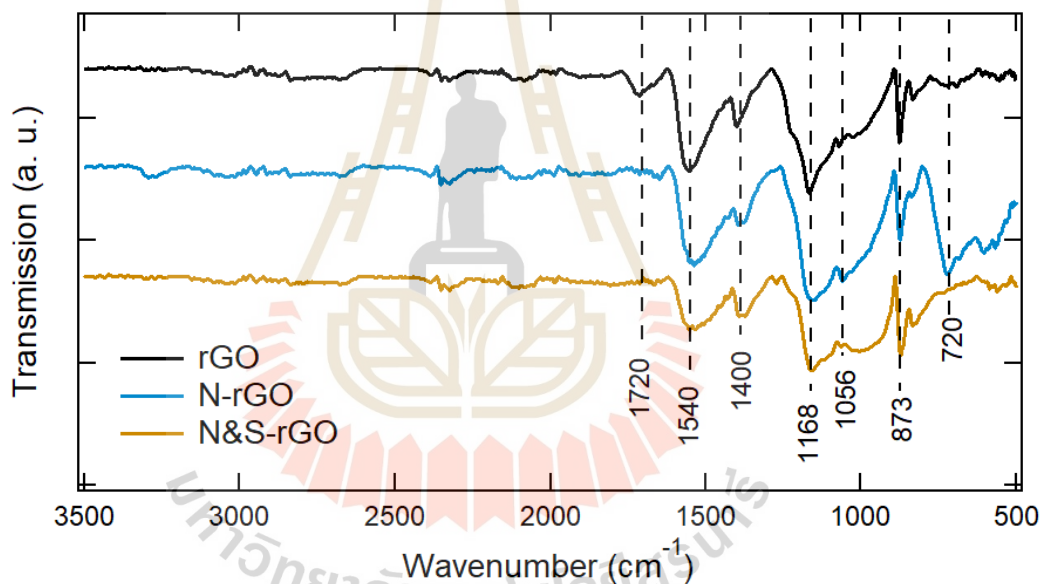


**Figure 4.24** FT-IR results of rGO, N-rGO, and NandS-rGO electrodes.

### 4.3.4 X-ray photoelectron spectroscopy

X-ray photoelectron spectroscopy showed C, O are main element for all electrode but more N for both doping and more S for only NandS-rGO electrode as shown in Figure 4.25(a).

To clearly investigate chemical composition, High resolution XPS was performed to check C1s, O1s, N1s, and S2p spectrum which were deconvoluted as shown in Figure 4.26 (b)-(j). The XPS spectrum of C1s comprised C=C ( $sp^2$ ) (C-1), C-O (C-2), C=O (C-3), COOH/CHF (C-4), and C-F (C-5) at binding energies of 284.5, 286.5, 287.5, 289, and 290.5 eV, respectively (Biniak et al., 1997) (K. H. An et al., 2002) (Kelemen and Kwiatek, 1995) (Zhuo et al., 2015). To check oxygen species on surface, the signal of O1s of all electrode are shown oxygen-containing functional groups such as C=O (O-1), C-OH (C-2), C-O-C (C-3) and water (C-4) at binding energies of 531.0, 532.5, 534.4 and 536.0 eV, respectively (Śliwak et al., 2017) (Lorenc-Grabowska et al., 2013) (Zielke et al., 1996). Moreover, the XPS spectrum of N1s comprised pyridinic-N (N-1), pyrrolic-N (N-2), quaternary-N (N-3), and pyridine N-oxide (N-4) at binding energies of 398.5, 400.0, 401.5 eV, and 405.5 respectively (Lorenc-Grabowska et al., 2013) (Kapteijn et al., 1999). Finally, for NandS-rGO, the XPS spectrum of S2p peak at binding energies of 164.0, 164.9, 168.9 and 169.9 eV, corresponding with C-S $2p_{3/2}$  (S-1), C-S $2p_{1/2}$  (S-2), sulphone $2p_{3/2}$  (S-3), sulphone $2p_{1/2}$  (S-4), respectively (W. S. V. Lee et al., 2015) (Y. Yang et al., 2017).

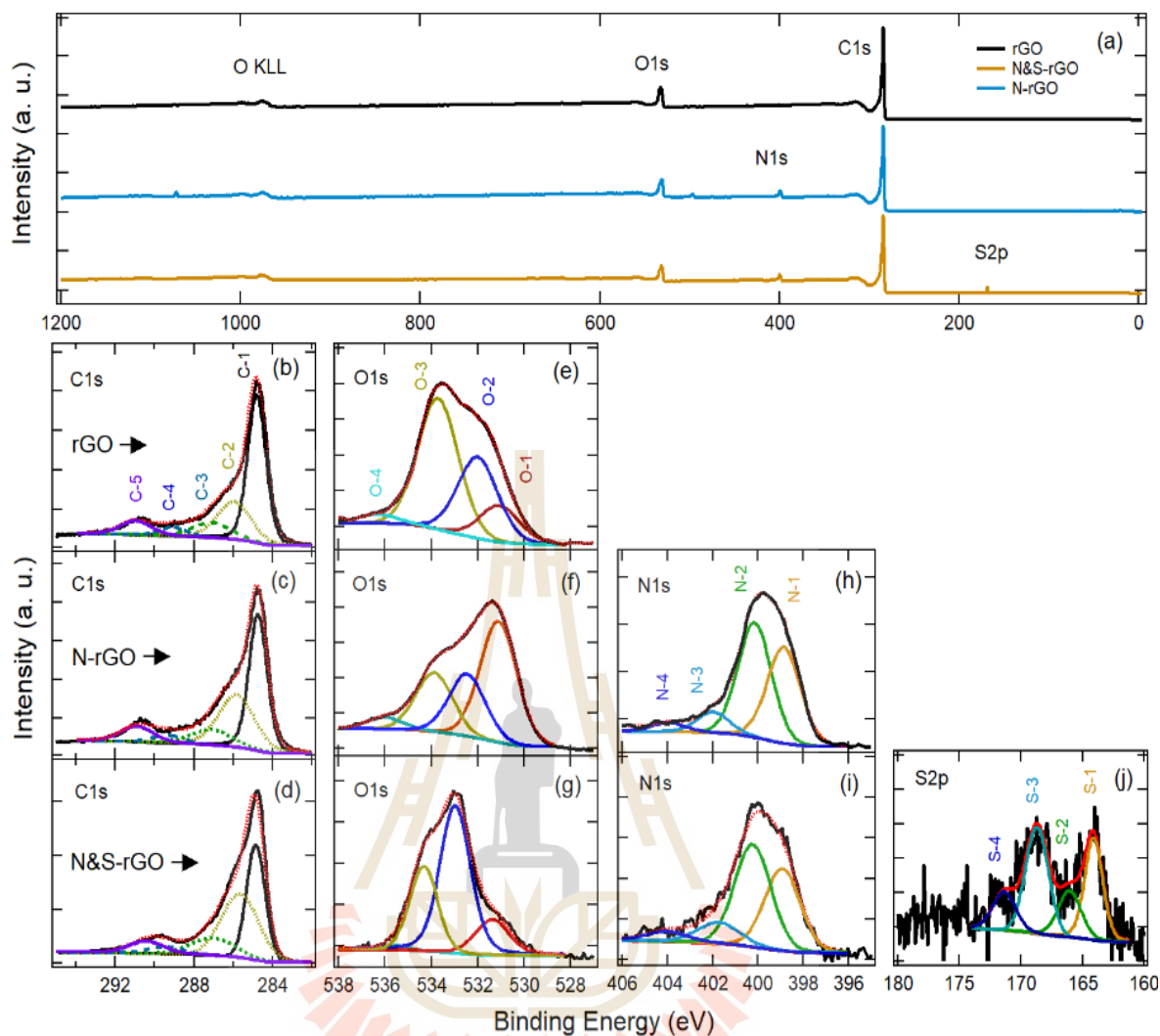


**Figure 4.25** XPS results from rGO, N-rGO, and NandS-rGO electrode.

To clearly amount of each bonding species, Table 4.8– 4.11 showed position and relative area of each bonding. Table 4.8 showed  $sp^2$  hybridization would be reduced after doped with N and further decrease after doped with N and S.

**Table 4.8** The results of XPS curve-fitting from C1s peak in Figure 4.26 (b)- (d).

Electrode	Relative C=C (sp <sup>2</sup> )	Position (eV)				
		sp <sup>2</sup> (C-1)	C-O/C-N (C-2)	C=O/C=N (C-3)	COOH (C-4)	C-F (C-5)
rGO	1.04	284.3	285.4	286.6	288.6	290.5
N-rGO	0.76	284.3	285.4	286.7	288.8	290.3
NandSrGO	0.56	284.3	285.2	256.5	288.8	290.0

Table 4.9 showed O-C will decrease after doping for both N-rGO and NandS-rGO.

**Table 4.9** The results of XPS curve-fitting from O1s peak in Figure 4.26 (e)- (g).

Electrode	Percentage of each bonding											
	Hydroxides (O-1)			O=C (O-2)			O-C (O-3)			Absorbed H <sub>2</sub> O (O-4)		
	Position	FWHM	Area	Position	FWHM	Area	Position	FWHM	Area	Position	FWHM	Area
rGO	530.8	2.0	31.6	532.0	2.0	14.1	533.5	2.0	50.8	536	2.0	3.45
N-rGO	530.8	1.9	47.5	532.2	1.9	24.5	533.5	1.9	23.3	535.8	1.9	4.6
NandS-rGO	530.8	2.1	15.2	532.2	1.7	49.5	533.5	1.8	35.1	535.7	2.0	0.2

For nitrogen species, there is a notice point that would be significant parameter for performance of supercapacitors which is N-3 showed higher quantity in N-rGO than NandS-rGO.

**Table 4.10** The results of XPS curve-fitting from N1s peak in Figure 4.26 (h), (i).

Electrode	Percentage of each bonding											
	(N-1)			(N-2)			(N-3)			(N-4)		
	Position	FWHM	Area	Position	FWHM	Area	Position	FWHM	Area	Position	FWHM	Area
N-rGO	398.3	1.9	26.8	399.6	1.9	51.1	401.5	2.4	17.6	405.8	2.3	4.4
NandS-rGO	398.4	1.9	36.1	399.7	1.9	45.9	401.6	2.2	11.8	405.7	2.2	6.2

Other species of sulfur were observed as shown in Table 4.11 which cause pseudocapacitance for NandS-rGO.

**Table 4.11** The results of XPS curve-fitting from S2p peak in Figure 4.26 (j).

Electrode	Percentage of each bonding											
	(S-1)			(S-2)			(S-3)			(S-4)		
	Position	FWHM	Area	Position	FWHM	Area	Position	FWHM	Area	Position	FWHM	Area
NandS-rGO	164.1	1.8	30.6	166.1	2.1	17.8	168.7	2.1	36.9	171.4	2.1	14.7

### 4.3.5 Raman spectroscopy

To investigate step transformation of the formation of C=C sp<sup>2</sup> graphitic carbon in graphene with varies doping condition, the Raman spectra were deconvoluted based on above mention. The fitted data of Raman spectra curves of all deconvoluted signals are summarized in in Figure 4.26 and Table 4.12. Also, the decrease in the intensity ratios between D-band and G-band ( $I_D/I_G$ ) and between D''-band and G-band ( $I_{D''}/I_G$ ) reflects an increase in the degree of C=C sp<sup>2</sup>-bonded graphitization, which implied higher disorder state after doping with N and more disorder state when doping with NandS. These results were attributed via  $I_D/I_G$ . Furthermore, the results of  $I_{D''}/I_G$  ratios decreased with doping with NandS, successful reductions of oxygen/nitrogen-containing functional groups on graphene.

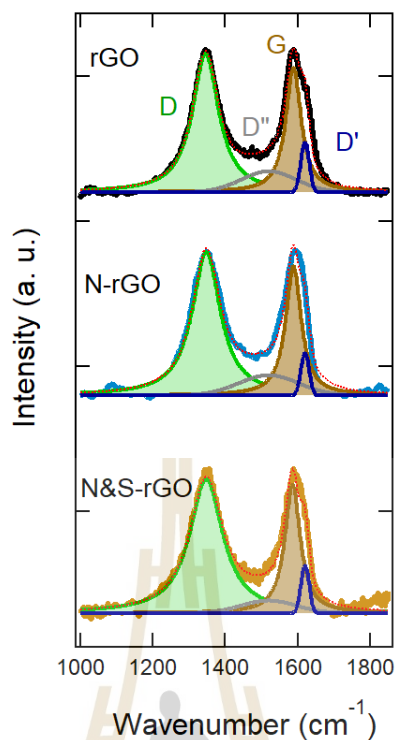


**Figure 4.26** Raman spectroscopy result of rGO, N-rGO, and NandS-rGO.

**Table 4.12** The fitted data and analyzed data of Raman spectra curves.

Electrodes	$I_D/I_G$	$I_{D''}/I_G$	Band position ( $\text{cm}^{-1}$ )			
			D band	D'' band	G band	D' band
rGO	1.88	0.40	1346.5	1521.7	1589.4	1621.3
N-rGO	1.99	0.40	1347.6	1520.4	1588.5	1620.4
andS-rGO	2.22	0.23	1347.6	1520.7	1586.0	1620.5

These results might be explained doping only nitrogen or monomer doping would be better than nitrogen and sulfur co-doping because higher electrical conductivity is more essential factor for supercapacitor than pseudocapacitive. Moreover, there are more characterizations and analyzation such atomic percentage for each element which must be done then we try to finish write manuscript for this research topic soon.

### 4.3.6 Contact angle

In this comparative study, contact angle clearly showed co-doping or NandS-rGO electrode, can increase wettability of graphene oxide more than monomer-doping or N-rGO electrode. There is a research from Dae Kyom Kim who also showed co-doping, can clearly decrease contact angle (D. K. Kim et al., 2018). Therefore, 2 Heteroatom doping as co-doping can decrease contact angle of graphene oxide than a source doping as shown in Figure 4.27.

Electrode	Pic	Contact angle
<u>rGO</u>		149.8
<u>N-rGO</u>		142.8
<u>N&amp;S-rGO</u>		97.8

**Figure 4.27** show contact angle of rGO, N-rGO, and NandS-rGO.

To conclude above results, due to electrochemical performance N-rGO and NandS-rGO showed higher than rGO that mean both urea and thiourea could be used to hydrothermal treatment as N-rGO, and NandS-rGO, respectively. Both doping showed the nitrogen species and more sulfur species for NandS-rGO. But monomer doping or

urea or N-rGO showed higher electrode performance than NandS-rGO. There are some reasons, could be attributed such only nitrogen doping showed higher graphitic-N which might be explained by no sulfur as bigger atom to interfere as well as sulfur might also be cause to destroy  $sp^2$  hybridization, implied using  $I_D/I_G$ . There conclude may be implied electrical conductivity and pseudocapacitance are significant parameter than wettability for being a good supercapacitor electrode.

#### 4.4 Violet laser treatment (VLT) on N-rGO

We started this research from graphene oxide (GO) synthesis as electrode for supercapacitor application. Intrinsic properties of graphene oxide were improved by using hydrothermal technique with urea called nitrogen doped reduced graphene oxide (N-rGO). Based on this improvement, the best urea concentration is 40 % w/v called N-rGO40 that was mostly studied in this chapter. After that, VLT treatment is useful to improve surface properties of rGO, N-rGO20, N-rGO40, and N-rGO60 electrodes called rGO-VX, N-rGO20-VX, N-rGO40-VX, and N-rGO60-VX electrodes, respectively (when X is the repeating number of VLT treatment). There is more notice point for normal treatment when we do not identify voltage of violet laser. That mean we use 10.2 V to apply for treatment which is maximum voltage as well as intensity of our violet laser treating machine. To investigate VLT effect on electrode for supercapacitor, all electrodes were further treated by violet laser treatment (VLT) on their electrodes. all electrodes were assembled as symmetric supercapacitor coin cells with using 1 M  $H_2SO_4$  in DI water as electrolyte for evaluating electrochemical performance as shown in Figure 3.6. Finally, almost electrodes were further characterized using scanning electron microscopy (SEM), X-ray diffraction (XRD), Fourier transform infrared spectroscopy

(FT-IR), X-ray photoelectron spectroscopy (XPS), Raman spectroscopy, and contact angle.

Before moving forward to electrochemical properties and characterized parts, we need to explain about division of intrinsic and surface properties that will be mentioned in this thesis. Due to SEM image for cross section view of electrode for N-rGO and N-rGO-V5 region clearly showed the effect of VLT treatment in depth as shown in Figure 4.28. which clearly represented activated surface  $\sim 30 \mu\text{m}$  in depth because of VLT process.

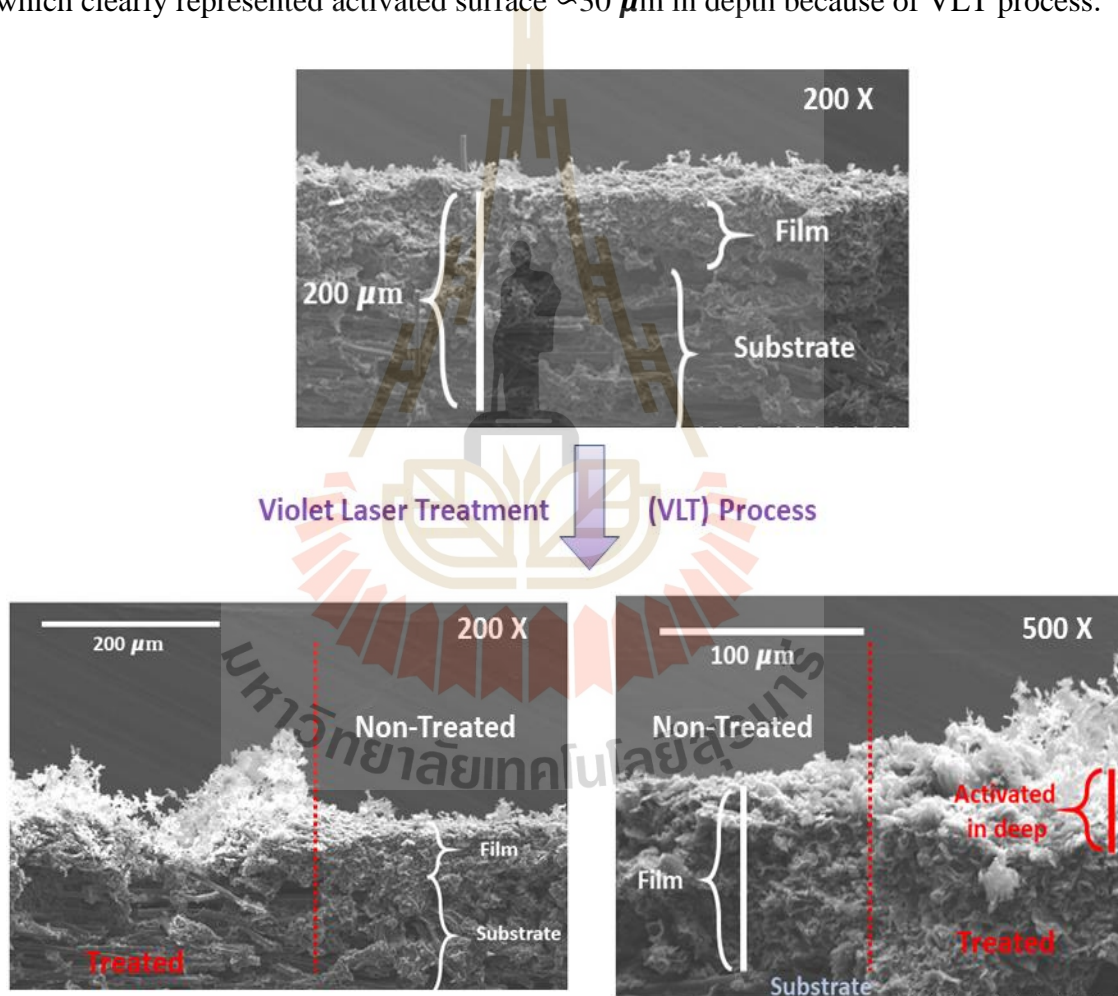


**Figure 4.28** SEM image of cross-section view of electrode for showing interface of N-rGO40 and N-rGO40-V5 region.

#### 4.4.1 Electrochemical properties

After coin cell assembly as symmetric supercapacitors using rGO, rGO-VX, N-rGO20, N-rGO20-VX, N-rGO40, N-rGO40-VX, N-rGO60, and N-rGO60-VX electrode, all coin cells were evaluated electrochemical properties via evaluating using CV and GCD. Coin cell supercapacitors with all electrodes condition were tested with expand operating voltage from 1 V to 1.0 V. CV loops were evaluated with potential scan rate 5, 10, 25, 50, 100, 200, 500  $\text{mV s}^{-1}$ . GCD were measured with constant current 0.125, 0.25, 0.50, 1, 2, 5 and 10  $\text{A g}^{-1}$ . Moreover, CV and GCD can be attributed the behavior in system to show pseudocapacitive signal and electrostatic double layer capacitors (EDLCs). Finally, individual electrodes were further characterized using electrochemical impedance spectroscopy (EIS) to explain the effect to performance enhancement of electrodes which were treated using VLT treatment as shown in following.

##### 4.4.1.1 The specific capacitance of rGO, rGO-V1, rGO-V3, and rGO-V5

###### SCs coin cells

Coin cell supercapacitor with rGO, rGO-V1, rGO-V3 and rGO-V5 electrodes were tested with operating voltage from 1 V to 1.0 V with both CV and GCD showed as shown in Figure 4.29. GCD showed a triangular charge/ discharge curve which discharge time of electrodes with VLT treatment showed longer than non-treated. CVs loops exhibited a quasi-rectangular shape with a pair of small board oxidation that mean mainly electrical double layer capacitive (EDLC) with pseudo-capacitive behavior that may come from quinone group after VLT process. Moreover, CVs graph showed bigger loops when supercapacitors were used VLT electrode. Those mean VLT treatment can enhance capacitive performance of rGO based electrode.

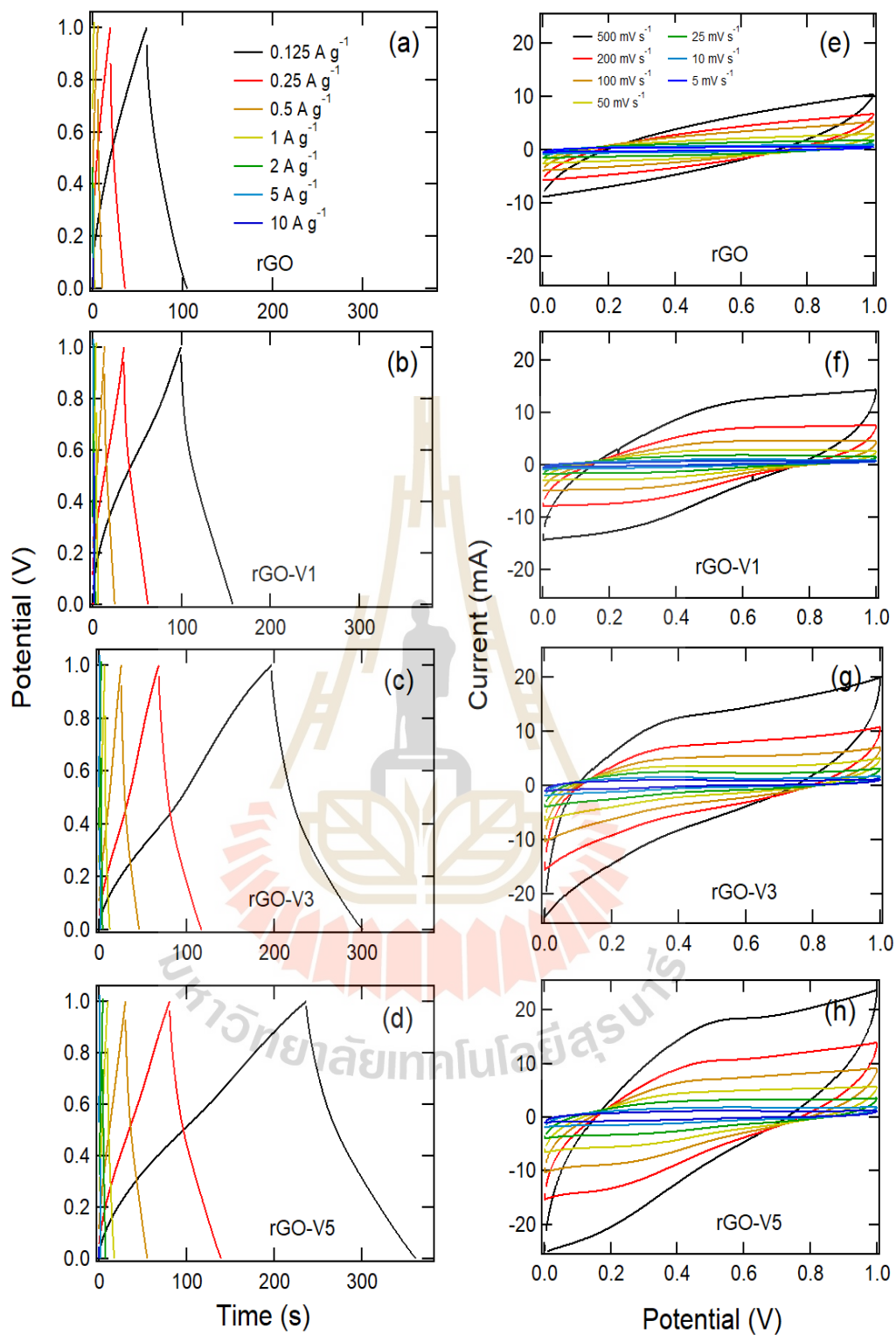


**Figure 4.29** GCD and CV results of rGO, rGO-V1, rGO-V3 and rGO-V5 SCs coin cells.

Figure 4.30 showed trend of the specific capacitance with constant current in GCD and potential scan rate for CV. The trend results showed VLT treatment can clearly improve of performance of supercapacitor via increase EDLCs mechanism as well as a bit increase pseudocapacitance or redox reaction.

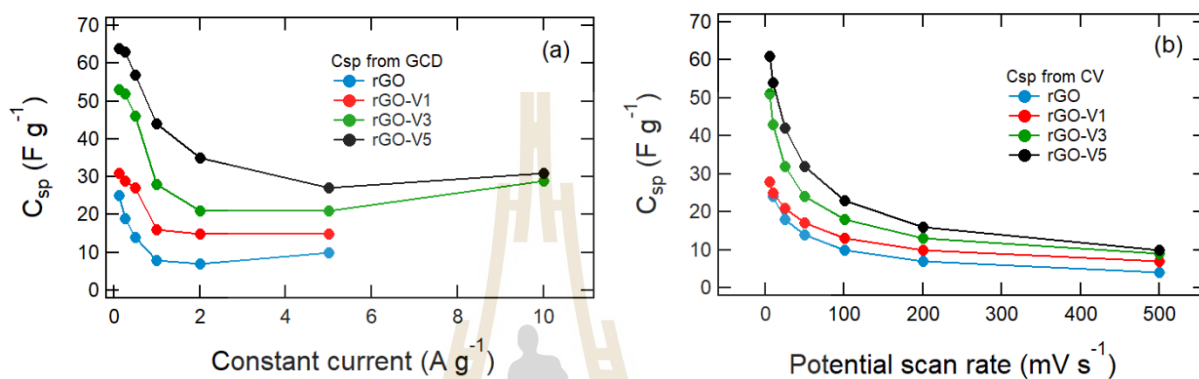


**Figure 4.30** Calculated the specific capacitance from GCD and CV results of rGO, rGO-V1, rGO-V3 and rGO-V5 SCs coin cells.

#### 4.4.1.2 EIS of rGO, rGO-V1, rGO-V3, and rGO-V5 SCs coin cells

The electrochemical behavior at the electrode/electrolyte interface was reported by EIS. The results showed all VLT treatment (1, 3, 5 cycle) can clearly showed decreasing of electrode ( $R_e$ ) and electrode/electrolyte resistance ( $R_e + R_{\Omega}$ ). But charge diffusion showed quite same rate which were interpreted from quite same slope of low frequency region in all EIS results as shown in Figure 4.31 and Table 4.13.

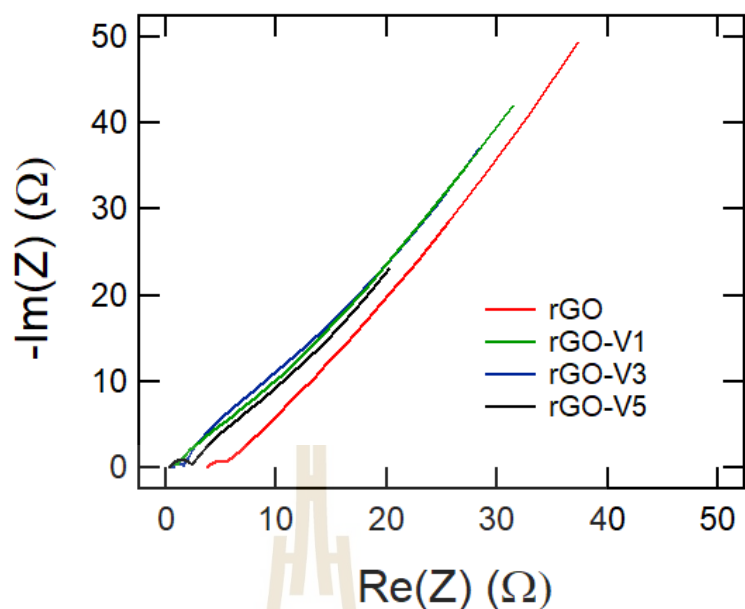


**Figure 4.31** EIS results of rGO, rGO-V1, rGO-V3 and rGO-V5 SCs coin cells.

**Table 4.13** Electrochemical performance results of N-rGO20, N-rGO20-V1, N-rGO20-V3 and N-rGO20-V5 SCs coin cells.

Electrode	GCD		CV		EIS		
	Best $C_{sp}$ ( $F g^{-1}$ )	Position of pseudo-peak (V)	Best $C_{sp}$ ( $F g^{-1}$ )	Position of pseudo-peak (V)	$R_e$	$R_e + R_s$	Slope at $R_D$ region and slope at low $f$
rGO	28	-	25	-	4.6	5.4	rGO $\approx$ rGO-V1 $\approx$
rGO-V1	31	0.3-0.5	28	0.3-0.5	0.4	1.0	rGO-V3 $\approx$ rGO-V5
rGO-V3	53	0.4	51	0.3	0.7	1.8	
rGO-V5	65	0.5	61	0.5	0.4	2.2	

#### 4.4.1.3 The specific capacitance of N-rGO20, N-rGO20-V1, N-rGO20-V3, and N-rGO20-V5 SCs coin cells

Coin cell supercapacitor with N-rGO20, N-rGO20-V1, N-rGO20-V3 and N-rGO20-V5 electrodes were tested with operating voltage from 1 V to 1.0 V with

both CV and GCD showed as shown in Figure 4.32. GCD showed a triangular charge/discharge curve which discharge time of electrodes with VLT process showed longer than non-treated. CVs loops exhibited a quasi-rectangular shape that mean mainly electrical double layer capacitive (EDLC). Moreover, CVs graph showed bigger loops when supercapacitors were used VLT electrode. These GCD and CV results meaned VLT treatment can enhance capacitive performance of N-rGO20 based electrode.

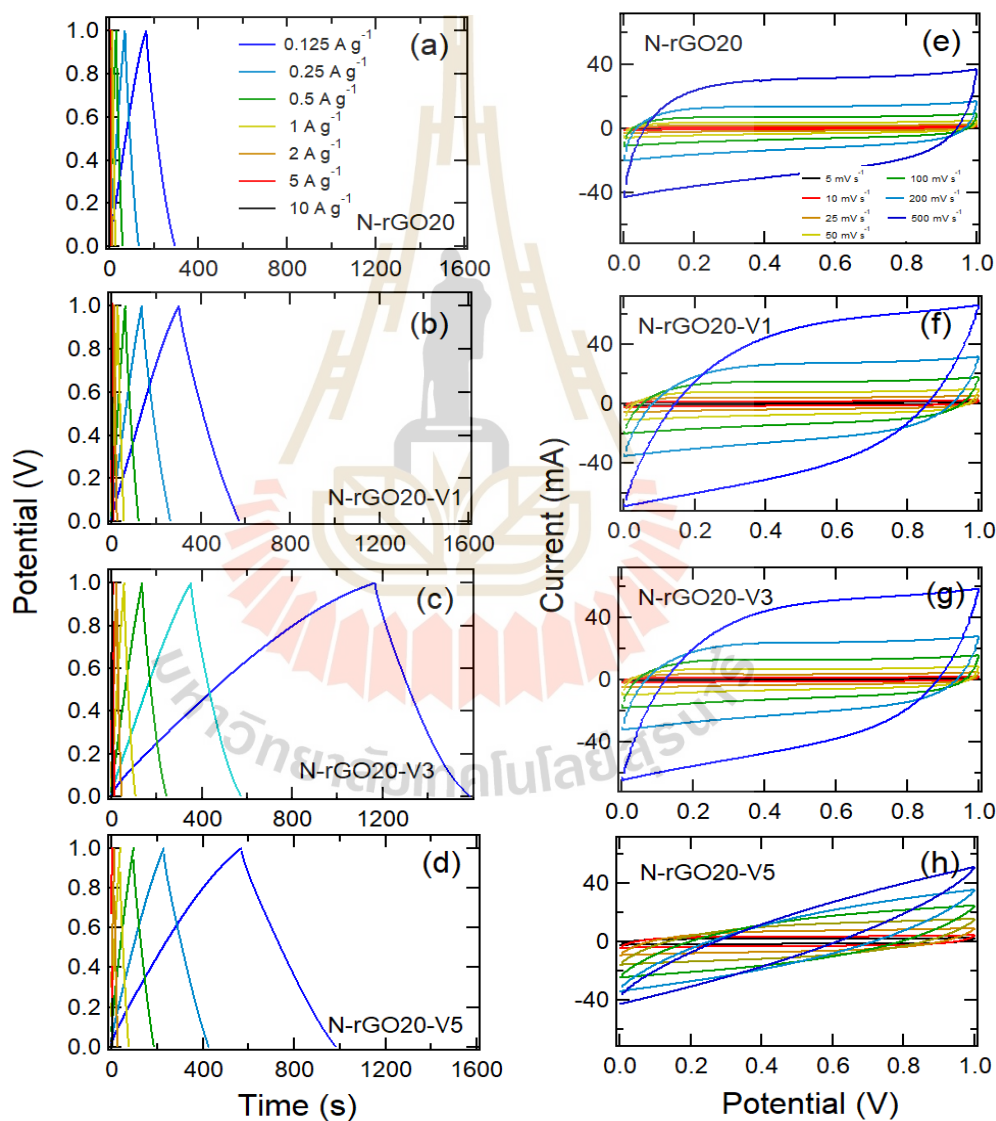


**Figure 4.32** GCD and CV results of N-rGO20, N-rGO20-V1, N-rGO20-V3 and N-rGO20-V5 SCs coin cells.

Subsequently, Figure 4.33 showed trend of the specific capacitance with constant current in GCD and potential scan rate for CV. The trend results showed VLT treatment can clearly improve of performance of supercapacitor via increase EDLCs mechanism. For, N-rGO20-V5 showed pseudocapacitance or redox reaction which is a main factor for higher the Csp.

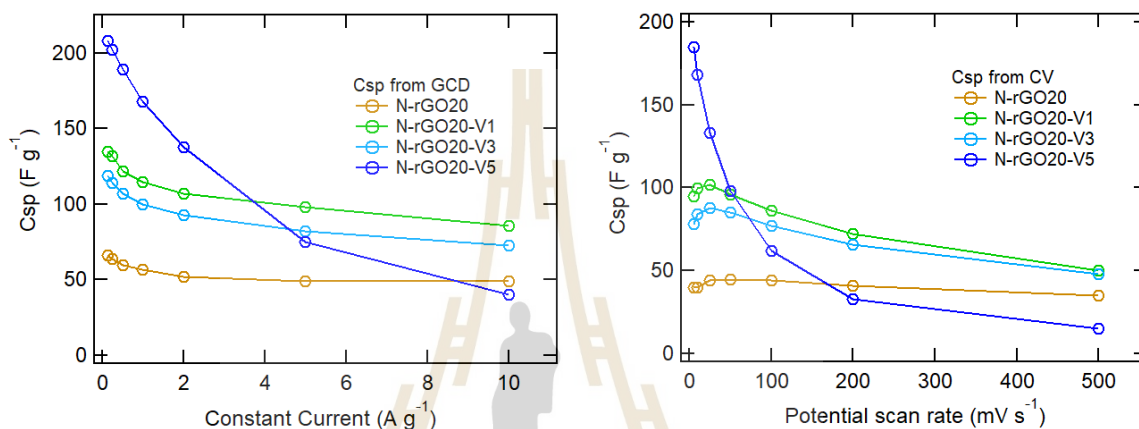


**Figure 4.33** Calculated the specific capacitance from GCD and CV results of N-rGO20, N-rGO20-V1, N-rGO20-V3 and N-rGO20-V5 SCs coin cells.

#### 4.4.1.4 EIS of N-rGO20, N-rGO20-V1, N-rGO20-V3, and N-rGO20-V5

##### SCs coin cells

The electrochemical behavior at the electrode/electrolyte interface was reported by EIS. The results showed all VLT treatment (1, 3, 5 cycle) increased whole coin cell conductivity although showed slight increase electrodes resistance ( $R_e$ ) and electrode/electrolyte resistance ( $R_e + R_{\text{ct}}$ ). Moreover, charge diffusion showed quite high rate for only N-rGO20-V1 SCs coin cell and N-rGO20-V3 SCs coin cell because higher slope at low frequency region than N-rGO20 SCs coin cell as shown in Figure 4.34 and Table 4.14. Unfortunately, there is noticed point for N-rGO-V5 SCs coin cell that may

from spiny coin cell assembly then caused very high electrodes resistance ( $R_e$ ) and electrode/electrolyte resistance ( $R_e + R_{\Omega}$ ).

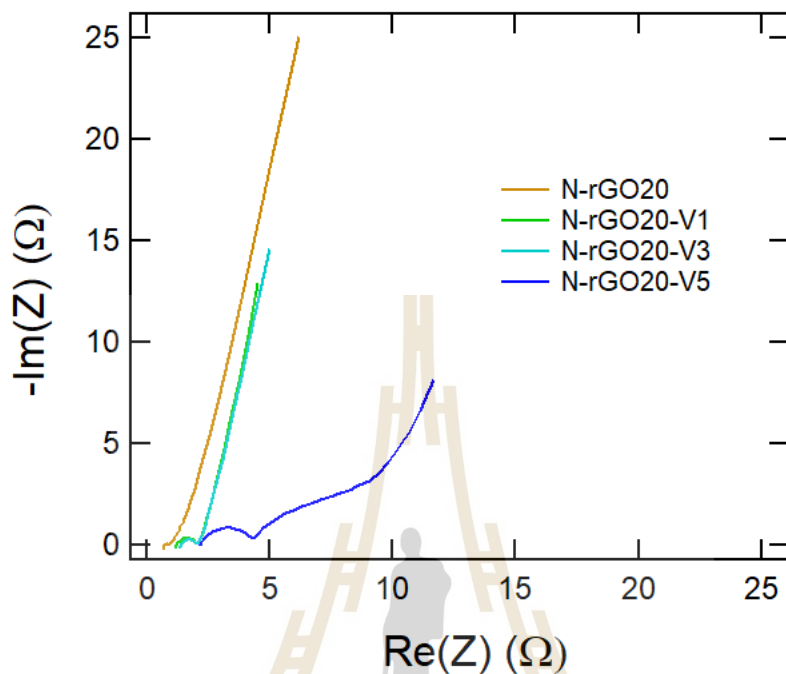


**Figure 4.34** EIS results of N-rGO20, N-rGO20-V1, N-rGO20-V3 and N-rGO20-V5 SCs coin cell.

**Table 4.14** Electrochemical performance results of N-rGO20, N-rGO20-V1, N-rGO20-V3 and N-rGO20-V5 SCs coin cell.

Electrode	GCD		CV		EIS		
	Best $C_{sp}$ ( $F g^{-1}$ )	Position of pseudo- peak (V)	Best $C_{sp}$ ( $F g^{-1}$ )	Position of pseudo- peak (V)	$R_e$	$R_e + R_{\Omega}$	Slope at $R_D$ region and slope at low f
N-rGO20	66	-	45	-	0.7	0.9	N-rGO20-V1 $\approx$ N-
N-rGO20-V1	135	-	102	-	1.2	2.0	rGO-V3 > N-
N-rGO20-V3	119	-	88	-	1.3	2.0	rGO20 > N-
N-rGO20-V5	208	-	185	-	2.2	4.3	rGO20-V5

#### 4.4.1.5 The specific capacitance of N-rGO40, N-rGO40-V1, N-rGO40-V3, and N-rGO40-V5 SCs coin cells.

Coin cell supercapacitor with N-rGO40, N-rGO40-V1, N-rGO40-V3 and N-rGO40-V5 electrodes were tested with operating voltage from 0 V to 1.0 V with both CV and GCD showed as shown in Figure 4.35. GCD showed a triangular charge/discharge curve which discharge time of electrodes with VLT treatment showed longer than non-treated. CVs loops exhibited a quasi-rectangular shape that mean mainly electrical double layer capacitive (EDLC). Moreover, CVs graph showed bigger loops when supercapacitors were used VLT electrode. These results represented VLT treatment induced enhancement of capacitive performance of N-rGO40 based electrode. Moreover, a little bit curve and quasi-rectangular shapes at potential 0.3-0.4 V from GCD curve and CV loop, respectively were disappeared after VLT for all N-rGO40-V1, N-rGO40-V3 and N-rGO40-V5 SCs coin cell which maybe explained using VLT can remove some nitrogen functional groups.

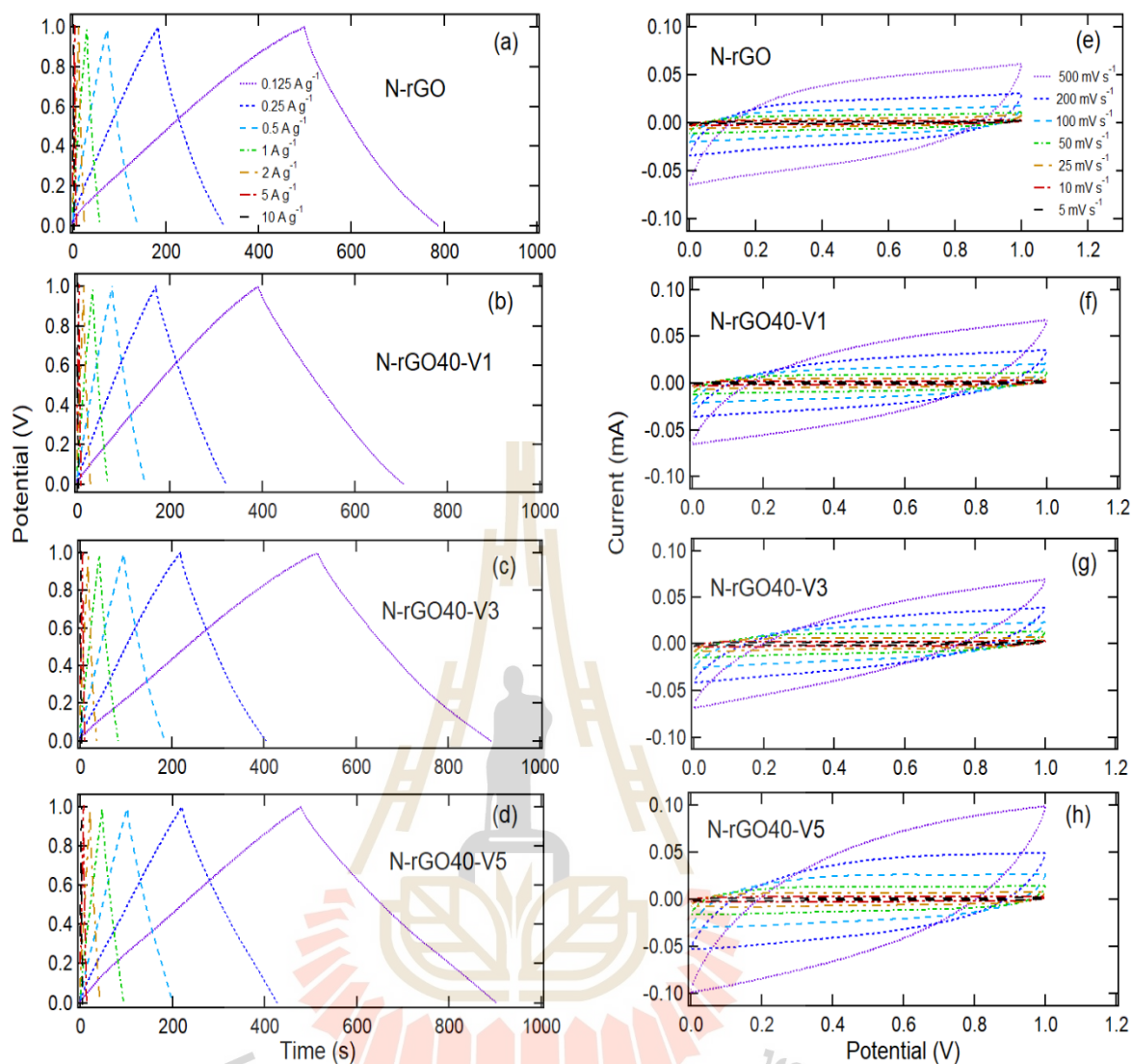


**Figure 4.35** GCD and CV results of N-rGO40, N-rGO40-V1, N-rGO40-V3 and N-rGO40-V5 SCs coin cell.

Figure 4.36 showed trend of the specific capacitance with constant current in GCD and potential scan rate for CV. The trend results showed VLT treatment can clearly improve of performance of supercapacitor via increase EDLCs mechanism as well as pseudocapacitance or redox reaction.

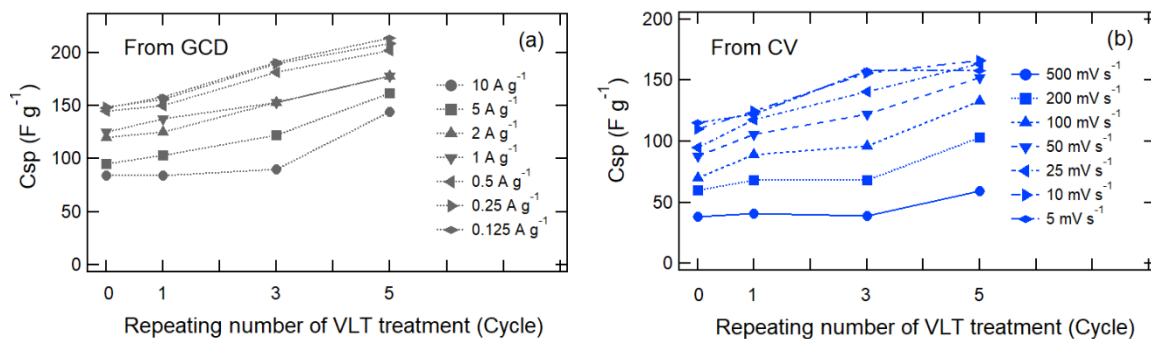


**Figure 4.36** Calculated the specific capacitance from GCD and CV results of results of N-rGO40, N-rGO40-V1, N-rGO40-V3 and N-rGO40-V5 SCs coin cell.

#### 4.4.1.6 EIS of of N-rGO40, N-rGO40-V1, N-rGO40-V3, and N-rGO40-V5 SCs coin cells.

The electrochemical behavior at the electrode/electrolyte interface was reported by EIS. Electrode resistance ( $R_e$ ) of N-rGO40 electrode clearly showed decreasing with both VLT treatment with 3, 5 cycle. Moreover, all 1, 3, 5 cycles of VLT on N-rGO40 showed similar of electrode/electrolyte resistance ( $R_e + R_{\Omega}$ ) but exhibited fasted charge diffusion rate from slope of lower frequency results as shown in Figure 4.37 and Tablr 4.15. But N-rGO40-V1 showed clearly decrease of charge diffusion rate that might be attribute using not enough treating time and intensity.

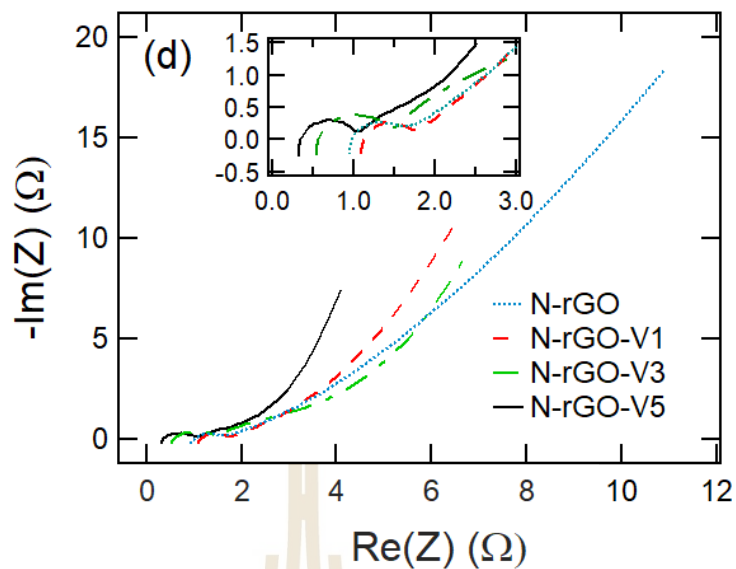


**Figure 4.37** EIS results of N-rGO40, N-rGO40-V1, N-rGO40-V3 and N-rGO40-V5 SCs coin cell.

**Table 4.15** Electrochemical performance results of N-rGO40, N-rGO40-V1, N-rGO40-V3 and N-rGO40-V5 SCs coin cells.

Electrode	GCD		CV		EIS		
	Best $C_{sp}$ ( $F g^{-1}$ )	Position of pseudo- peak (V)	Best $C_{sp}$ ( $F g^{-1}$ )	Position of pseudo-peak (V)	$R_e$	$R_e + R_s$	Slope at $R_D$ region and slope at low f
N-rGO40	145	0.3-0.4	114	0.3-0.5	0.9	1.7	N-rGO40-V5 > N-
N-rGO40-V1	158	-	125	-	1.0	1.7	rGO40-V1 N-rGO40-V3 > N-rGO40
N-rGO40-V3	191	-	158	-	0.5	1.4	
N-rGO40-V5	214	-	166	-	0.3	1.0	

#### **4.4.1.7 The specific capacitance of N-rGO40, N-rGO40-V3-3V, N-rGO40-V3-7V, and N-rGO40-V3-10.2V SCs coin cells.**

Moreover, N-rGO40 were further treated using VLT process with varies intensity of violet laser via changing applied voltage for 0 V (N-rGO40 or non-treated), 3 V, 7 V, and 10.2 V (maximum applied voltage), called N-rGO40-V3-3V, N-rGO40-V3-7V, and N-rGO40-V3-10.2V electrodes were tested with operating voltage from 1 V to 1.0 V with both CV and GCD showed as shown in Figure 4.38. GCD showed a triangular charge/ discharge curve which discharge time of electrodes with VLT treatment showed longer than non-treated. CVs loops exhibited a quasi-rectangular shape with a pair of small board oxidation that mean mainly electrical double layer capacitive (EDLC) with pseudo-capacitive behavior in N-rGO40. Moreover, CVs graph showed bigger loops when supercapacitors were used VLT electrode. Those mean VLT treatment can enhance capacitive performance of N-rGO40 based electrode when approach enough laser intensity or applying voltage more than 3 volt.

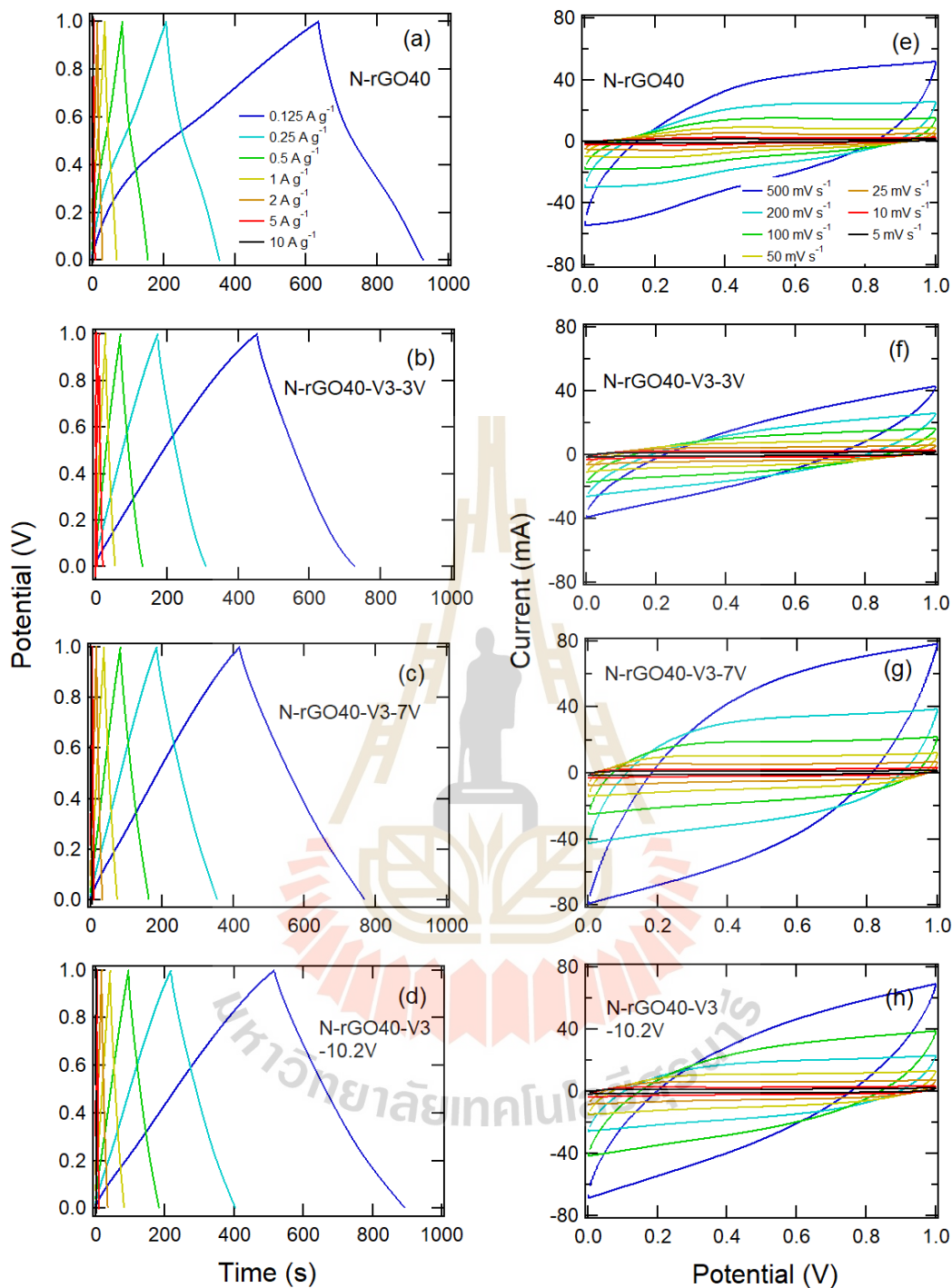


**Figure 4.38** GCD and CV results of N-rGO40, N-rGO40-V3-3V, N-rGO40-V3-7V and N-rGO40-V3-10.2V SCs coin cells.

Figure 4.39 showed trend of the specific capacitance with constant current in GCD and potential scan rate for CV. The trend results showed VLT treatment

can clearly improve of performance of supercapacitor via increase EDLCs mechanism as well as pseudocapacitance or redox reaction.

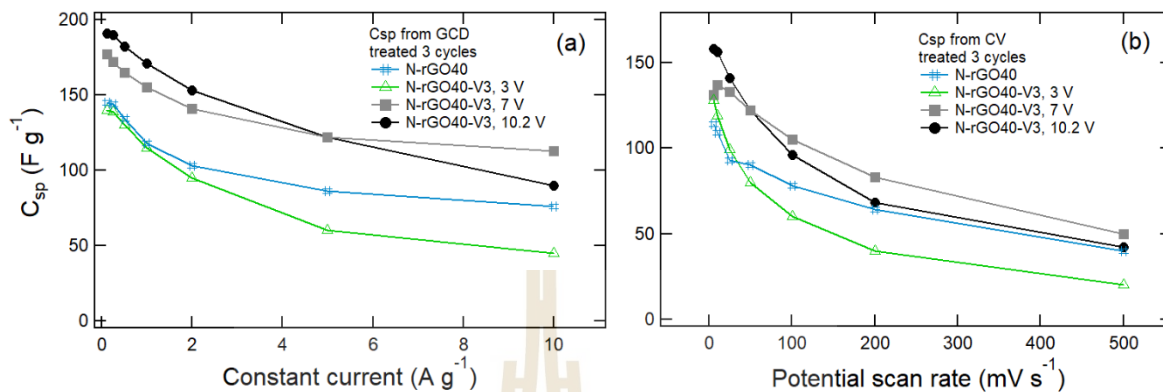


**Figure 4.39** Calculated the specific capacitance from GCD and CV results of N-rGO40, N-rGO40-V3-3V, N-rGO40-V3-7V and N-rGO40-V3-10.2V SCs coin cells.

#### 4.4.1.8 EIS of N-rGO40, N-rGO40-V3-3V, N-rGO40-V3-7V, and N-rGO40-V3-10.2V SCs coin cells.

The electrochemical behavior at the electrode/electrolyte interface was reported by EIS, showed all VLT treatment 3 cycle and more cycles with using applied voltage more than 7 volt. These mentioned conditions showed achievement of the decreasing for electrode resistance and electrode /electrolyte resistance and increase charge diffusion rate as shown in Figure 4.40 and Table 4.16. For -rGO40-V3, 3V, the difference of EIS feature showed lower N slope for  $R_D$  region that can be explained by higher diffusion resistance.

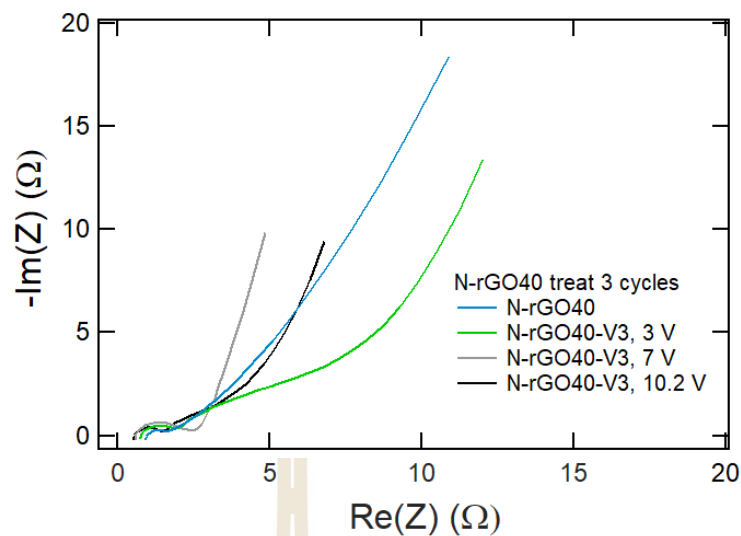


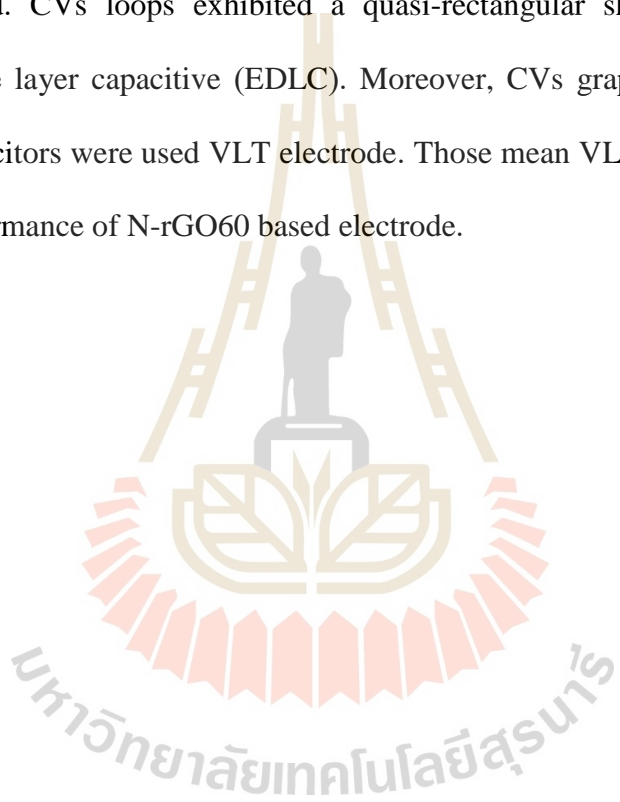
**Figure 4.40** EIS of N-rGO40, N-rGO40-V3-3V, N-rGO40-V3-7V and N-rGO40-V3-10.2V SCs coin cell.

**Table 4.16** Electrochemical performance results of N-rGO40, N-rGO40-V3 with varies intensity via applied voltage as 3, 7, and 10.2 V SCs coin cells.

Electrode	GCD		CV		EIS		
	Best $C_{sp}$ ( $F g^{-1}$ )	Position of pseudo-peak (V)	Best $C_{sp}$ ( $F g^{-1}$ )	Position of pseudo-peak (V)	$R_e$	$R_e + R_s$	Slope at $R_D$ region and slope at low f
N-rGO40	145	0.3-0.4	114	0.3-0.5	0.9	1.7	N-rGO40-V3, 7V > N-rGO40-V3, 10.2V > N-rGO40-V3, 3V > N-rGO40
N-rGO40-V3, 3V	140	-	128	-	0.7	1.7	
N-rGO40-V3, 7V	177	-	137	-	0.5	2.4	
N-rGO40-V3, 10.2V	191	-	158	-	0.5	1.4	

#### **4.4.1.9 The specific capacitance of N-rGO60, N-rGO60-V1, N-rGO60-V3, and N-rGO60-V5 SCs coin cells**

Coin cell supercapacitor with N-rGO60, N-rGO60-V1, N-rGO60-V3 and N-rGO60-V5 electrodes were tested with operating voltage from 1 V to 1.0 V with both CV and GCD showed as shown in Figure 4.41. GCD showed a triangular charge/discharge curve which discharge time of electrodes with VLT treatment showed longer than non-treated. CVs loops exhibited a quasi-rectangular shape that mean mainly electrical double layer capacitive (EDLC). Moreover, CVs graph showed bigger loops when supercapacitors were used VLT electrode. Those mean VLT treatment can enhance capacitive performance of N-rGO60 based electrode.



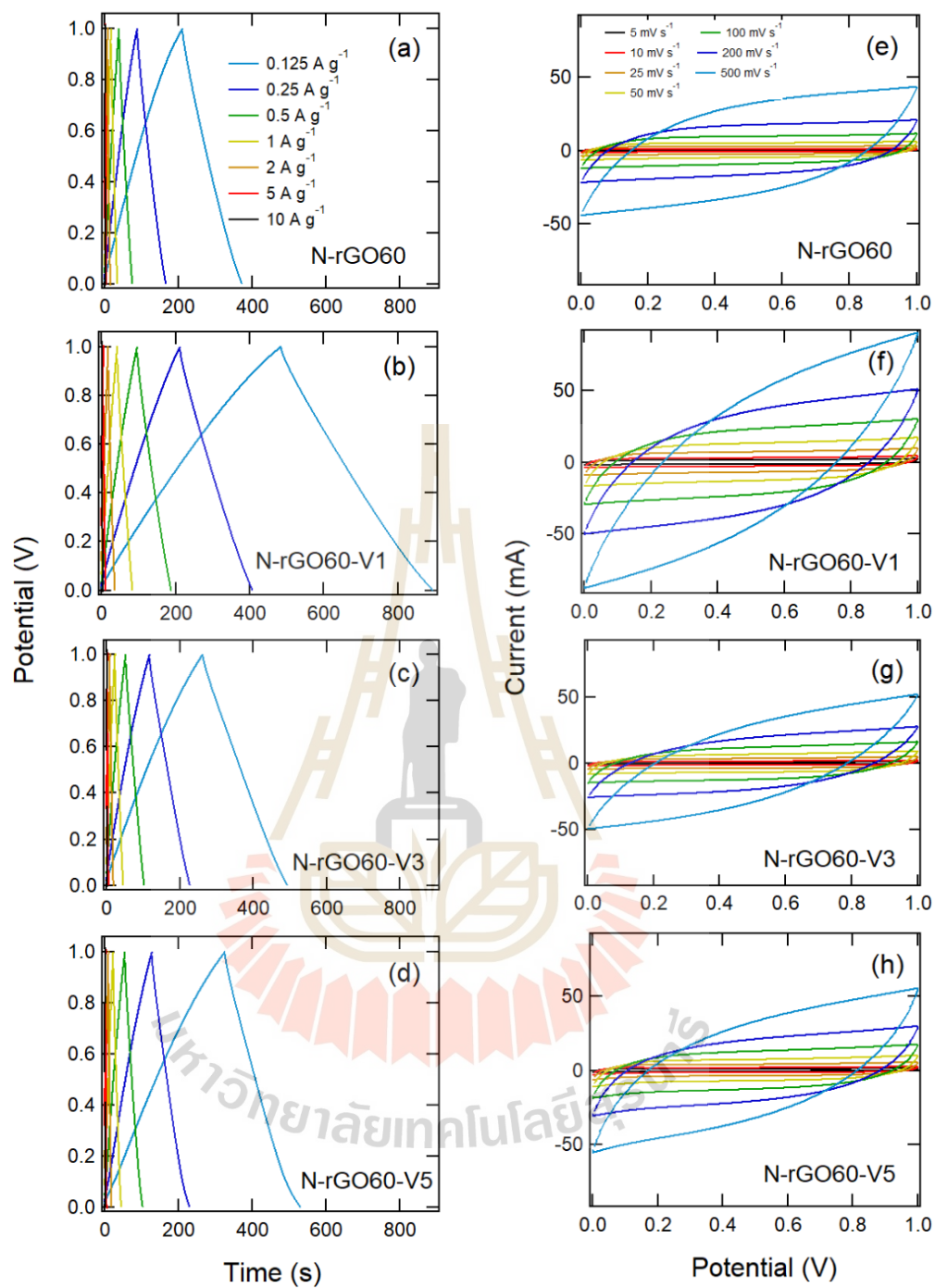


**Figure 4.41** GCD and CV results of N-rGO60, N-rGO60-V1, N-rGO60-V3 and N-rGO60-V5 SCs coin cells.

Figure 4.42 showed trend of the specific capacitance with constant current in GCD and potential scan rate for CV. The trend results showed VLT treatment can clearly improve of performance of supercapacitor via increase EDLCs.

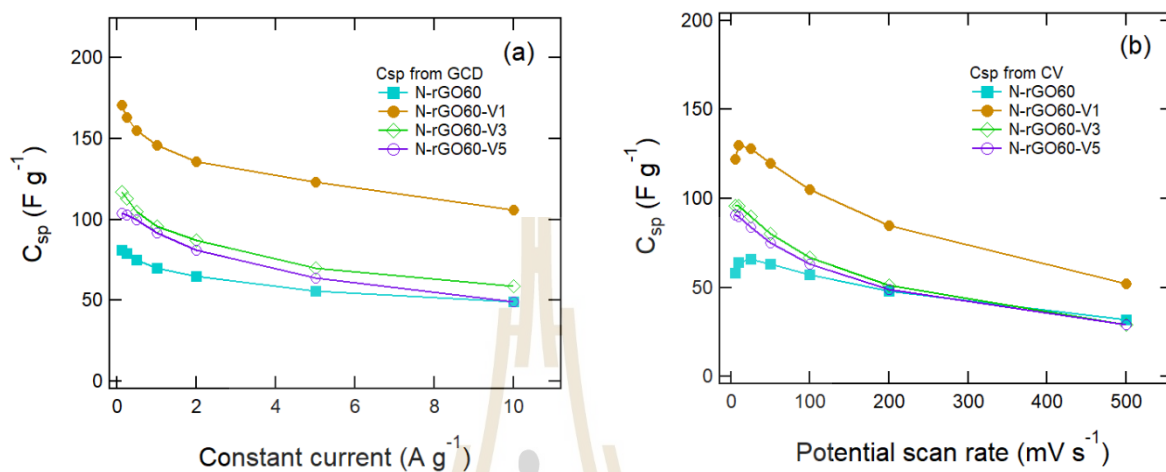


**Figure 4.42** Calculated the specific capacitance from GCD and CV results of N-rGO60, N-rGO60-V1, N-rGO60-V3 and N-rGO60-V5 SCs coin cell.

#### 4.4.1.10 EIS of N-rGO60, N-rGO60-V1, N-rGO60-V3, and N-rGO60-V5

##### SCs coin cells

The electrochemical behavior at the electrode/electrolyte interface was reported by EIS, All N-rGO60 with VLT (1, 3, 5 cycle) can decrease electrode resistance ( $R_e$ ) and electrode/electrolyte resistance ( $R_e + R_{\text{dl}}$ ) although charge diffusion showed quite same rate for non-treat SCs coin cell as shown in Figure 4.43 and Table 4.17.

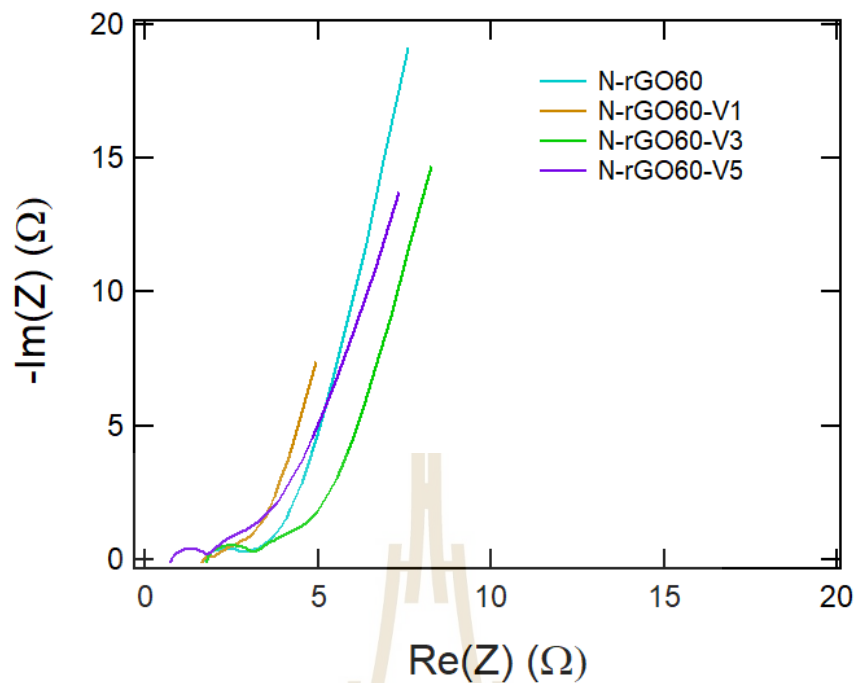


**Figure 4.43** EIS results of N-rGO60, N-rGO60-V1, N-rGO60-V3 and N-rGO60-V5 SCs coin cells.

**Table 4.17** Electrochemical performance results of N-rGO60, N-rGO60-V1, N-rGO60-V3 and N-rGO60-V5 SCs coin cells.

Electrode	GCD		CV		$R_e$	$R_{e+}$	Slope at $R_D$ region and slope at low $f$
	Best $C_{sp}$ ( $F\ g^{-1}$ )	Position of pseudo-peak (V)	Best $C_{sp}$ ( $F\ g^{-1}$ )	Position of pseudo-peak (V)			
N-rGO60	81	-	66	-	1.8	2.9	N-rGO60-V3 $\approx$ N-rGO60-V1 $\approx$ N-rGO60-V5
N-rGO60-V1	171	-	130	-	1.7	1.9	
N-rGO60-V3	117	-	96	-	1.7	3.1	
N-rGO60-V5	104	-	91	-	0.8	1.8	

To study influence of treatment time for violet light laser, Table 4.18 showed comparative results of N-rGO40, N-rGO40-V3-3V, N-rGO40-V3-7V and N-rGO40-V3-10.2V SCs coin cells. These results showed the using VLT technique to enhance performance of SCs electrode. Enough treatment time or repeating cycle of VLT must higher than 3 cycles.

**Table 4.18** The operating voltage, charging and discharging time, specific capacitances, energy densities and power densities of SCs using rGO, rGO-VX, N-rGOY and N-rGOY-VX SCs coin cells in 1 M H<sub>2</sub>SO<sub>4</sub> at 0.125 A g<sup>-1</sup>.

Electrode-(treated step with 10.2 V)	$\Delta V$ (V)	$\Delta t_{\text{discharge}}$ (s)	$C_{\text{sp}}$ (F g <sup>-1</sup> )	E (W h kg <sup>-1</sup> )	P (W kg <sup>-1</sup> )
rGO	0.93	45	24.2	0.7	58.1
rGO-V1	0.97	58.2	30	1.0	60.6
rGO-V3	0.98	104	53.1	1.8	61.3
rGO-V5	0.98	126	64.3	2.1	61.3
N-rGO20	0.99	129	65.2	2.2	61.8
N-rGO20-V1	0.99	268	134.7	4.6	62.2
N-rGO20-V3	0.99	237	119.1	4.1	62.2
N-rGO20-V5	0.99	413	208.6	7.1	61.9
N-rGO40	0.99	294	149	5.1	61.9
N-rGO40-V1	0.99	423	214	7.3	61.9
N-rGO40-V3	0.99	377	190.5	6.5	61.9
N-rGO40-V5	0.99	313	158.1	5.4	61.9
N-rGO60	0.99	161	81.3	2.8	61.9
N-rGO60-V1	0.99	340	170.9	5.9	62.2
N-rGO60-V3	0.99	230	116.2	4.0	61.9
N-rGO60-V5	0.99	201	102	3.5	61.9

Moreover, to study influence of intensity of violet light laser, Table 4.19 showed comparative results of N-rGO40, N-rGO40-V3-3V, N-rGO40-V3-7V and N- N-rGO40-V3-10.2V SCs coin cells. These results showed the using VLT technique to enhance performance of SCs electrode. Enough intensity of violet laserlight must also more than applying voltage for 7 V (approximate > 500 mW from forecast)

**Table 4.19** The operating voltage, charging and discharging time, specific capacitances, energy densities and power densities of SCs using N-rGO40 and varies laser intensity with 3 treated cycles in 1 M H<sub>2</sub>SO<sub>4</sub> at 0.125 A g<sup>-1</sup>.

N-rGO40 Electrode	$\Delta V$ (V)	$\Delta t_{\text{discharge}}$ (s)	$C_{\text{sp}}$ (F g <sup>-1</sup> )	E (W h kg <sup>-1</sup> )	P (W kg <sup>-1</sup> )
Non treat	0.99	294	149	5.1	61.9
3 V	0.99	274	138	4.7	61.7
7 V	0.99	351	177.5	6.0	61.9
10.2 V	0.99	377	190.5	6.5	61.9

#### 4.4.1.11 Capacitive retention of N-rGO40 and N-rGO40-V5 SCs coin cells.

To show long term stabilities of a coin cell supercapacitors, only rGO and N-rGO40 cells were tested capacitive retention with GCD at 1 A g<sup>-1</sup> for 10,000 cycles. Subsequently, the specific capacitance and percentage of capacitive retention of N-rGO40 SCs coin cell was a bit greater than that of N-rGO40-V5 SCs coin cell after 10,000 charge-discharge cycles as shown in Figure 4.44. That can imply VLT treatment, do not have significant on life cycle for supercapacitor electrode. Unfortunately, we have available cells for testing only N-rGO40, and N-rGO40-V5 coin cell supercapacitor.

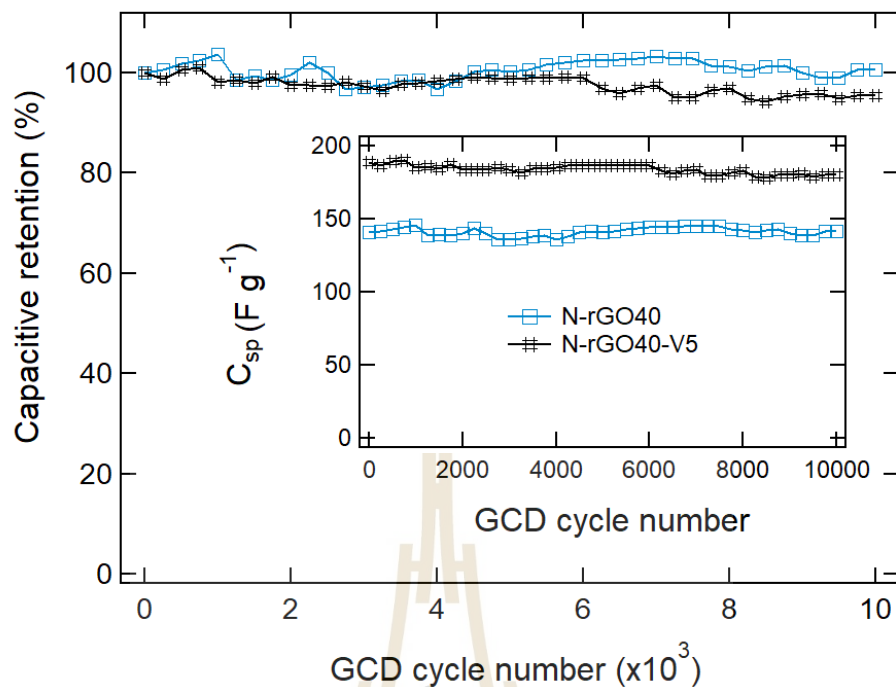


**Figure 4.44** Percentage and the specific capacitance of capacitive retentions of rGO and N-rGO40 SCs coin cells.

#### 4.4.1.12 Leakage current of some N-rGOY-X SCs coin cells

Moreover, violet laser treatment (VLT) treatment on graphene oxide-based electrode can obviously help the decreasing of leakage current and self-discharge, compare with non-treated (rGO and N-rGO40 as well as N-rGO20) as shown in Figure 4.45. Unfortunately, we have available cells for testing only rGO, rGO-V5, N-rGO20, N-rGO40, N-rGO40-V1, N-rGO40-V3, and N-rGO40-V5 coin cell supercapacitor.

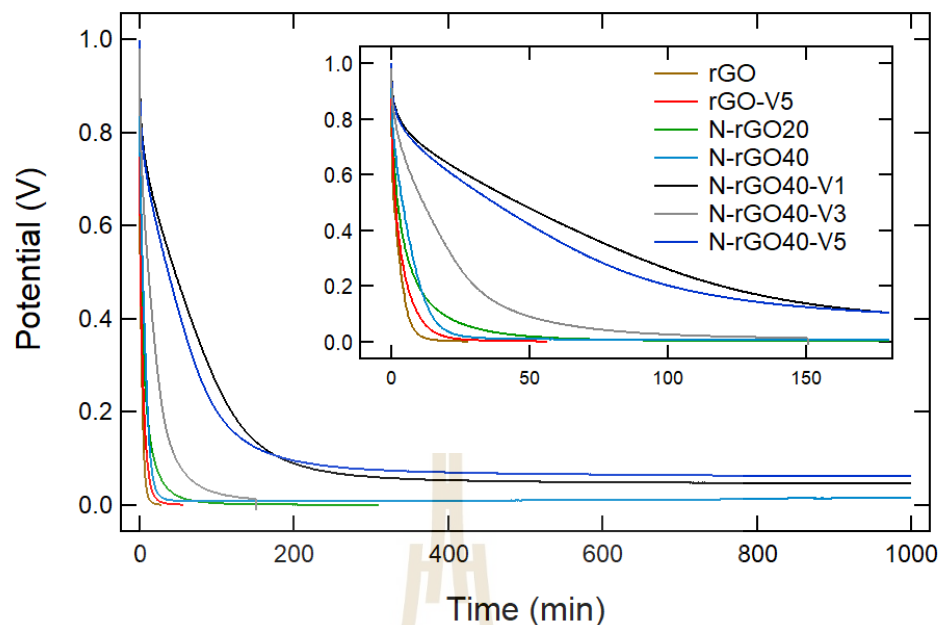


**Figure 4.45** Leakage current of some N-rGOY-VX coin cells

These electrochemical performances showed suitable condition for VLT treatment on rGO and N-rGOY electrode. These are intensity of violet laser should in range of applying 7 – 10.2 V (our experiment cannot provide for higher voltage) and the increase of repeating number of VLT treatment effect to improve electrochemical performance via 3 cycles and showed highest at 5 cycles of treatment which is clearly implied the best condition. Moreover, there are some not clear factors about 1 cycle of treatment that mean for obvious improving then we should use suitable repeating number of VLT treatment as well.

#### 4.4.2 Characterization of rGO, rGO-VX, N-rGOY and N-rGOY-VX electrodes

##### 4.4.2.1 Scanning electron microscopy

To clearly show surface transformation, Figure 4.46 (a) - (e) shows SEM images of the changing of surface morphologies of N-rGO before and after irradiation by

violet laser with the different number of VLT treatments. Figure 4.46 (a)-(h) are the top-view images taken from the N-rGO40 and N-rGO40-VX electrode ( $X = 1, 3, \text{ and } 5$ ), respectively. All N-rGO-based samples exhibited the wrinkly surface of graphene with many nanoparticles' distribution on their surface, while the rGO showed a smoother surface without some nano sizes, as shown in Figure 4.12 (a). The surfaces of N-rGO40 electrode were more roughness than rGO electrode owing to a hydrothermal method with urea. The N-rGO samples are expected to exhibit better electrochemical properties compared to the rGO sample. Therefore, N-rGO electrode was chosen for VLT treatment. It was also found that the surface of the N-rGO samples became more roughness and exfoliation when the number of the repeating cycle of VLT increased. More interesting results were observed in the higher magnification SEM images as shown in Figure 4.46 (d), (f), (h). The bright spots appeared on the sample surface after VLT, and their size was enlarged by the laser fluence or the repeating cycle of VLT. Moreover, Figure 4.46 (i), and (j) showed interface view of electrode where between of N-rGO40 and N-rGO40-V5 region that clearly exhibited exfoliated surface after VLT.

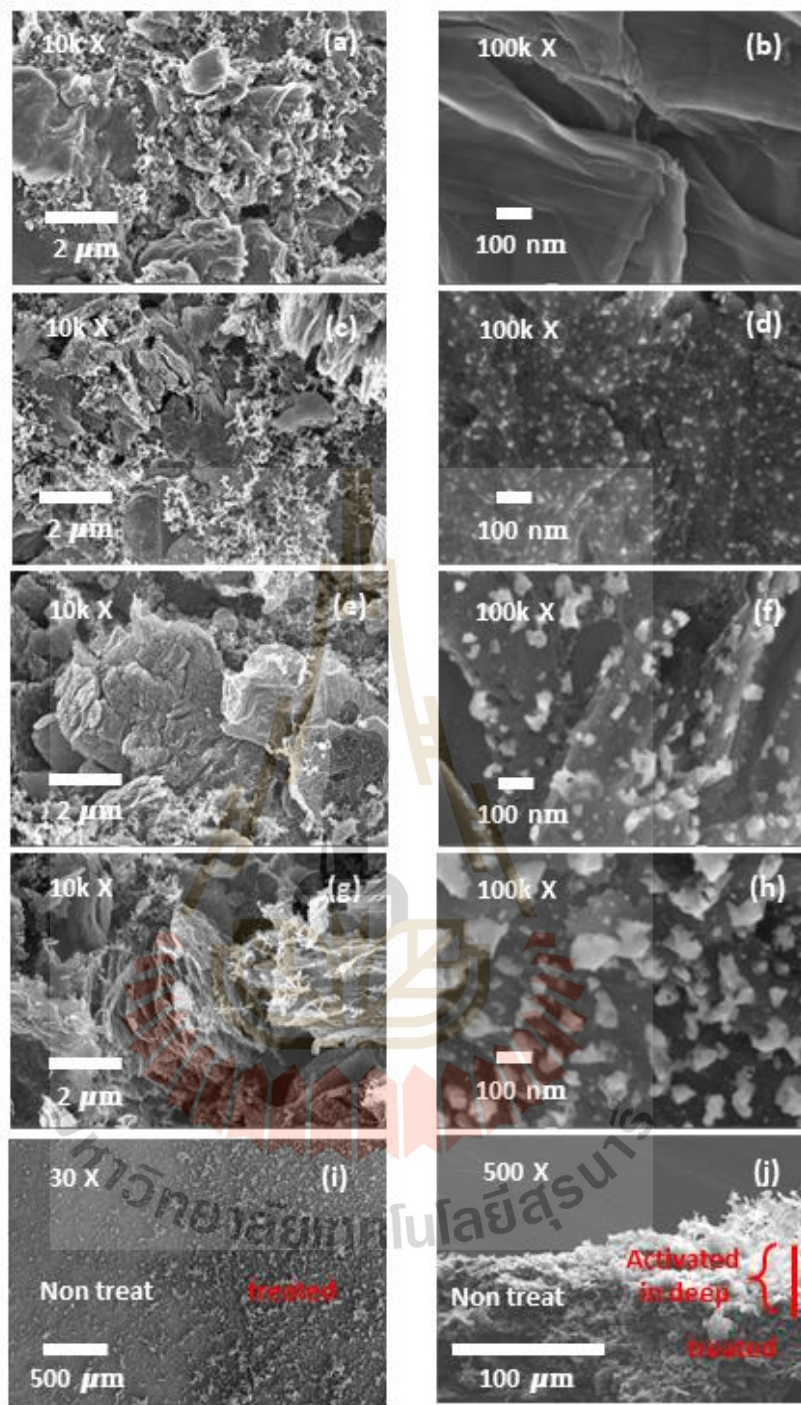


**Figure 4.46** SEM images of N-rGO40 (a) (b), N-rGO40-V1 (c) (d), N-rGO40-V3 (e) (f) and N-rGO40-V5 (g) (h) electrode, Top view of interface between N-rGO40 and N-rGO40-V5 (i) electrode, and side view of interface of electrode for showing the difference between of N-rGO40 and N-rGO40-V5 region (j).

#### 4.4.2.2 X-ray diffraction (XRD)

According to previous XRD in chapter V already identified diffraction plan. Here, we need to show importance evidence for supporting exfoliated surface and higher porosity of electrode after VLT treatment as shown in Figure 4.47. This is plan peak shift to lower  $2\theta$  which can be attributed using Bragg's law to imply increasing of d-spacing (S.-Y. Lee and Park, 2014) (Nguyen and Baird, 2007). Moreover, higher counts of each peak also showed more plan or state in same plan peak after VLT treatment. There are obviously peak via (002), (103), and (220), corresponding to graphitic plan, carbon black, respectively which showed as above explanation.

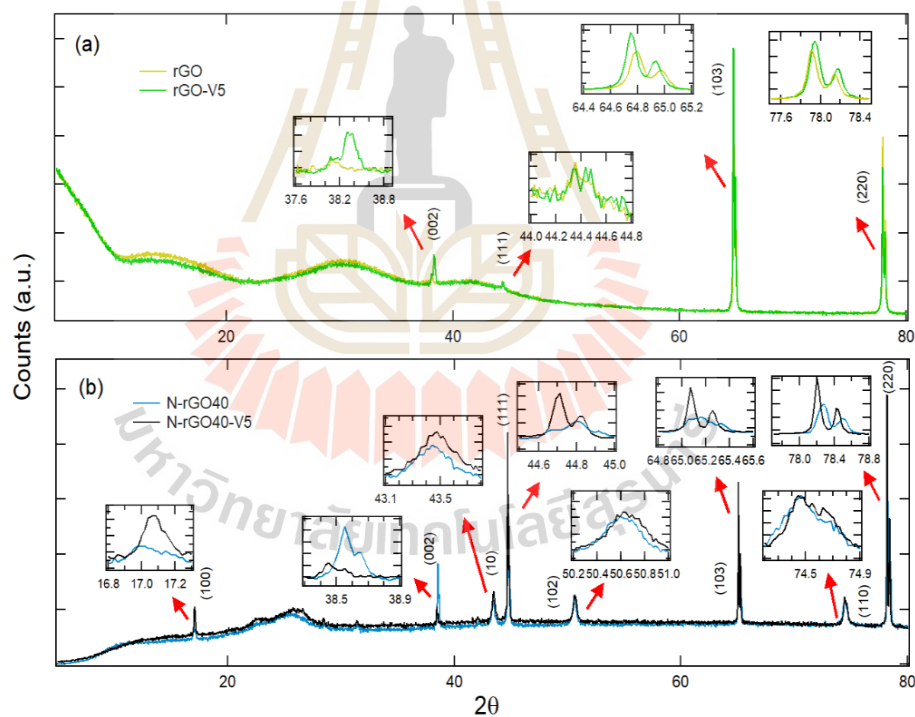


**Figure 4.47** XRD results of comparative result of rGO, rGO-V5 electrode (a), and N-rGO40, N-rGO40-V5 electrode (b).

#### 4.4.2.3 X-ray photoelectron spectroscopy

To overall observation of chemical composition changing, X-ray photoelectron spectroscopy (XPS) were performed to investigate chemical compositions on rGO, rGO-V5, all N-rGOY, and all N-rGOY-V5 electrodes. Wide scans of these electrodes were recorded in the binding energies range from 0 to 550 eV which included carbon, oxygen on all electrodes and a little nitrogen peak on N-rGO20, N-rGO40 and N-rGO60 electrode as shown in Figure 4.48 (a)- Figure 4.51 (a). These spectra showed decrease of O1s peak intensity with increasing of C1s peak intensity after VLT treatment which can implied the removing of oxygen functional group on electrode surface.

To analysis surface chemical compositions, the high resolution XPS spectra of C1s signal of rGO, rGO-V5, all N-rGOY, and all N-rGOY-V5 electrodes are displayed in Figure 4.48 (b), (c) – Figure 4.51 (b), (c). The XPS spectrum of C1s comprised C=C ( $sp^2$ ), C-O/C-N, C=O/C=N, COOH, CHF, and C-F at binding energies of 284.5, 285.3, 286.8, 288.4, 289.2 and 292 eV, respectively (Zhuo et al., 2015) (K. H. An et al., 2002) (Biniak et al., 1997) (Kelemen and Kwiatek, 1995). These spectra showed increasing intensity peak of C=C ( $sp^2$ ) with decrease of other peaks and related with relative C=C ( $sp^2$ ) ratio as shown in Table 4.20.

To check oxygen species, the signal of O1s of all electrodes are shown oxygen-containing functional groups such as C=O, C-OH/C-O-C, and COOH/water at binding energies of 531.5, 533.0, 534.5 eV, respectively (Zielke et al., 1996) (Lorenc-Grabowska et al., 2013) as shown in Figure 4.48 (d), (e)- 4.51 (d), (e). These spectra showed VLT treatment, might not significantly affect to species of oxygen because ratio peaks of each bonding are quite same as shown in Table 4.21.

Moreover, N1s peak of all electrodes, revealed nitrogen-containing functional groups such pyridinic-N, pyrrolic-N, and quaternary-N at binding energies of 398.0, 400.0 and 402.0 eV, respectively (Kapteijn et al., 1999) (Lorenc-Grabowska et al., 2013) (Śliwak et al., 2017) as shown in Figure 4.48 (f), (g)- 4.51 (f), (g). These spectra showed VLT treatment, mainly effect to remove pyridinic-N, pyrrolic-N but quaternary-N is quite same amount when amount of N species calculated ratio with quaternary-N as shown in Table 4.22.

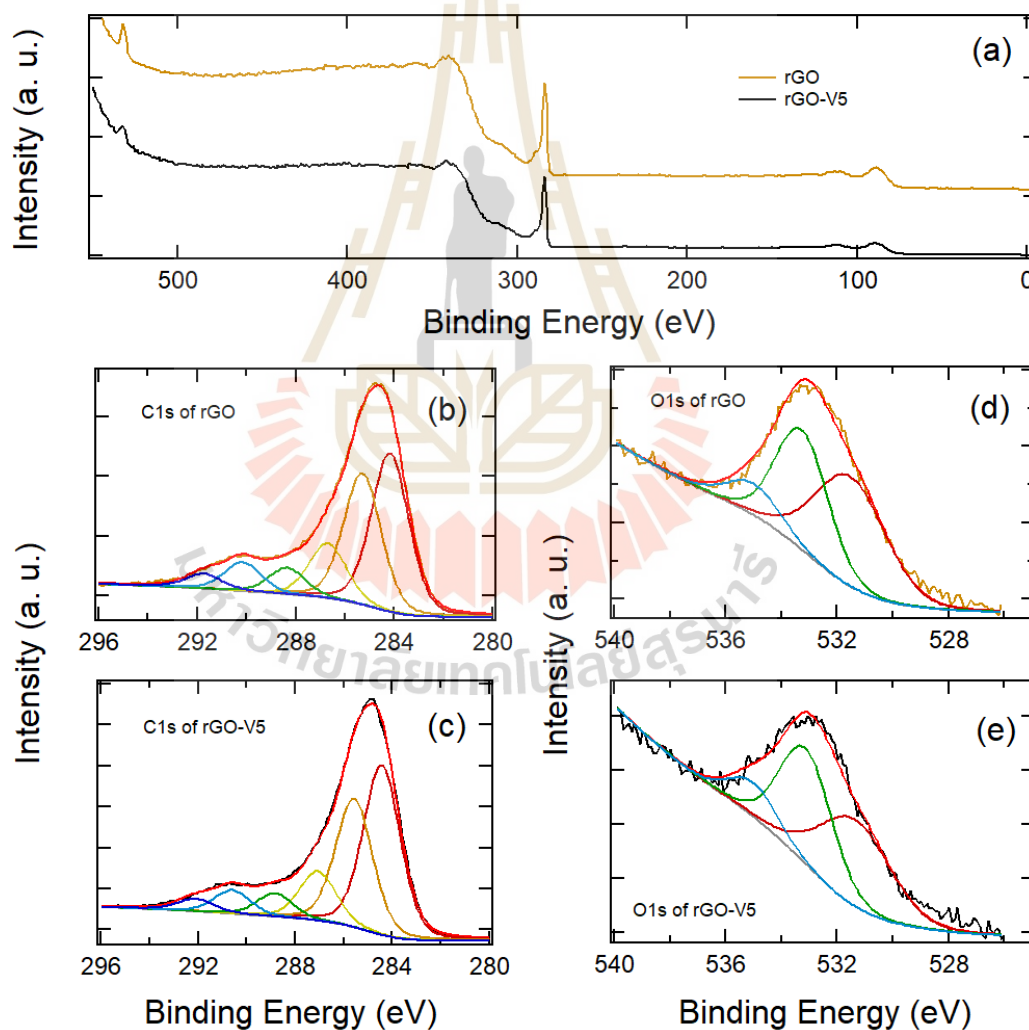


**Figure 4.48** Wide scan rGO and rGO-V5 (a), C1s of rGO (b), C1s of rGO-V5 (c), O1s of rGO (d), and O1s of rGO-V5 (e) electrodes.

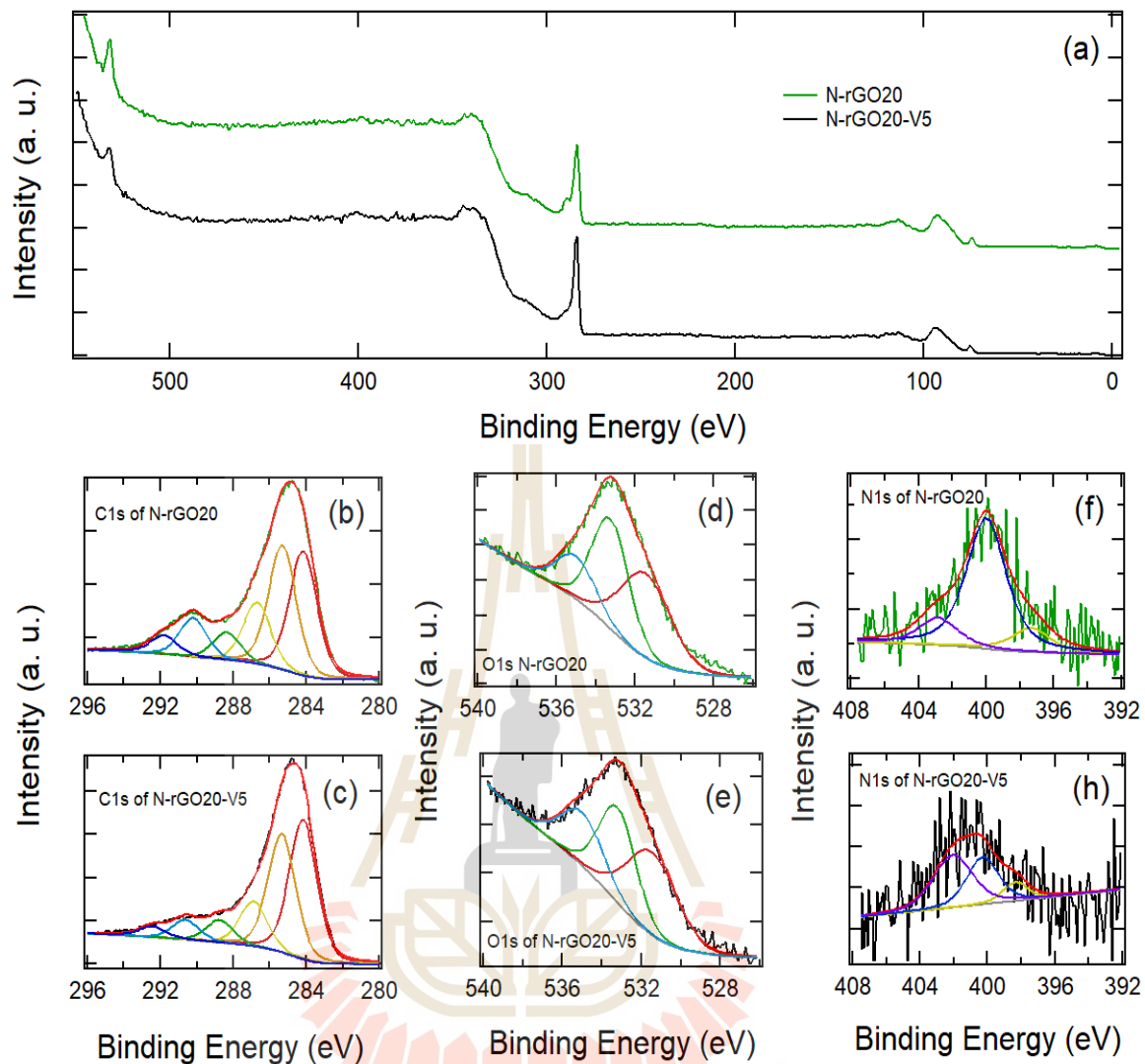


**Figure 4.49** Wide scan N-rGO20 and N-rGO20-V5 (a), C1s of N-rGO20 (b), C1s of N-rGO20 -V5 (c), O1s of N-rGO20 (d), O1s of N-rGO20 -V5 (e), N1s of N-rGO20 (f), N1s of N-rGO20 -V5 (g) electrodes.

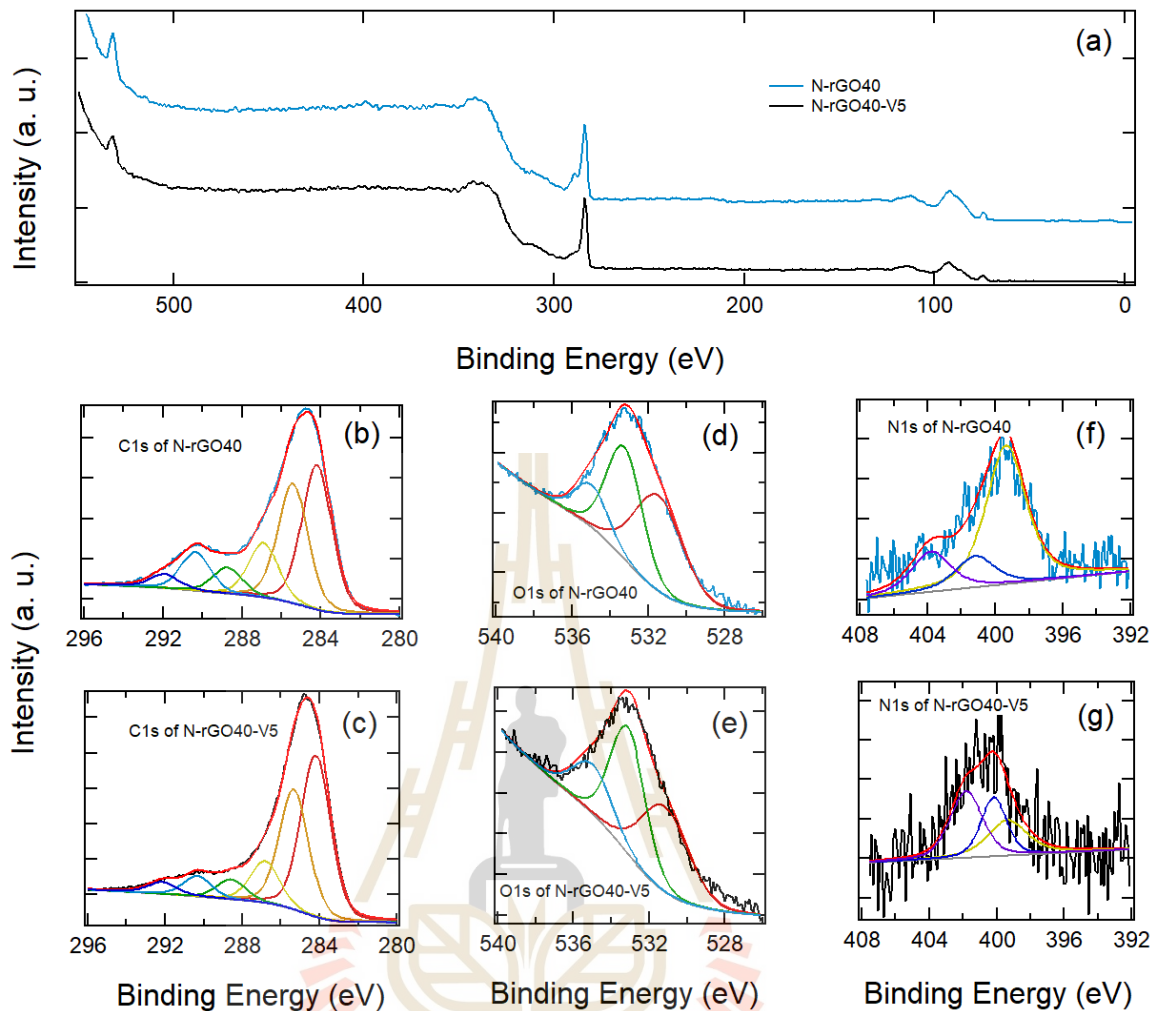


**Figure 4.50** Wide scan N-rGO40 and N-rGO40-V5 (a), C1s of N-rGO40 (b), C1s of N-rGO40-V5 (c), O1s of N-rGO40 (d), O1s of N-rGO40-V5 (e), N1s of N-rGO40 (f), N1s of N-rGO40-V5 (g) electrodes.

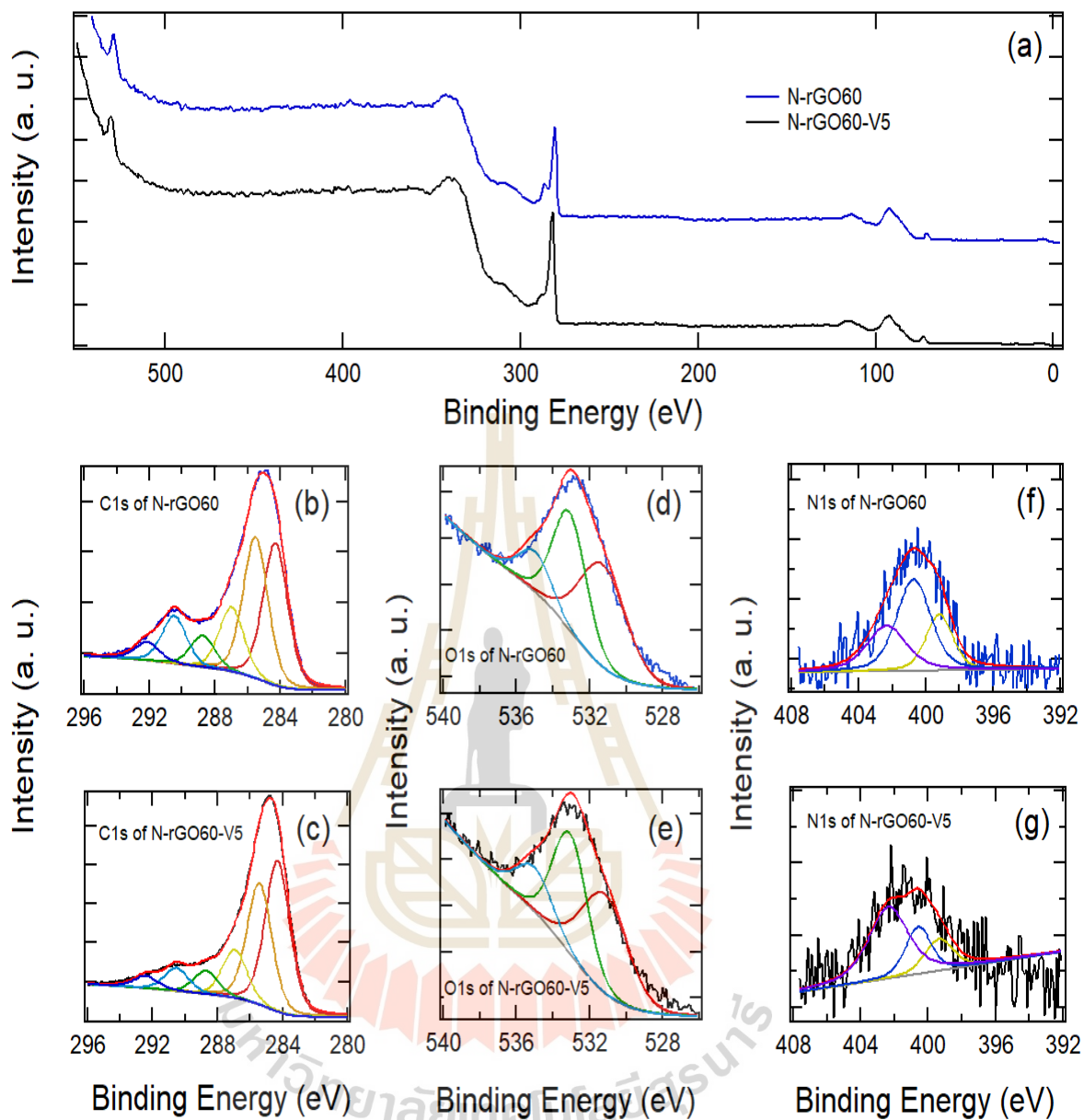


**Figure 4.51** Wide scan N-rGO60 and N-rGO60-V5 (a), C1s of N-rGO60 (b), C1s of N-rGO60 -V5 (c), O1s of N-rGO60 (d), O1s of N-rGO60 -V5 (e), N1s of N-rGO60 (f), N1s of N-rGO60 -V5 (g) electrodes.

**Table 4.20** The results of XPS curve-fitting of C1s from Figure 5.22 (b), (c)- Figure 5.25 (b), (c).

Electrode	Position of each bonding at C1s						Relative C=C (sp <sup>2</sup> )
	sp <sup>2</sup>	C-O/C-N	C=O/C=N	COOH	CHF	C-F	
rGO-V5	284.4	285.6	287.0	288.8	290.6	292.1	0.71
N-rGO20-V5	284.2	285.4	286.9	288.8	290.6	292.4	0.64
N-rGO40-V5	284.2	285.3	286.9	288.6	290.4	292.2	0.74
N-rGO60-V5	284.3	285.4	286.9	288.7	290.6	292.42	0.65

**Table 4.21** The results of XPS curve-fitting of O1s from Figure 5.22 (d), (e)- Figure 5.25 (d), (e).

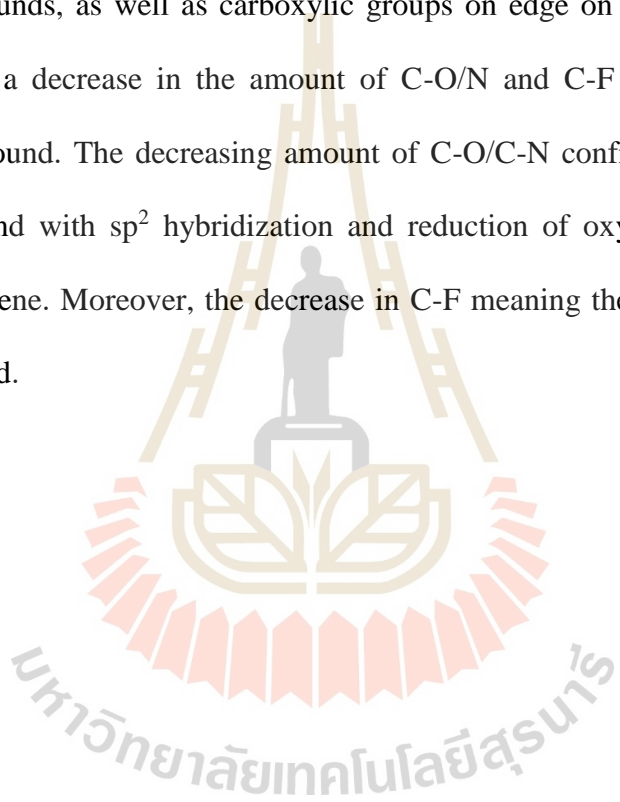
electrode	Position of each bonding at O1s			Area of each bonding at O1s		
	C=O	C-OH/C-O-C	COOH/water	C=O	C-OH/C-O-C	COOH/water
rGO-V5	531.3	533.1	535.0	44.94	43.86	11.20
N-rGO20-V5	531.4	533.2	535.0	41.72	35.21	23.07
N-rGO40-V5	531.2	533.2	535.0	39.06	42.65	18.29
N-rGO60-V5	531.2	533.1	535.0	44.71	39.97	15.33

**Table 4.22** The results of XPS curve-fitting of N1s from Figure 5.23 (f), (g)- Figure 5.25 (f), (g).

electrode	Position of each bonding at N1s			Area of each bonding at N1s		
	pyridinic-N	pyrrolic-N	quaternary-N	pyridinic-N	pyrrolic-N	quaternary-N
N-rGO20-V5	398.4	400.3	402.1	11.81	37.24	50.95
N-rGO40-V5	399.3	400.2	402.2	29.51	29.08	41.41
N-rGO60-V5	399.3	400.5	402.3	17.43	23.35	59.22

To clearer investigate step transformation and more analyze surface chemical compositions, X-ray photoemission spectroscopy (XPS) was performed. Figure 4.52 display the survey scan XPS of N-rGO and N-rGO-V5 electrodes showing three signals of carbon, nitrogen, and oxygen at binding energies of  $\sim 281.0$  eV,  $\sim 400.0$  eV,  $\sim 532.0$  eV, respectively, demonstrating nitrogen being successfully doped into graphene frameworks. It can be seen that after VLT treatment, the magnitude of O 1s and N 1s peaks decreased, while that of C 1s was still the same meaning that oxygen- and nitrogen-containing functional groups are partially removed by violet laser because binding energies of C-O and C-N are lower than the photon energy of violet laser (Souto, Pickholz, Dos Santos, and Alvarez, 1998). Figure 5.26 (b) – (d) illustrate the high-resolution core-level XPS spectra of C1s signal for N-rGO, N-rGO-V1, N-rGO-V3, and N-rGO-V5 electrodes, respectively. In the case of C1s peak of all samples, it can be composed into five components including C=C  $sp^2$ , C-O/N, C=O/N, COOH, and C-F located at a binding energy of 284.0, 286.0, 287.0, 288.5, and 289.5 eV, respectively (Burke, 2000) (K. H. An et al., 2002). It can be confirmed the surface of as-prepared samples consisting of oxygen- and nitrogen-containing functional groups as well as fluorine from polyvinylidene fluoride (PVDF) as a binder. To investigate the effect of cycling number of VLT treatment on the effectively chemically functional groups

removing, Figure 4.52 (f) and (d) illustrating the graphs plotted between percentage number of different functional groups such as C=C  $sp^2$ , C-O/N, C=O/N, COOH, and C-F. As result, the rapid increase in percentage amount of C=C double bond with  $sp^2$  hybridization, and the slightly rising percentage amount of C=O/N, and COOH with repeating of VLT treatment were observed. It means an improvement of electrically conductive properties and an increase in quinone group, which is oxidized derivatives of aromatic compounds, as well as carboxylic groups on edge on graphene structures. On the other hand, a decrease in the amount of C-O/N and C-F with repeating of VLT treatment was found. The decreasing amount of C-O/C-N confirms an enhancement of C=C double bond with  $sp^2$  hybridization and reduction of oxygen/nitrogen functional groups on graphene. Moreover, the decrease in C-F meaning the PVDF as a binder was partially removed.



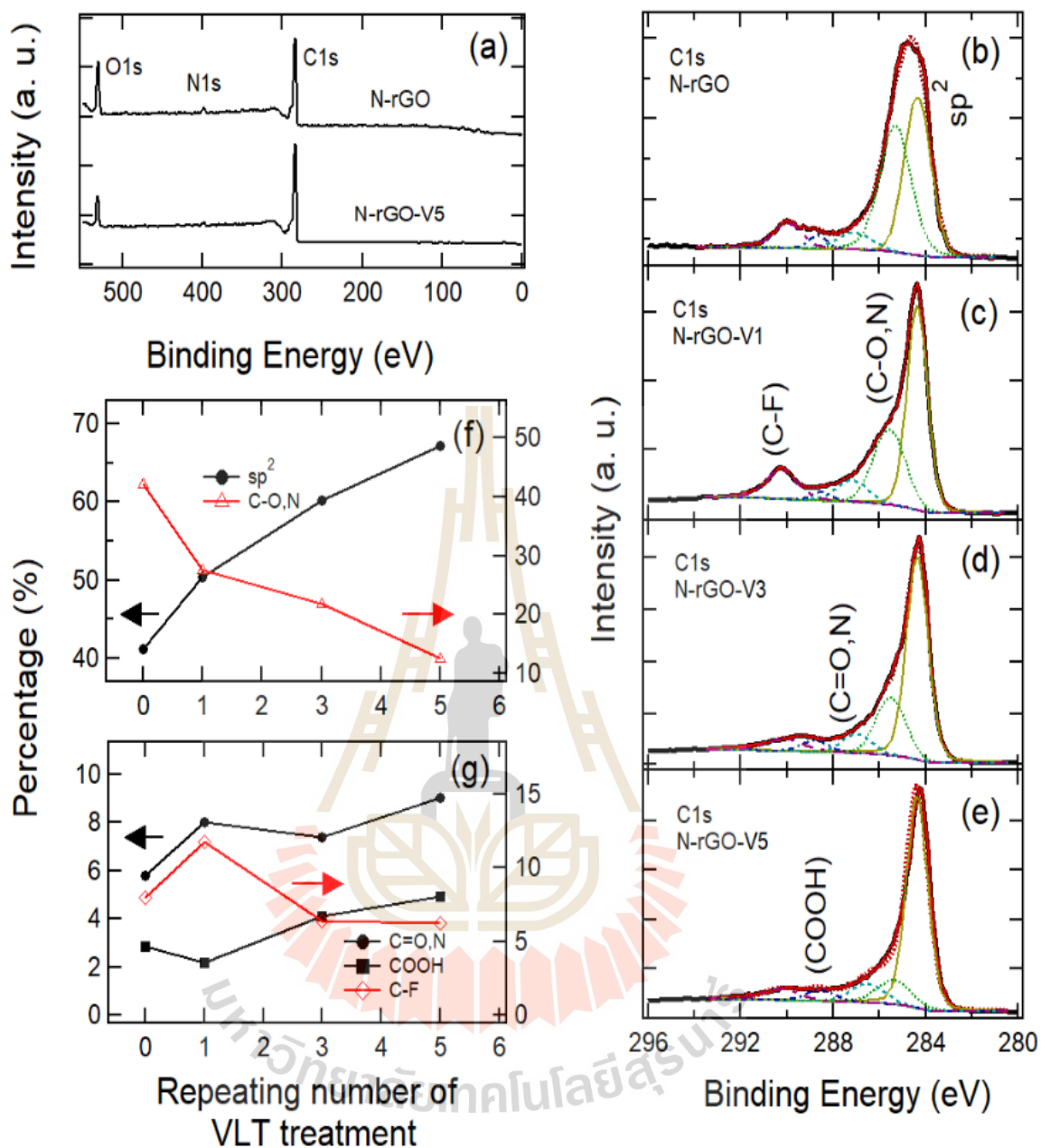


**Figure 4.52** Survey scan XPS spectra of (a) of N-rGO and N-rGO-V5 electrode, high-resolution XPS spectra of C1s signal for (b) N-rGO, (c) N-rGO-V1, (d) N-rGO-V3 and (e) N-rGO-V5 electrode, (f) percentage amount of C=C  $sp^2$  and C-O/N, species and (g) percentage amount of C=O/N, COOH, and C-F species concerning the repeating number of VLT treatments.

#### 4.4.2.4 Raman spectroscopy

To investigate step transformation of the formation of C=C  $sp^2$  graphitic carbon in graphene with the repeating number of VLT treatment, N-rGO40 was used to be representative. Raman spectra of N-rGO, N-rGO-V1, N-rGO-V3, and N-rGO-V5 electrode. The Raman spectra were deconvoluted based on Lorentzian functions for D- and G- bands and based on Gaussian function for D' - and D'' - bands in range of 1000-1800  $cm^{-1}$  (Berrellez-Reyes and Alvarez-Garcia, 2019) (Claramunt et al., 2015). As results, there were four deconvolution peaks located at  $\sim 1618$ ,  $\sim 1590$ ,  $\sim 1520$ , and  $\sim 1345$   $cm^{-1}$  corresponding to disorder-induced phonon mode due to crystal defects (D' -band), graphitic carbon phase with C=C double bond with  $sp^2$ -hybridization (G-band), amorphous  $sp^2$ -bonded carbons or interstitial defects (D'' -band), and defect graphite structure (D -band), respectively (Tuinstra and Koenig, 1970) (X. Zhao and Ando, 1998) (Ferrari and Robertson, 2000). The fitted data of Raman spectra curves of all deconvoluted signals are summarized in Table 4.23. Also, the decrease in the intensity ratios between D-band and G-band ( $I_D/I_G$ ) and between D''-band and G-band ( $I_{D''}/I_G$ ) reflects an increase in the degree of C=C  $sp^2$ -bonded graphitization, which is implied re-establishment of  $sp^2$  electron configuration. Furthermore, the results show that the values of  $I_D/I_G$  and  $I_{D''}/I_G$  ratios decreased with the repeating number of VLT treatments signifying an increase in C=C double bond with  $sp^2$  hybridization content and successful reductions of oxygen/nitrogen-containing functional groups on graphene via VLT treatment (Claramunt et al., 2015) (Childres et al., 2013). Besides, the effect of the repeating number of VLT treatments on the shift of the G-band peak position was further investigated, as displayed in Figure 4.53. After repeating VLT for 5th cycles, the peak position of G-band for N-rGO-V5 electrode ( $1583.4$   $cm^{-1}$ ) was significantly shifted to

lower wavenumber, compared to that of N-rGO electrode ( $1590.1 \text{ cm}^{-1}$ ), which can be clarified a transition from an amorphous to a more crystalline carbon state of graphene (Strong et al., 2012), while others were still located at the same position.

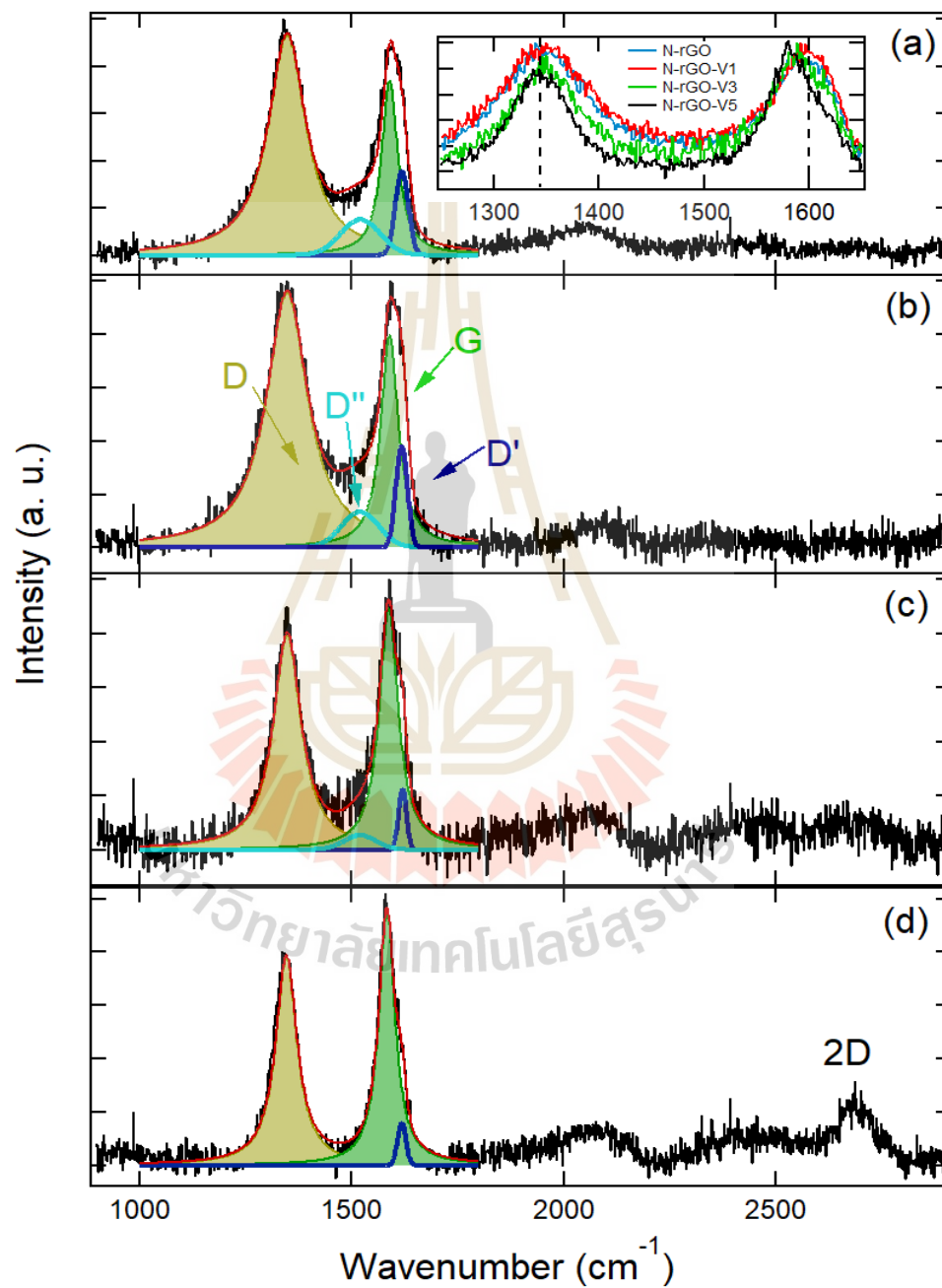
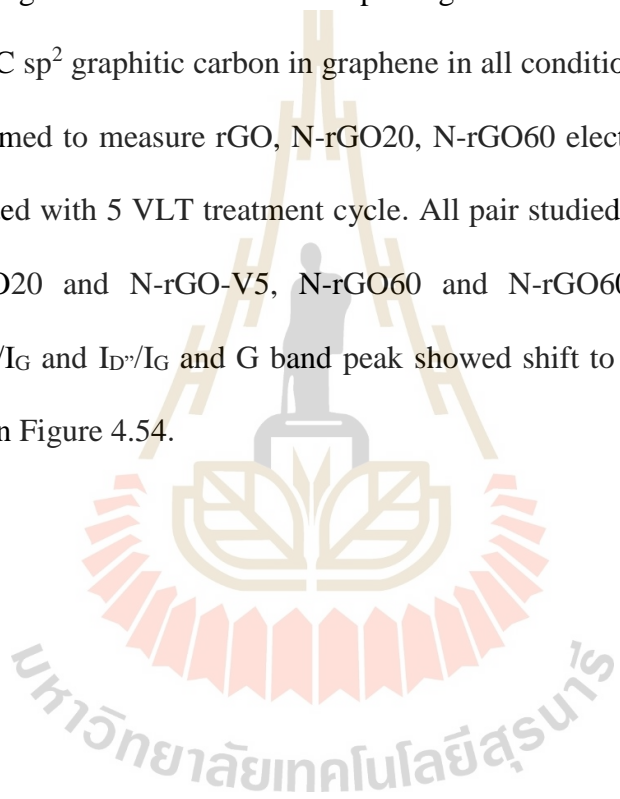


**Figure 4.53** Raman spectroscopy result of N-rGO40, N-rGO40-V1, N-rGO40-V3 and N-rGO40-V5 electrodes.

**Table 4.23** The fitted data and analyzed data of Raman spectra curves.

electrode	$I_D/I_G$	$I_{D''}/I_G$	Position				Area			
			D	D''	G	D'	D	D''	G	D'
N-rGO40	2.98	0.32	1348.1	1520.9	1590.1	1618.3	159.2	17.0	53.4	13.8
N-rGO40-V1	2.83	0.24	1348.1	1520.1	1589.7	1618.0	177.4	15.1	62.7	13.0
N-rGO40-V3	1.31	0.07	1348.3	1521.0	1587.8	1620.0	98.9	5.3	75.5	5.3
N-rGO40-V5	1.07	-	1346.5	-	1583.4	1618.5	74.9	-	69.6	4.0

To investigate the effect of the repeating number of VLT treatment on the formation of C=C  $sp^2$  graphitic carbon in graphene in all conditions, Raman spectroscopy were also performed to measure rGO, N-rGO20, N-rGO60 electrode and their electrode which were treated with 5 VLT treatment cycle. All pair studied electrode such rGO and rGO-V5, N-rGO20 and N-rGO-V5, N-rGO60 and N-rGO60-V5 electrode showed decreasing of  $I_D/I_G$  and  $I_{D''}/I_G$  and G band peak showed shift to lower wavenumber (red shift) as shown in Figure 4.54.



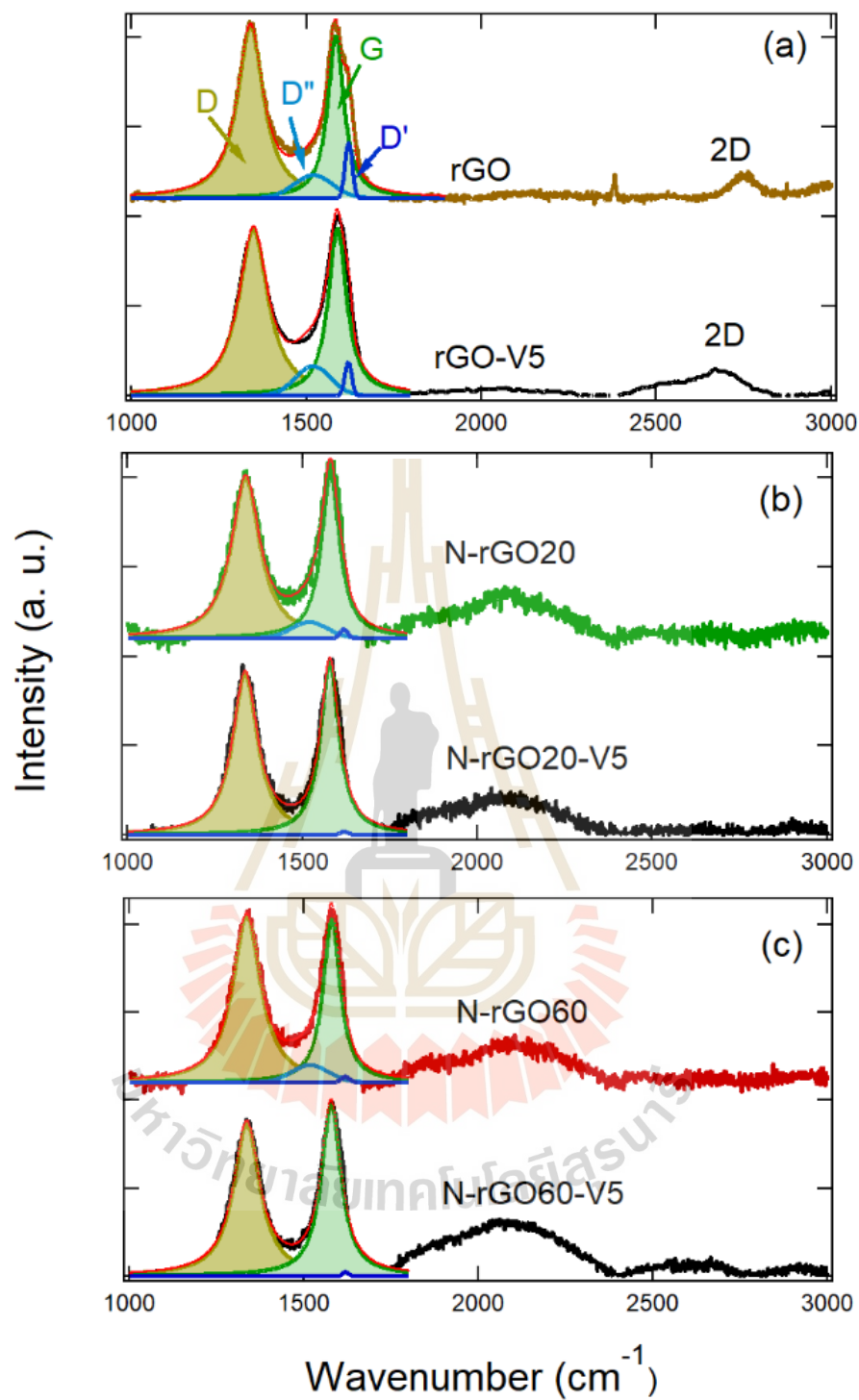


**Figure 4.54** Comparative Raman spectroscopy result for rGO, rGO-V5, N-rGO20, N-rGO20-V5, N-rGO60, and N-rGO60-V5 electrodes.

**Table 4.24** The fitted data and analyzed data of Raman spectra curves.

electrode	$I_D/I_G$	$I_{D''}/I_G$	Position				Area			
			D	D''	G	D'	D	D''	G	D'
rGO	1.71	0.23	1340.9	1520.5	1584.6	1620.9	137.2	18.1	80.1	8.2
rGO-V5	1.59	0.22	1348.9	1519.6	1589.0	1619.8	148.5	21.0	93.2	4.8
N-rGO20	1.51	0.13	1338.4	1520.6	1580.8	1618.7	139.9	12.2	92.8	1.5
N-rGO20-V5	1.26	-	1336.8	-	1578.8	1620.6	124.0	-	98.5	0.6
N-rGO60	1.66	0.16	1336.7	1518.5	1580.2	1619.6	144.9	13.7	87.4	1.1
N-rGO60-V5	1.18	-	1336.9	-	1578.6	1620.4	124.3	-	105.4	0.5

#### 4.4.2.5 Contact angle

Wettability of VLT treated electrode were decreased and more decreasing when the repeating number of VLT treatment increase. These results are expectation results which oxygen functional group or heteroatom were removed then contact angle will be increased as shown in Figure 4.55. Unfortunately, VLT treatment affect on these electrodes with worse for this a characterized aspect because we need to enhance wettability for SCs electrode.

Electrode	Treated (round)	Picture	Contact angle (°)	Electrode	Treated (round)	Picture	Contact angle(°)
rGO	non		149.8	N-rGO40	non		142.8
	1		150.4		1		145.9
	3		147.2		3		149.4
	5		146.1		5		153.9
N-rGO20	non		143.8	N-rGO60	non		146
	1		143.1		1		152.2
	3		145.1		3		154.6
	5		146.8		5		155.6

**Figure 4.55** Picture and results of contact angle of all electrodes (rGO, rGO-VX, N-rGOY, and N-rGOY-VX).

Figure 4.56 showed contact angle for all electrode which exhibited increasing trend of contact angle with increase the repeating number of VLT treatment. These results were explained using removing of heteroatom from electrode surface (Szciodrowski et al., 2009).

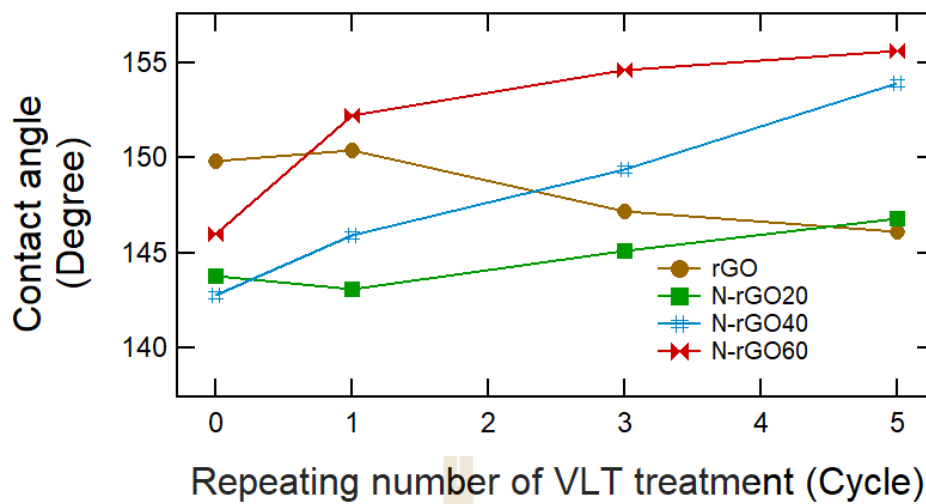
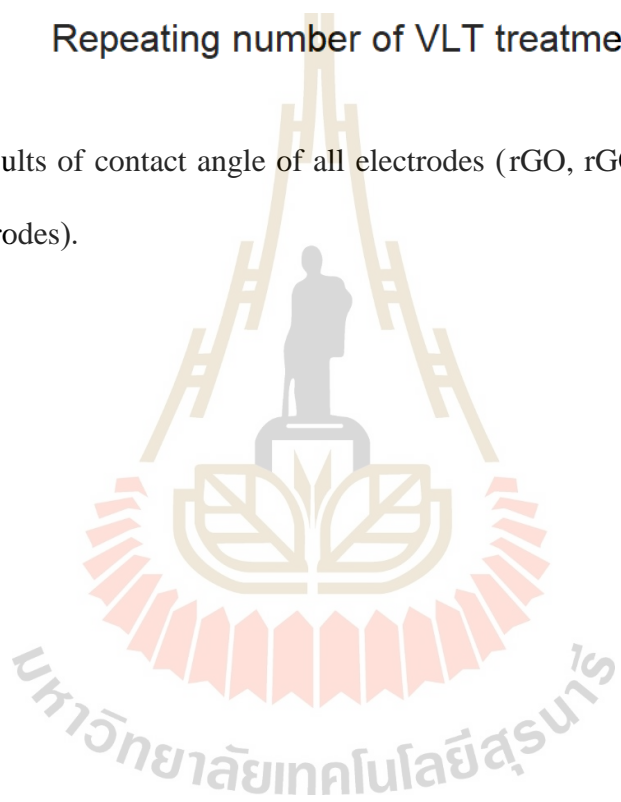


**Figure 4.56** Results of contact angle of all electrodes (rGO, rGO-VX, N-rGOY, and N-rGOY-VX electrodes).



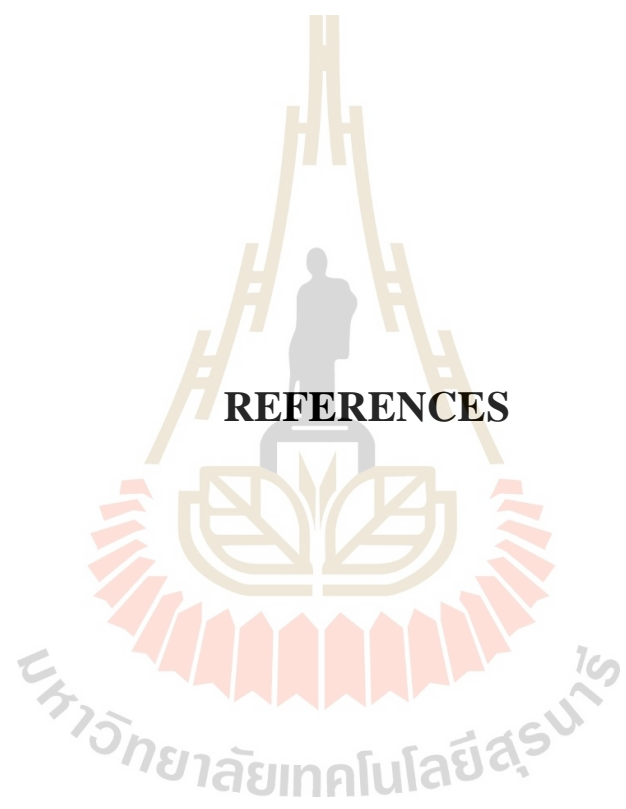
## CHAPTER V

### CONCLUSIONS

Graphene oxide was completely synthesized using Hummers method via characterizing with many technique and in agreement with other research. Further, intrinsic properties of graphene oxide were improve using hydrothermal method with varies urea concentrations in DI water (Y is urea concentration), called N-rGOY. This technique provided higher the specific capacitance for all doping conditions which were attributed the improvement by 3 species of nitrogen doping in graphene oxide structure such pyridinic-N, pyrrolic-N, and quaternary/graphitic-N. There are reasons that can be attributed best urea concentration is 40% w/v such highest present of pyridinic-N that might be caused pseudocapacitance, suitable and optimal concentration for introducing of nitrogen into carbon in graphene oxide structure with lowest of creation insulating urea blocking active sites of graphene which cause from excess amount of urea concentration. Furthermore, rGO, N-rGO, and NandS-rGO which is performed from thiourea doping showed comparative study to show monomer doping is a better condition than co-doping because N-rGO showed higher rate introducing of nitrogen atom to replace carbon atom for quaternary/graphitic-N. Electrical conductivity is showed as significant factor more than pseudocapacitance for supercapacitor application.

The surface of rGO, N-rGOY was successfully modified by the VLT technique (called rGO-VX, and N-rGOY-VX). To achieve better performance, VLT machine must be set the repeating number more than 3-5 cycles and intensity for more than 7-10.2 V via applied voltage. The morphologies of N-rGO-VX were examined by the SEM, which

exhibited a rougher surface with many bright spots appearing on their surface. The XPS confirms VLT technique can increase the degree of C=C sp<sup>2</sup>-bonded graphitization, which reflects the re-establishment of sp<sup>2</sup> electron configuration, while can decrease in oxygen-containing functional groups demonstrating partially reduced graphene oxide by VLT technique. The Raman spectroscopy of electrodes showed the decrease in the intensity ratios between I<sub>D</sub>/I<sub>G</sub> and I<sub>D'</sub>/I<sub>G</sub> with the repeating number of VLT treatments, confirming an increase in the degree of C=C sp<sup>2</sup>-bonded graphitization. The specific capacitances notably increase with the increasing relative ratio of C=C sp<sup>2</sup>, while those fell off with a rising in I<sub>D</sub>/I<sub>G</sub> and I<sub>D'</sub>/I<sub>G</sub> ratios. Particularly, the N-rGO-V5 exhibited the highest specific capacitance with excellent stability and a low self-discharging rate. The improvement of electrochemical properties is due to the synergistic effect of nitrogen contents in N-rGO and the repeating number of VLT treatments. Therefore, these nitrogens doped reduced graphene oxide (N-rGO) and violet laser treating (VLT) technique might be a promising method to enhance supercapacitors electrode performance for large-scale in industry.



**REFERENCES**

## REFERENCES

- Acharya, S., Gopinath, C. S., Alegaonkar, P. and Datar, S. (2018). Enhanced microwave absorption property of reduced graphene oxide (RGO)–strontium hexaferrite (SF)/poly (vinylidene) fluoride (PVDF). **Diamond and Related Materials**. 89: 28-34.
- Ai, W., Zhou, W., Du, Z., Du, Y., Zhang, H., Jia, X. and Huang, W. (2012). Benzoxazole and benzimidazole heterocycle-grafted graphene for high-performance supercapacitor electrodes. **Journal of Materials Chemistry**. 22(44): 23439-23446.
- An, K., Kim, W., Park, Y., Choi, Y., Lee, S. and Chung, D. (2001). Bae, SC Lim, YH Lee. **Advanced Materials**. 13: 497.
- An, K. H., Heo, J. G., Jeon, K. G., Bae, D. J., Jo, C., Yang, C. W. and Hung, Y. S. (2002). X-ray photoemission spectroscopy study of fluorinated single-walled carbon nanotubes. **Applied Physics Letters**. 80(22): 4235-4237.
- Azaïs, P., Duclaux, L., Florian, P., Massiot, D., Lillo-Rodenas, M.-A., Linares-Solano, A. and Béguin, F. (2007). Causes of supercapacitors ageing in organic electrolyte. **Journal of power sources**. 171(2): 1046-1053.
- Ban, F., Majid, S. R., Huang, N. M. and Lim, H. (2012). Graphene oxide and its electrochemical performance. **International Journal of Electrochemical**. 7(5): 4345-4351.
- Barra, A., Lazăr, O., Pantazi, A., Hortigüela, M. J., Otero-Irurueta, G., Enăchescu, M. and Ferreira, P. (2021). Joining Caffeic Acid and Hydrothermal Treatment to

- Produce Environmentally Benign Highly Reduced Graphene Oxide. **Nanomaterials**. 11(3): 732.
- Berrellez-Reyes, F. and Alvarez-Garcia, S. (2019). Insights into the Interaction of Graphene Oxide and Adsorbed RhB by Raman Spectral Deconvoluted Scanning. **The Journal of Physical Chemistry C**. 123(49): 30021-30027.
- Bi, R. R., Wu, X. L., Cao, F. F., Jiang, L. Y., Guo, Y. G. and Wan, L. J. (2010). Highly dispersed RuO<sub>2</sub> nanoparticles on carbon nanotubes: facile synthesis and enhanced supercapacitance performance. **The Journal of Physical Chemistry C**. 114(6): 2448-2451.
- Biniak, S., Szymański, G., Siedlewski, J. and Świątkowski, A. (1997). The characterization of activated carbons with oxygen and nitrogen surface groups. **Carbon**. 35(12): 1799-1810.
- Bøckman, O., Østvold, T., Voyiatzis, G. A. and Papatheodorou, G. N. (2000). Raman spectroscopy of cemented cobalt on zinc substrates. **Hydrometallurgy**. 55(1): 93-105.
- Borenstein, A., Strauss, V., Kowal, M. D., Yoonessi, M., Muni, M., Anderson, M. and Kaner, R. B. (2018). Laser-reduced graphene-oxide/ferrocene: a 3-D redox-active composite for supercapacitor electrodes. **Journal of Materials Chemistry A**. 6(41): 20463-20472.
- Brodie, B. C. (1859). XIII. On the atomic weight of graphite. **Philosophical Transactions of the Royal Society of London**. 149: 249-259.
- Burke, A. (2000). Ultracapacitors: why, how, and where is the technology. **Journal of power sources**. 91(1): 37-50.

- Chae, J., Ng, K. and Chen, G. (2010). Nanostructured materials for the construction of asymmetrical supercapacitors. Proceedings of the Institution of Mechanical Engineers, Part A. **Journal of Power and Energy**. 224(4): 479-503.
- Chen, W., Fan, Z., Gu, L., Bao, X. and Wang, C. (2010). Enhanced capacitance of manganese oxide via confinement inside carbon nanotubes. **Chemical Communications**. 46(22): 3905-3907.
- Chen, X., Xu, X., Yang, Z., Liu, Z., Zhang, L., Xu, X. and Huang, S. (2014). Sulfur-doped porous reduced graphene oxide hollow nanosphere frameworks as metal-free electrocatalysts for oxygen reduction reaction and as supercapacitor electrode materials. **Nanoscale**. 6(22): 13740-13747.
- Childres, I., Jauregui, L. A., Park, W., Cao, H. and Chen, Y. P. (2013). Raman spectroscopy of graphene and related materials. **New developments in photon and materials research**. 1: 1-20.
- Claramunt, S., Varea, A., Lopez-Diaz, D., Velázquez, M. M., Cornet, A. and Cirera, A. (2015). The importance of interbands on the interpretation of the Raman spectrum of graphene oxide. **The Journal of Physical Chemistry C**. 119(18): 10123-10129.
- Compton, O. C. and Nguyen, S. T. (2010). Graphene oxide, highly reduced graphene oxide, and graphene: versatile building blocks for carbon-based materials. **small**. 6(6): 711-723.
- Conway, B. (1993). Two-dimensional and quasi-two-dimensional isotherms for Li intercalation and UPD processes at surfaces. **Electrochimica Acta**. 38(9): 1249-1258.

- Conway, B. E. (1991). Transition from “supercapacitor” to “battery” behavior in electrochemical energy storage. **Journal of the Electrochemical Society**. 138(6): 1539.
- Conway, B. E., Birss, V. and Wojtowicz, J. (1997). The role and utilization of pseudocapacitance for energy storage by supercapacitors. *Journal of power sources*. 66(1-2): 1-14.
- Dai, Z., Ren, P.-G., Jin, Y.-L., Zhang, H., Ren, F. and Zhang, Q. (2019). Nitrogen-sulphur Co-doped graphenes modified electrospun lignin/polyacrylonitrile-based carbon nanofiber as high performance supercapacitor. **Journal of power sources**. 437: 226937.
- Du, C. and Pan, N. (2006). Supercapacitors using carbon nanotubes films by electrophoretic deposition. **Journal of power sources**. 160(2): 1487-1494.
- Dubal, D. P., Ayyad, O., Ruiz, V. and Gomez-Romero, P. (2015). Hybrid energy storage: the merging of battery and supercapacitor chemistries. **Chemical Society Reviews**. 44(7): 1777-1790.
- Dyatkin, B., Presser, V., Heon, M., Lukatskaya, M. R., Beidaghi, M. and Gogotsi, Y. (2013). Development of a green supercapacitor composed entirely of environmentally friendly materials. **ChemSusChem**. 6(12): 2269-2280.
- Eigler, S., Dotzer, C. and Hirsch, A. (2012). Visualization of defect densities in reduced graphene oxide. *Carbon*. 50(10): 3666-3673.
- El-Kady, M. F., Strong, V., Dubin, S. and Kaner, R. B. (2012). Laser scribing of high-performance and flexible graphene-based electrochemical capacitors. **science**. 335(6074), 1326-1330.

- Faisal, S. N., Haque, E., Noorbehesht, N., Zhang, W., Harris, A. T., Church, T. L. and Minett, A. I. (2017). Pyridinic and graphitic nitrogen-rich graphene for high-performance supercapacitors and metal-free bifunctional electrocatalysts for ORR and OER. **RSC Advances**. 7(29): 17950-17958.
- Fan, X., Yu, C., Yang, J., Ling, Z. and Qiu, J. (2014). Hydrothermal synthesis and activation of graphene-incorporated nitrogen-rich carbon composite for high-performance supercapacitors. **Carbon**. 70: 130-141.
- Ferrari, A. C. and Robertson, J. (2000). Interpretation of Raman spectra of disordered and amorphous carbon. **Physical Review B**. 61(20): 14095.
- Frackowiak, E. (2007). Carbon materials for supercapacitor application. **Physical chemistry chemical physics**. 9(15): 1774-1785.
- Gilje, S., Han, S., Wang, M., Wang, K. L. and Kaner, R. B. (2007). A chemical route to graphene for device applications. **Nano letters**. 7(11): 3394-3398.
- Gómez-Navarro, C., Meyer, J. C., Sundaram, R. S., Chuvilin, A., Kurasch, S., Burghard, M. and Kaiser, U. (2010). Atomic structure of reduced graphene oxide. **Nano letters**. 10(4): 1144-1148.
- Guerrero, M. A., Romero, E., Barrero, F., Milanés, M. I. and Gonzalez, E. (2009). Supercapacitors: Alternative energy storage systems. **Przegląd Elektrotechniczny**. 85(10): 188-195.
- Han, Z., Tang, Z., Li, P., Yang, G., Zheng, Q. and Yang, J. (2013). Ammonia solution strengthened three-dimensional macro-porous graphene aerogel. **Nanoscale**. 5(12): 5462-5467.

- Herrero, E., Buller, L. J. and Abruña, H. D. (2001). Underpotential deposition at single crystal surfaces of Au, Pt, Ag and other materials. **Chemical reviews**. 101(7): 1897-1930.
- Hofmann, U. and Holst, R. (1939). Über die Säurenatur und die Methylierung von Graphitoxyd. **Berichte der deutschen chemischen Gesellschaft (A and B Series)**. 72(4): 754-771.
- Hu, C.-C., Chang, K.-H., Lin, M.-C. and Wu, Y.-T. (2006). Design and tailoring of the nanotubular arrayed architecture of hydrous RuO<sub>2</sub> for next generation supercapacitors. **Nano letters**. 6(12): 2690-2695.
- Hu, Y., Shen, J., Li, N., Shi, M., Ma, H., Yan, B. and Ye, M. (2010). Amino - functionalization of graphene sheets and the fabrication of their nanocomposites. **Polymer composites**. 31(12): 1987-1994.
- Huang, X., Qi, X., Boey, F. and Zhang, H. (2012). Graphene-based composites. **Chemical Society Reviews**. 41(2): 666-686.
- Huang, Y., Huang, Z., Zhong, Z., Yang, X., Hong, Q., Wang, H. and Cai, D. (2018). Highly transparent light emitting diodes on graphene encapsulated Cu nanowires network. **Scientific reports**. 8(1): 1-11.
- Hulicova-Jurcakova, D., Sereych, M., Lu, G. Q. and Bandosz, T. J. (2009). Combined effect of nitrogen-and oxygen-containing functional groups of microporous activated carbon on its electrochemical performance in supercapacitors. **Advanced Functional Materials**. 19(3): 438-447.
- Hummers Jr, W. S. and Offeman, R. E. (1958). Preparation of graphitic oxide. **Journal of the american chemical society**. 80(6): 1339-1339.

- Jeon, J. W., Zhang, L., Lutkenhaus, J. L., Laskar, D. D., Lemmon, J. P., Choi, D. and Motkuri, R. K. (2015). Controlling porosity in lignin-derived nanoporous carbon for supercapacitor applications. **ChemSusChem**. 8(3): 428-432.
- Kapteijn, F., Moulijn, J., Matzner, S. and Boehm, H. P. (1999). The development of nitrogen functionality in model chars during gasification in CO<sub>2</sub> and O<sub>2</sub>. **Carbon**. 37(7): 1143-1150.
- Kelemen, S. and Kwiatek, P. (1995). Quantification of organic oxygen species on the surface of fresh and reacted Argonne Premium coal. **Energy and fuels**. 9(5): 841-848.
- Kim, C. and Yang, K. (2003). Electrochemical properties of carbon nanofiber web as an electrode for supercapacitor prepared by electrospinning. **Applied Physics Letters**. 83(6): 1216-1218.
- Kim, D. K., Bong, S., Jin, X., Seong, K.-d., Hwang, M., Kim, N. D. and Piao, Y. (2018). Facile in situ synthesis of multiple-heteroatom-doped carbons derived from polyimide precursors for flexible all-solid-state supercapacitors. **ACS applied materials and interfaces**. 11(2): 1996-2005.
- Kong, L., Zhang, C., Zhang, S., Wang, J., Cai, R., Lv, C. and Long, D. (2014). High-power and high-energy asymmetric supercapacitors based on Li<sup>+</sup>-intercalation into a T-Nb<sub>2</sub>O<sub>5</sub>/graphene pseudocapacitive electrode. **Journal of Materials Chemistry A**. 2(42): 17962-17970.
- Kötz, R. and Carlen, M. (2000). Principles and applications of electrochemical capacitors. **Electrochimica Acta**. 45(15-16): 2483-2498.
- Lee, S. Y. and Park, S. J. (2014). Isothermal exfoliation of graphene oxide by a new carbon dioxide pressure swing method. **Carbon**. 68: 112-117.

- Lee, W. S. V., Leng, M., Li, M., Huang, X. L. and Xue, J. M. (2015). Sulphur-functionalized graphene towards high performance supercapacitor. **Nano Energy**. 12: 250-257.
- Lee, Y.-H., Chang, K.-H. and Hu, C.-C. (2013). Differentiate the pseudocapacitance and double-layer capacitance contributions for nitrogen-doped reduced graphene oxide in acidic and alkaline electrolytes. **Journal of power sources**. 227: 300-308.
- Lerf, A., He, H., Forster, M. and Klinowski, J. (1998). Structure of graphite oxide revisited. **The Journal of Physical Chemistry B**. 102(23): 4477-4482.
- Li, W., Chen, J., Zhao, J., Zhang, J. and Zhu, J. (2005). Application of ultrasonic irradiation in preparing conducting polymer as active materials for supercapacitor. **Materials Letters**. 59(7): 800-803.
- Li, Y., Zhang, S., Song, H., Chen, X., Zhou, J. and Hong, S. (2015). New insight into the heteroatom-doped carbon as the electrode material for supercapacitors. **Electrochimica Acta**. 180: 879-886.
- Liao, Y., Huang, Y., Shu, D., Zhong, Y., Hao, J., He, C. and Song, X. (2016). Three-dimensional nitrogen-doped graphene hydrogels prepared via hydrothermal synthesis as high-performance supercapacitor materials. **Electrochimica Acta**. 194: 136-142.
- Lin, Z., Waller, G. H., Liu, Y., Liu, M. and Wong, C. p. (2013). 3D Nitrogen-doped graphene prepared by pyrolysis of graphene oxide with polypyrrole for electrocatalysis of oxygen reduction reaction. **Nano Energy**. 2(2): 241-248.
- Liu, C., Yu, Z., Neff, D., Zhamu, A. and Jang, B. Z. (2010). Graphene-based supercapacitor with an ultrahigh energy density. **Nano letters**. 10(12): 4863-4868.

- Long, D., Li, W., Ling, L., Miyawaki, J., Mochida, I. and Yoon, S.-H. (2010). Preparation of nitrogen-doped graphene sheets by a combined chemical and hydrothermal reduction of graphene oxide. **Langmuir**. 26(20): 16096-16102.
- Lorenc-Grabowska, E., Gryglewicz, G. and Diez, M. (2013). Kinetics and equilibrium study of phenol adsorption on nitrogen-enriched activated carbons. **Fuel**. 114: 235-243.
- Lota, G., Grzyb, B., Machnikowska, H., Machnikowski, J. and Frackowiak, E. (2005). Effect of nitrogen in carbon electrode on the supercapacitor performance. **Chemical Physics Letters**. 404(1-3): 53-58.
- Ma, H. L., Zhang, H. B., Hu, Q. H., Li, W. J., Jiang, Z. G., Yu, Z. Z. and Dasari, A. (2012). Functionalization and reduction of graphene oxide with p-phenylene diamine for electrically conductive and thermally stable polystyrene composites. **ACS applied materials and interfaces**. 4(4): 1948-1953.
- Mane, R. S., Chang, J., Ham, D., Pawar, B., Ganesh, T., Cho, B. W. and Han, S. H. (2009). Dye-sensitized solar cell and electrochemical supercapacitor applications of electrochemically deposited hydrophilic and nanocrystalline tin oxide film electrodes. **Current Applied Physics**. 9(1): 87-91.
- Markervich, E., Salitra, G., Levi, M. and Aurbach, D. (2005). Capacity fading of lithiated graphite electrodes studied by a combination of electroanalytical methods, Raman spectroscopy and SEM. **Journal of power sources**. 146(1-2): 146-150.
- Mei, B.-A., Munteshari, O., Lau, J., Dunn, B. and Pilon, L. (2018). Physical interpretations of Nyquist plots for EDLC electrodes and devices. **The Journal of Physical Chemistry C**. 122(1): 194-206.

- Miller, J. R. and Simon, P. (2008). Electrochemical capacitors for energy management. **Science**. 321(5889): 651-652.
- Montes-Navajas, P., Asenjo, N. G., Santamaría, R., Menendez, R., Corma, A. and García, H. (2013). Surface area measurement of graphene oxide in aqueous solutions. **Langmuir**. 29(44): 13443-13448.
- Nakae, H., Inui, R., Hirata, Y. and Saito, H. (1998). Effects of surface roughness on wettability. **Acta materialia**. 46(7): 2313-2318.
- Nakajima, T., Mabuchi, A. and Hagiwara, R. (1988). A new structure model of graphite oxide. **Carbon**. 26(3): 357-361.
- Nguyen, Q. T. and Baird, D. G. (2007). An improved technique for exfoliating and dispersing nanoclay particles into polymer matrices using supercritical carbon dioxide. **Polymer**. 48(23): 6923-6933.
- Ni, Z. H., Yu, T., Lu, Y. H., Wang, Y. Y., Feng, Y. P. and Shen, Z. X. (2008). Uniaxial strain on graphene: Raman spectroscopy study and band-gap opening. **ACS nano**. 2(11): 2301-2305.
- Pan, H., Li, J. and Feng, Y. (2010). Carbon nanotubes for supercapacitor. **Nanoscale research letters**. 5(3): 654-668.
- Pandolfo, A. G. and Hollenkamp, A. F. (2006). Carbon properties and their role in supercapacitors. **Journal of power sources**. 157(1): 11-27.
- Pang, H., Wang, X., Zhang, G., Chen, H., Lv, G. and Yang, S. (2010). Characterization of diamond-like carbon films by SEM, XRD and Raman spectroscopy. **Applied Surface Science**. 256(21): 6403-6407.

- Park, J. and Kim, S. (2014). Nitrogen modified-reduced graphene oxide supports for catalysts for fuel cells and their electrocatalytic activity. **Journal of the Electrochemical Society**. 161(4): F518.
- Park, J. H., Park, O. O., Shin, K. H., Jin, C. S. and Kim, J. H. (2002). An electrochemical capacitor based on a Ni (OH)<sub>2</sub>/activated carbon composite electrode. **Electrochemical and Solid-State Letters**. 5(2): H7-H10.
- Qu, Q., Zhang, P., Wang, B., Chen, Y., Tian, S., Wu, Y. and Holze, R. (2009). Electrochemical performance of MnO<sub>2</sub> nanorods in neutral aqueous electrolytes as a cathode for asymmetric supercapacitors. **The Journal of Physical Chemistry C**. 113(31): 14020-14027.
- Ragone, D. V. (1968). *Review of battery systems for electrically powered vehicles*. 0148-7191. Retrieved from.
- Robinson, J. T., Perkins, F. K., Snow, E. S., Wei, Z. and Sheehan, P. E. (2008). Reduced graphene oxide molecular sensors. **Nano letters**. 8(10): 3137-3140.
- Rochman, R. A., Wahyuningsih, S., Ramelan, A. H. and Hanif, Q. A. (2019). *Preparation of nitrogen and sulphur Co-doped reduced graphene oxide (rGO-NS) using N and S heteroatom of thiourea*. Paper presented at the IOP Conference Series: Materials Science and Engineering.
- Roy, R., Deb, B., Bhattacharjee, B. and Pal, A. (2002). Synthesis of diamond-like carbon film by novel electrodeposition route. **Thin solid films**. 422(1-2): 92-97.
- Ryu, S. H. and Shanmugharaj, A. (2014). Influence of long-chain alkylamine-modified graphene oxide on the crystallization, mechanical and electrical properties of isotactic polypropylene nanocomposites. **Chemical Engineering Journal**. 244: 552-560.

- Saleem, H., Haneef, M. and Abbasi, H. Y. (2018). Synthesis route of reduced graphene oxide via thermal reduction of chemically exfoliated graphene oxide. **Materials Chemistry and Physics**. 204: 1-7.
- Shao, Y., El-Kady, M. F., Sun, J., Li, Y., Zhang, Q., Zhu, M. and Kaner, R. B. (2018). Design and mechanisms of asymmetric supercapacitors. **Chemical reviews**. 118(18): 9233-9280.
- Shayeh, J. S., Ehsani, A., Ganjali, M., Norouzi, P. and Jaleh, B. (2015). Conductive polymer/reduced graphene oxide/Au nano particles as efficient composite materials in electrochemical supercapacitors. **Applied Surface Science**. 353: 594-599.
- Shin, H. J., Kim, K. K., Benayad, A., Yoon, S. M., Park, H. K., Jung, I. S. and Choi, J. Y. (2009). Efficient reduction of graphite oxide by sodium borohydride and its effect on electrical conductance. **Advanced Functional Materials**. 19(12): 1987-1992.
- Simon, P. and Gogotsi, Y. (2010). Materials for electrochemical capacitors. In **Nanoscience and technology: a collection of reviews from Nature Journals** pp. 320-329: World Scientific.
- Sing, K. S. (1985). Reporting physisorption data for gas/solid systems with special reference to the determination of surface area and porosity (Recommendations 1984). **Pure and applied chemistry**. 57(4): 603-619.
- Singh, V., Patra, M., Manoth, M., Gowd, G., Vadera, S. and Kumar, N. (2009). In situ synthesis of graphene oxide and its composites with iron oxide. **New Carbon Materials**. 24(2): 147-152.
- Slabaugh, W. and Seiler, B. (1962). Interactions of ammonia with graphite oxide. **The Journal of Physical Chemistry**. 66(3): 396-401.

- Śliwak, A., Grzyb, B., Díez, N. and Gryglewicz, G. (2017). Nitrogen-doped reduced graphene oxide as electrode material for high rate supercapacitors. **Applied Surface Science**. 399: 265-271.
- Smirnov, V., Arbuzov, A. and Shulga, Y. M. (2011). SA Bas kakov, VM Martynenko, VE Muradyan, and EI Kresova, "Photoreduction of Graphite Oxide,". **High Energy Chem**. 45: 57-61.
- Soltani, T. and Lee, B.-K. (2017). A benign ultrasonic route to reduced graphene oxide from pristine graphite. **Journal of colloid and interface science**. 486: 337-343.
- Soo, L. T., Loh, K. S., Mohamad, A. B., Daud, W. R. W. and Wong, W. Y. (2016). Effect of nitrogen precursors on the electrochemical performance of nitrogen-doped reduced graphene oxide towards oxygen reduction reaction. **Journal of Alloys and Compounds**. 677: 112-120.
- Souto, S., Pickholz, M., Dos Santos, M. and Alvarez, F. (1998). Electronic structure of nitrogen-carbon alloys ( $a\text{-CN}_x$ ) determined by photoelectron spectroscopy. **Physical Review B**. 57(4): 2536.
- Srinivas, G., Burrell, J. W., Ford, J. and Yildirim, T. (2011). Porous graphene oxide frameworks: synthesis and gas sorption properties. **Journal of Materials Chemistry**. 21(30): 11323-11329.
- Stankovich, S., Piner, R. D., Nguyen, S. T. and Ruoff, R. S. (2006). Synthesis and exfoliation of isocyanate-treated graphene oxide nanoplatelets. **Carbon**. 44(15): 3342-3347.
- Staudenmaier, L. (1898). Verfahren zur darstellung der graphitsäure. **Berichte der deutschen chemischen Gesellschaft**. 31(2): 1481-1487.

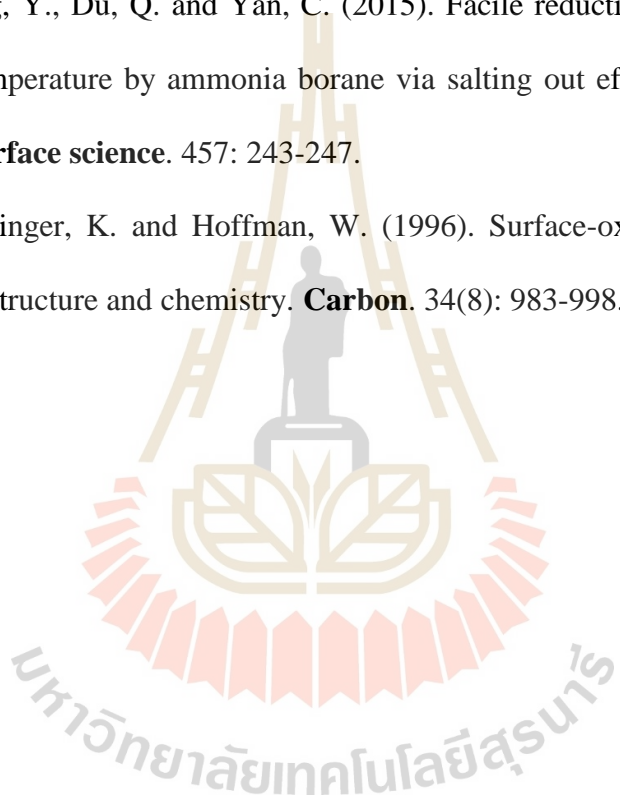
- Stobinski, L., Lesiak, B., Malolepszy, A., Mazurkiewicz, M., Mierzwa, B., Zemek, J. and Bieloshapka, I. (2014). Graphene oxide and reduced graphene oxide studied by the XRD, TEM and electron spectroscopy methods. **Journal of Electron Spectroscopy and Related Phenomena**. 195: 145-154.
- Stoller, M. D., Park, S., Zhu, Y., An, J. and Ruoff, R. S. (2008). Graphene-based ultracapacitors. **Nano letters**. 8(10): 3498-3502.
- Stoller, M. D. and Ruoff, R. S. (2010). Best practice methods for determining an electrode material's performance for ultracapacitors. **Energy and Environmental Science**. 3(9): 1294-1301.
- Strankowski, M., Włodarczyk, D., Piszczyk, Ł. and Strankowska, J. (2016). Polyurethane nanocomposites containing reduced graphene oxide, FTIR, Raman and XRD studies. **Journal of Spectroscopy**. 20: 16.
- Strong, V., Dubin, S., El-Kady, M. F., Lech, A., Wang, Y., Weiller, B. H. and Kaner, R. B. (2012). Patterning and electronic tuning of laser scribed graphene for flexible all-carbon devices. **ACS nano**. 6(2): 1395-1403.
- Sudha, V. and Sangaranarayanan, M. (2002). Underpotential deposition of metals: structural and thermodynamic considerations. **The Journal of Physical Chemistry B**. 106(10): 2699-2707.
- Sun, J., Lei, E., Ma, C., Wu, Z., Xu, Z., Liu, Y. and Liu, S. (2019). Fabrication of three-dimensional microtubular kapok fiber carbon aerogel/RuO<sub>2</sub> composites for supercapacitors. **Electrochimica Acta**. 300: 225-234.
- Szczodrowski, K., Prélot, B., Lantenois, S., Douillard, J. M. and Zajac, J. (2009). Effect of heteroatom doping on surface acidity and hydrophilicity of Al, Ti, Zr-doped mesoporous SBA-15. **Microporous and mesoporous materials**. 124(1-3): 84-93.

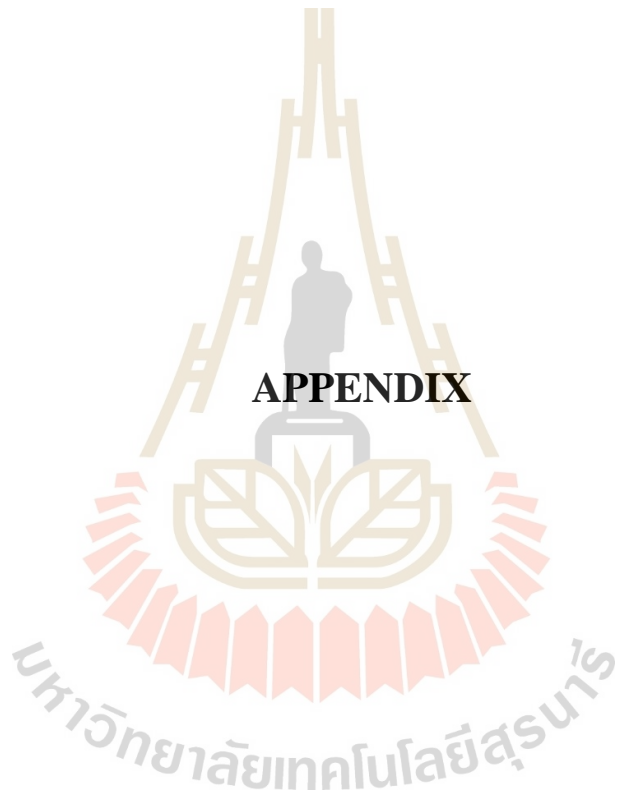
- Taberna, P. L., Portet, C. and Simon, P. (2006). Electrode surface treatment and electrochemical impedance spectroscopy study on carbon/carbon supercapacitors. **Applied Physics A**. 82(4): 639-646.
- TK, B. S., Nair, A. B., Abraham, B. T., Beegum, P. S. and Thachil, E. T. (2014). Microwave exfoliated reduced graphene oxide epoxy nanocomposites for high performance applications. **Polymer**. 55(16): 3614-3627.
- Tuinstra, F. and Koenig, J. L. (1970). Raman spectrum of graphite. **The Journal of chemical physics**. 53(3): 1126-1130.
- Ungar, T., Gubicza, J., Ribarik, G., Pantea, C. and Zerda, T. W. (2002). Microstructure of carbon blacks determined by X-ray diffraction profile analysis. **Carbon**. 40(6): 929-937.
- Vivekchand, S., Rout, C. S., Subrahmanyam, K., Govindaraj, A. and Rao, C. (2008). Graphene-based electrochemical supercapacitors. **Journal of Chemical Sciences**. 120(1): 9-13.
- Wang, D.-W., Li, F., Chen, Z.-G., Lu, G. Q. and Cheng, H.-M. (2008). Synthesis and electrochemical property of boron-doped mesoporous carbon in supercapacitor. **Chemistry of Materials**. 20(22): 7195-7200.
- Wang, T., Wang, L. X., Wu, D. L., Xia, W. and Jia, D. Z. (2015). Interaction between nitrogen and sulfur in co-doped graphene and synergetic effect in supercapacitor. **Scientific reports**. 5(1): 1-9.
- Wang, Y., Shi, Z., Huang, Y., Ma, Y., Wang, C., Chen, M. and Chen, Y. (2009). Supercapacitor devices based on graphene materials. **The Journal of Physical Chemistry C**. 113(30): 13103-13107.

- Wang, Z., Li, P., Chen, Y., He, J., Zhang, W., Schmidt, O. G. and Li, Y. (2014). Pure thiophene–sulfur doped reduced graphene oxide: synthesis, structure, and electrical properties. **Nanoscale**. 6(13): 7281-7287.
- Winter, M. and Brodd, R. J. (2005). What are batteries, fuel cells, and supercapacitors? (Chem. Rev. 2003, 104, 4245– 4269. Published on the Web 09/28/2004.). **Chemical reviews**. 105(3): 1021-1021.
- Xiang, D., Yin, L., Wang, C. and Zhang, L. (2016). High electrochemical performance of RuO<sub>2</sub>–Fe<sub>2</sub>O<sub>3</sub> nanoparticles embedded ordered mesoporous carbon as a supercapacitor electrode material. **Energy**. 106: 103-111.
- Xu, B., Yue, S., Sui, Z., Zhang, X., Hou, S., Cao, G. and Yang, Y. (2011). What is the choice for supercapacitors: graphene or graphene oxide? **Energy and Environmental Science**. 4(8): 2826-2830.
- Xu, L. Q., Liu, Y. L., Neoh, K. G., Kang, E. T. and Fu, G. D. (2011). Reduction of graphene oxide by aniline with its concomitant oxidative polymerization. **Macromolecular rapid communications**. 32(8): 684-688.
- Yang, D. and Bock, C. (2017). Laser reduced graphene for supercapacitor applications. **Journal of power sources**. 337: 73-81.
- Yang, Y., Hu, X., Zhao, Y., Cui, L., Huang, Z., Long, J. and Liao, W. (2017). Decontamination of tetracycline by thiourea-dioxide–reduced magnetic graphene oxide: effects of pH, ionic strength, and humic acid concentration. **Journal of colloid and interface science**. 495: 68-77.
- Yar, A., Dennis, J. O., Saheed, M. S. M., Mohamed, N. M., Irshad, M. I., Mumtaz, A. and Jose, R. (2020). Physical reduction of graphene oxide for supercapacitive charge storage. **Journal of Alloys and Compounds**. 822: 153636.

- Yuan, S., Huang, X., Wang, H., Xie, L., Cheng, J., Kong, Q. and Chen, C. M. (2020). Structure evolution of oxygen removal from porous carbon for optimizing supercapacitor performance. **Journal of Energy Chemistry**. 51: 396-404.
- Yuan, Y. and Lee, T. R. (2013). Contact angle and wetting properties. In **Surface science techniques**. pp. 3-34 : Springer.
- Zhang, L. L. and Zhao, X. (2009). Carbon-based materials as supercapacitor electrodes. **Chemical Society Reviews**. 38(9): 2520-2531.
- Zhang, W. B., Zhang, Z. X., Yang, J. H., Huang, T., Zhang, N., Zheng, X. T. and Zhou, Z. W. (2015). Largely enhanced thermal conductivity of poly (vinylidene fluoride)/carbon nanotube composites achieved by adding graphene oxide. **Carbon**. 90: 242-254.
- Zhao, B., Liu, P., Jiang, Y., Pan, D., Tao, H., Song, J. and Xu, W. (2012). Supercapacitor performances of thermally reduced graphene oxide. **Journal of power sources**. 198: 423-427.
- Zhao, X. and Ando, Y. (1998). Raman spectra and X-ray diffraction patterns of carbon nanotubes prepared by hydrogen arc discharge. **Japanese Journal of Applied Physics**. 37(1): 4846-4849.
- Zhou, D. and Han, B. H. (2010). Graphene-based nanoporous materials assembled by mediation of polyoxometalate nanoparticles. **Advanced Functional Materials**. 20(16): 2717-2722.
- Zhou, Y., Bao, Q., Tang, L. A. L., Zhong, Y. and Loh, K. P. (2009). Hydrothermal dehydration for the “green” reduction of exfoliated graphene oxide to graphene and demonstration of tunable optical limiting properties. **Chemistry of Materials**. 21(13): 2950-2956.

- Zhu, D., Cheng, K., Wang, Y., Sun, D., Gan, L., Chen, T. and Liu, M. (2017). Nitrogen-doped porous carbons with nanofiber-like structure derived from poly (aniline-co-p-phenylenediamine) for supercapacitors. **Electrochimica Acta**. 224: 17-24.
- Zhu, Y., Stoller, M. D., Cai, W., Velamakanni, A., Piner, R. D., Chen, D. and Ruoff, R. S. (2010). Exfoliation of graphite oxide in propylene carbonate and thermal reduction of the resulting graphene oxide platelets. **ACS nano**. 4(2): 1227-1233.
- Zhuo, Q., Zhang, Y., Du, Q. and Yan, C. (2015). Facile reduction of graphene oxide at room temperature by ammonia borane via salting out effect. **Journal of colloid and interface science**. 457: 243-247.
- Zielke, U., Hüttinger, K. and Hoffman, W. (1996). Surface-oxidized carbon fibers: I. Surface structure and chemistry. **Carbon**. 34(8): 983-998.





**APPENDIX**

## APPENDIX

Manuscript was published as Nathabumroong, S., Pochai, C., Chanlek, N., Eknapakul, T., Sonsupap, S., Tuichai, W., Sriprachuabwong, C., Tuantranont, A., Rujirawat, S., Songsiriritthigul, Pand Yimnirun, R. (2021). Enhanced surface and electrochemical properties of nitrogen-doped reduced graphene oxide by violet laser treatment for high charge storage and lower self-discharge supercapacitors. *Journal of Power Sources*, 513, 230517.

### **Enhanced surface and electrochemical properties of nitrogen-doped reduced graphene oxide by violet laser treatment for high charge storage and lower self-discharge supercapacitors**

Sarawudh Nathabumroong<sup>a</sup>, Chatwarin Pochai<sup>b</sup>, Narong Chanlek<sup>c</sup>, Tanachat Eknapakul<sup>a</sup>, Somchai Sonsupap<sup>a</sup>, Wattana Tuichai<sup>d</sup>, Chakrit Sriprachuabwong<sup>b</sup>, Saroj Rujirawat<sup>e</sup>, Prayoon Songsiriritthigul<sup>a</sup>, Adisorn Tuantranont<sup>b</sup>, Rattikorn Yimnirun<sup>e,f,\*</sup>

<sup>a</sup>Research Network NANOTEC-SUT on Advanced Nanomaterials and Characterization, School of Physics, Institute of Science, Suranaree University of Technology, Nakhon Ratchasima, 30000, Thailand

<sup>b</sup>Graphene and Printed Electronics for Dual-Use Applications Research Division GPERD, National Security and Dual-Use Technology Center (NSD), National Science and Technology Development Agency (NSTDA), 111 Thailand Science Park, Thanon Phahonyothin, Tambon Klong Nueng, Amphoe Klong Luang, Phatum Thani, 12120, Thailand

<sup>c</sup>Synchrotron Light Research Institute, Nakhon Ratchasima, 30000, Thailand

<sup>d</sup>Department of Physics, Faculty of Science, Khon Kaen University, Khon Kaen, 40002, Thailand

<sup>e</sup>School of Energy Science and Engineering, Vidyasirimedhi Institute of Science and Technology, Rayong, 21210, Thailand

<sup>f</sup>Research Network of NANOTEC-VISTEC on Nanotechnology for Energy, Vidyasirimedhi Institute of Science and Technology (VISTEC), Wangchan, Rayong, 21210, Thailand

This work demonstrated that the performance improvement of nitrogen-doped reduced graphene oxide (N-rGO) electrodes over reduced graphene oxide (rGO) electrodes for supercapacitors could be further enhanced by violet laser treatment (VLT). A specific capacitance of 30 and 145 F g<sup>-1</sup> was obtained for rGO and N-rGO electrodes, respectively. When using N-rGO with proper VLT, a high specific capacitance of 214 F g<sup>-1</sup> could be achieved. In addition, the percentage of capacitive retention of the N-rGO with VLT remaining 94% after 10,000 cycles with a slower self-discharge rate at 0.55 V h<sup>-1</sup>, comparing to 0.91 V h<sup>-1</sup> for N-rGO. Systematic investigations of N-rGO with VLT were carried out by using different film characterization techniques. The surfaces of N-rGO with VLT exhibit an increase in the number of exfoliated graphene oxide sheets with more roughness when increasing the fluence of laser. It was also found that there are the decrease in oxygen/nitrogen-containing functional groups contents and the increases in graphitic carbon phase with C–C sp<sup>2</sup>-hybridization with the influence of laser. These may explain the improvements of the reported charge storage ability, electrode stability, and self-discharge rate.

<https://doi.org/10.1016/j.jpowsour.2021.230517>

Received 3 June 2021; Received in revised form 24 August 2021; Accepted 10 September 2021 0378-7753/© 2021 Published by Elsevier B.V.

Abstract presented at the 2018 ISAF-FMA-AMF-AMEC-PFM (IFAAP) Joint Conference (IFAAP2018), Hiroshima, Japan

### **High performance of hybrid Li-ion supercapacitors using N-doped reduce graphene oxide as cathode active material**

**S. Nathabumroong<sup>1</sup>, C. Pochai<sup>2</sup>, P. Thangdee<sup>1</sup>, A. Tuantranont<sup>2</sup>,  
S. Rujirawat<sup>1</sup>, and R. Yimnirun<sup>3</sup>**

<sup>1</sup>School of Physics, Institute of Science, and NANOTEC-SUT COE on Advanced Functional Nanomaterials, Suranaree University of Technology, NakhonRatchasima, 30000, Thailand

<sup>2</sup>National Electronics and Computer Technology Center (NECTEC), Pathum Thani, 12120, Thailand

<sup>3</sup>School of Energy Science and Engineering, Vidyasirimedhi Institute of Science and Technology, Rayong, 21210, Thailand

\*Corresponding Author: sn\_1779@hotmail.com

Lithium-ion hybrid supercapacitors (LIHSs) are interesting energy storage devices which exhibit integrating both advantages as the rapid charge-discharge and long life cycle of supercapacitors and high energy-stored capacity of lithium-ion batteries. Hence, they have been applied to several applications such as electric drive vehicles and some industries etc. Herein, N-doped reduced graphene oxide (N-rGO) was synthesized via hydrothermal technique with various concentrations of urea. Then, the obtained materials were utilized as a cathode material in the hybrid Li-ion supercapacitor consisting of lithium foil as an anode and lithium bis(trifluoromethylsulphonyl)imide (LiTFSi) as an organic electrolyte. Our cathode materials were examined their morphology by scanning electron microscope (SEM), transmission electron microscopy (TEM), X-ray diffraction (XRD), and Raman spectroscopy. Moreover, our electrochemical properties of hybrid Li-ion supercapacitors were characterized by galvanostatic charge/discharge (GCD), electrochemical impedance spectroscopy (EIS), and stability testing to evaluate their performance.

#### **References**

- [1] M. D. Stoller, et al., Physical chemistry chemical physics, 14, 3388-3391 (2012)
- [2] J. Lang, et al., Journal of energy chemistry, 27, 43-56 (2018)

Abstract presented at the 5<sup>th</sup> International Conference on Smart Materials and Nanotechnology 2020 (SmartMat@2020), Pattaya, Thailand

**Comparison properties of reduced graphene oxide (rGO) nitrogen doped reduced graphene oxide (N-rGO) and nitrogen and sulfur co-doped reduced graphene oxide (NandS-rGO) electrodes for symmetric supercapacitors**

S. Nathabumroong<sup>1</sup>, C. Poochai<sup>2</sup>, N. Chanlek<sup>3</sup>, H. Nakajima<sup>3</sup>, R. Yimnirun<sup>4,5</sup>,  
S. Rujirawat<sup>3</sup>, P. Songsiriritthigul<sup>1</sup>, P. Manyum<sup>1</sup> and A. Tuantranont<sup>2</sup>

<sup>1</sup>School of Physics, Institute of Science, and NANOTEC-SUT COE on Advanced Functional Nanomaterials, Suranaree University of Technology, Nakhon Ratchasima, 30000, Thailand

<sup>2</sup>Graphene and Printed Electronics for Dual-Use Applications Research Division (GPERD), Nation Security and Dual-Use Technology Center (NSD), Nation Science and Technology Development Agency (NSTDA), 111 Thailand Science Park, Thanon Phahonyothin, Tambon Klong Nueng, Amphoe Klong Luang, Phatum Thani 12120, Thailand

<sup>3</sup>Synchrotron Light Research Institute, Nakhon Ratchasima, 30000 Thailand

<sup>4</sup>School of Energy Science and Engineering, Vidyasirimedhi Institute of Science and Technology, Rayong, 21210, Thailand

<sup>5</sup>Research Network of NANOTEC-VISTEC on Nanotechnology for Energy, Vidyasirimedhi Institute of Science and Technology (VISTEC), Wangchan, Rayong, 21210, Thailand

*\*Email: sn\_1779@hotmail.com*

Symmetric supercapacitors (SCs) is energy storage that consist of two same electrodes sandwich separator which soak with electrolyte. reduced graphene oxide (rGO) is a widely used materials for SCs electrode. To improve properties, rGO was proposed to functionalize with urea and thiourea, called N-rGO and NandS-rGO, respectively. Both urea and thiourea simply synthesized by a hydrothermal technique with graphene oxide by same 30 % w/v in concentration. Both aqueous and organic electrolyte were used for assembly. Nitrogen can improve via enhance conductivity and pseudocapacitance. Sulfur help more hydrophilicity. Performance of symmetric SCs coin cells were evaluated and showed both urea and thiourea doping which are enhance the specific capacitance for both electrolytes higher 100% compare with rGO by using galvanostatic charge/ discharge (GCD) and cyclic voltammetry (CV). Subsequently, electrodes were characterized by using X-ray diffraction (XRD), Raman spectroscopy, X-ray photoelectron spectroscopy (XPS), scanning electron microscopy (SEM), Fourier transform-infrared (FT-IR) and contact angle to investigate surface electrodes.

**Keyword:** reduced graphene oxide, nitrogen doped reduced graphene oxide, nitrogen and sulfur doped reduced graphene oxide, the specific capacitance

# CURRICULUM VITAE

Name: Mr. Sarawudh Nathabumroong

Date of birth: 17 January 1991

Place of birth: Yasothon, Thailand

Nationality: Thai

## Education

Academic year

2009-2012 Khon kaen University, Khon kaen, Thailand.

Bachelor of Science (Physics)

2013-2016 Suranaree University of Technology, Nakhon Ratchasima, Thailand.

Master of Science (Physics)

2017-2020 Suranaree University of Technology, Nakhon Ratchasima, Thailand.

Degree of Doctor of Philosophy (Physics)